Pascal Ifeacho

Semi-conducting metal oxide nanoparticles from a low-pressure premixed $H_2/O_2/Ar$ flame:

Synthesis and Characterization

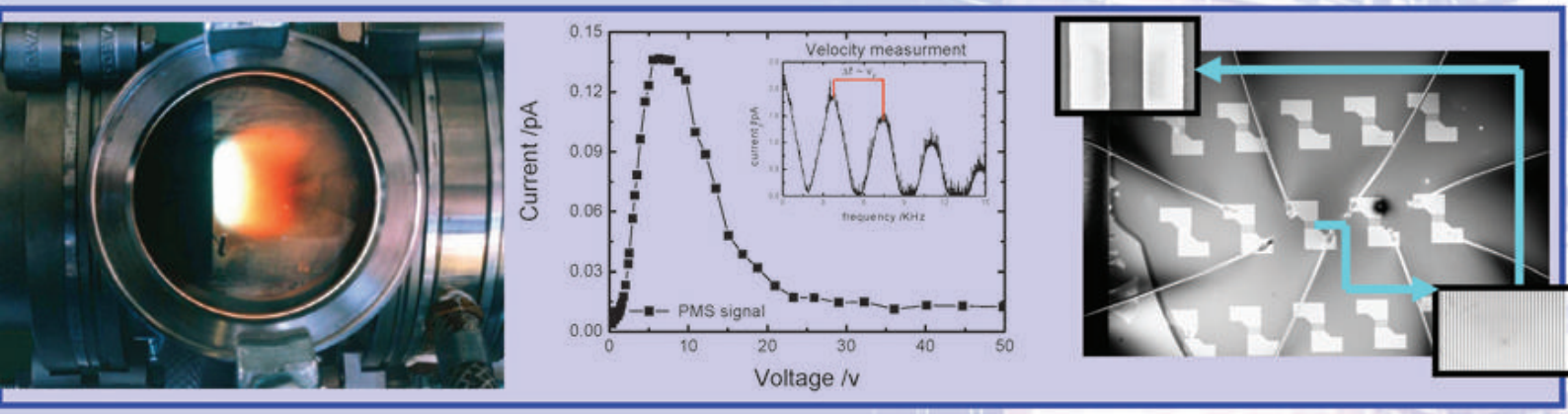

Cuvillier Verlag Göttingen
Internationaler wissenschaftlicher Fachverlag

Semi-conducting metal oxide nanoparticles from a low-pressure premixed H_2/O_2/Ar flame: Synthesis and Characterization

Von der Fakultät für Ingenieurwissenschaften, Abteilung Maschinenbau der

Universität Duisburg-Essen

zur Erlangung des akademischen Grades

DOKTOR-INGENIEUR

genehmigte Dissertation

von

Pascal Onyibo Ifeacho

aus

Enugu, Nigeria

Referent: Prof. Dr.-Ing. Paul Roth

Korreferent: Prof. Dr. Sortiris E, Pratsinis

Tag der mündlichen Prüfung: 16.10.2008

Bibliografische Information der Deutschen Nationalbibliothek
Die Deutsche Nationalbibliothek verzeichnet diese Publikation in der Deutschen Nationalbibliografie; detaillierte bibliografische Daten sind im Internet über http://dnb.ddb.de abrufbar.
1. Aufl. - Göttingen : Cuvillier, 2008
Zugl.: Duisburg-Essen, Univ., Diss., 2008

978-3-86727-816-4

© CUVILLIER VERLAG, Göttingen 2008
Nonnenstieg 8, 37075 Göttingen
Telefon: 0551-54724-0
Telefax: 0551-54724-21
www.cuvillier.de

Alle Rechte vorbehalten. Ohne ausdrückliche Genehmigung des Verlages ist es nicht gestattet, das Buch oder Teile daraus auf fotomechanischem Weg (Fotokopie, Mikrokopie) zu vervielfältigen.
1. Auflage, 2008
Gedruckt auf säurefreiem Papier

978-3-86727-816-4

Forward

This work was done during my time as a research assistant at the institute for combustion and gas dynamics of the university of Duisburg-Essen, Duisburg, Germany

My appreciation goes to all those who in their own little way contributed towards the successful realization of this work.

Special gratitude goes to the following persons:

Prof. Dr.-Ing Paul Roth for his academic guidance throughout the project
Prof. Dr. Sotiris E, Pratsinis for accepting to co-referre this work
Prof. Dr. Christof Schulz for his unflinching support and cooperation
Dr. Hartmut Wiggers who taught me everything I know about nano-science
Special thank you to all staff, colleagues and friends from the Institute/SFB445, and especially to my family for being very supportive of my decisions.

To God be the glory!

Köln 26th November 2008

Table of content

1 Introduction ---------- 1

2 Theory ---------- 5

2.1 **General flame phenomena ---------- 5**

2.2 **Parameters influencing premixed flame combustion synthesis ---------- 7**

2.2.1 Influence of fuel/oxidant ratio ---------- 7

2.2.2 Influence of inert gas additives ---------- 7

2.2.3 Influence of pressure ---------- 8

2.2.4 Influence of temperature distribution ---------- 8

2.3 **Fundamentals of gas-to-particle conversion ---------- 8**

2.3.1 Gas-to-particle conversion for single component metal oxide (MO_x) systems ---------- 9

2.3.1.1 Homogenous nucleation ---------- 10

2.3.1.2 Coagulation, Coalescence and Agglomeration ---------- 11

2.3.2 Gas-to-particle conversion for multi-component metal oxide systems ---------- 14

2.4 **Physical and optical properties of nanosized semi-conducting metal oxides ---- 16**

2.4.1 Particle morphology ---------- 16

2.4.2 Crystallinity ---------- 17

2.4.3 Hall-Petch effect ---------- 18

2.4.4 Band model ---------- 18

2.4.5 Band-gap ---------- 20

2.4.6 Quantum size effect ---------- 21

2.4.7 Inter-band absorption ---------- 22

3 Experimental set-up, in-situ and ex-situ analytical methods ---------- 24

3.1 **Precursor dilution systems ---------- 24**

3.1.1 Mixing vessel method ---------- 24

3.1.2 Controlled evaporation and mixing ---------- 26

3.1.3 Pressure controlled mixing ---------- 27

3.2 **Flame synthesis of metal oxide nanoparticles ---------- 28**

3.2.1 The low-pressure flame reactor ---------- 29

3.2.2 Thermophoretic sampling of particles and pneumatic assisted sampling ---------- 30

3.2.3 Filter by-pass system ---------- 31

3.3 **Particle mass spectrometer (PMS) ---------- 32**

3.4 **Laser induced incandescence ---------- 39**

3.4.1 Theory of TiRe-LII ---------- 40

3.4.1.1 Particle heating ---------- 41

3.4.1.2 Particle cooling ----42
3.4.2 *TiRe-LII* experimental set-up----43
3.5 **Ex-situ characterization techniques ---- 44**
3.5.1 X-ray diffraction (XRD) ----45
3.5.2 Brunauer-Emmett-Teller (BET) absorption isothermal----46
3.5.3 *UV-Vis* spectroscopy ----47
3.5.4 Transmission electron microscopes (TEM and HRTEM) ----48
3.5.5 Impedance spectroscopy IS ----48
4 Synthesis of particles in low-pressure flame ----51
4.1 **Metal oxides synthesis in the low-pressure flame ---- 51**
4.1.1 Synthesis of SnO_2 nanoparticles ----53
4.1.2 Characterization of flame synthesized SnO_2 nanoparticles ----54
4.1.2.1 Particle mass spectrometry ----54
4.1.2.2 X-ray diffraction (*XRD*) ----58
4.1.2.3 Transmission electron microscope (TEM) ----59
4.1.2.4 UV-spectroscopy ----61
4.1.3 Tuning the stoichiometry of tin oxide (SnO_x for $1.4 \leq x \leq 1.8$) ----63
4.1.4 Electrical properties of SnO_2 and SnO_x nanoparticles ----70
4.2 **Titanium dioxide nanoparticles (TiO_2)---- 75**
4.2.1 Synthesis of TiO_2 nanoparticles ----75
4.2.2 Characterization of flame synthesized TiO_2 nanoparticles ----76
4.2.3 Photocatalytic activity of flame synthesized TiO_2 nanoparticles ----82
4.3 **TiO_2-SnO_2 mixed oxide nanoparticles---- 85**
4.3.1 Synthesis of TiO_2-SnO_2 mixed oxide nanoparticles----86
4.3.2 Characterization of the TiO_2-SnO_2 mixed oxide particles----86
4.3.3 Electrical properties of the TiO_2-SnO_2 mixed oxide nanoparticles----94
4.4 **Time resolved laser induced incandescence (*TiRe-LII*) ---- 96**
4.4.1 Synthesis and characterization of Fe_2O_3 nanoparticles ----96
4.4.2 Synthesis of soot particles in the low-pressure reactor ----98
4.4.3 Characterization of soot particles----99
5 Conclusion ---- 105
6 References---- 108
7 Appendix A---- 114

Nomenclature of used symbols

Symbol	Definition	Unit
a	surface area of agglomerates	cm^{-2}
a_{wt}	weight of sample materials	g
A	absorbance of light	
b_k	width of the deflection capacitor	mm
B	*full width at half maximum* (FWHM)	
c_p	specific heat capacity (isobaric)	$J\ Kg^{-1}\ K^{-1}$
C_p	precursor concentration	ppm
c_{tg}	mean thermal velocity of the evaporated molecule	ms^{-1}
C_{TD}	mean thermal velocity of the gas molecule	ms^{-1}
d	distance between atomic layers in a crystal	nm
d_{gn}	geometric number mean diameter	nm
d_o	diameter of primary particle	nm
d_p	droplet or particle diameter	nm
$d_p^{\ o}$	exit diameter of the particle	nm
$d_{pcrystallite}$	crystallite diameter of a material	nm
d_{pi}	particle diameter	nm
d_{pn}	number (count) mean diameter	nm
D_f	mass fractal dimension	
$\left\vert\vec{E}\right\vert$	electric field strength	$v.m^{-1}$
E_v	energy in the lower state (valence band)	eV
E_c	energy in excited state (conduction band)	eV
E_F	*Fermi* energy	eV
E_g	band gap energy	eV
E_{kin}	kinetic energy	J
E_0	energy density of the laser	$J\ m^{-2}$
$\left\vert\vec{F}_y\right\vert$	deflection force due to an electric field in the y-direction	N
f_{min}	frequency minimum	Hz
F	*Kubelka-Munk* function	
G, G_0	conductance	S
G	particle growth law	$cm^3\ s^{-1}$
hv	photon energy	eV

Symbol	Definition	Unit
Δh_v	evaporation enthalpy	J Kg^{-1}
I_f	nucleation rate	molecules/cm^3s
I	light beam passing through sample	
I_o	reference beam	
J_{evp}	evaporation rate	Kg s^{-1}
k	imaginary part of the complex refractive index	
K_F	coagulation coefficient in free molecular regime	$cm^{5/2}$ s^{-1}
K_{PMS}	*PMS* constant	J/V
l	distance	mm
L	crystallite size	nm
L_g	distance between grids	mm
L_k	length of plate capacitor	mm
$L_{p,i}$	particle package length	mm
L_{PMS}	length of PMS	mm
m	complex refractive index of particles	
m_p	mass of particle	g
m_1	mass of a molecule or atom	g
M	molecular weight of adsorbate	g
M_i	mass of particles within a section	g
n	number concentration	cm^{-3}
n_e	number of charges	
N_f	number of primary particles	
N_i	number of particles in an interval in an agglomerate	
N_∞	total particle or aggregate concentration	cm^{-3}
P_1	partial pressure of species 1	dyne cm^{-2}
P_g	gas pressure	Pa
P_D	reactor pressure	mbar
q	phonon absorption	eV
q_{abs}	heat flux due to absorption	W
q_{cond}	heat flux due to conduction	W
q_{evap}	heat flux due to evaporation	W
q_{rad}	heat flux due to radiation	W
R	reflectance	
R_a	characteristic length of an aggregate	nm

Symbol	Definition	Unit
s	adsorption cross section	nm^2
S	specific surface	$m^2\ g^{-1}$
S_{at}	saturation ratio	
S_{bb}	radiation signal from black body	
S_p	particle emission signal	$V^{\#}$
S_{total}	total surface area	$m^2\ g^{-1}$
t	time	s
T	temperature	K
T_{bb}	temperature of black body	K
T_g	gas temperature	K
T_p	particle temperature	K
U_K	deflection voltage	V
v_f	laminar burning velocity	ms^{-1}
v_g	velocity of fresh gas	ms^{-1}
v_m	monolayer adsorbed gas quantity	m^3
v_p	speed of propagation	ms^{-1}
x	flow coordinate (height above burner)	mm
y	trajectory of particle deflection	
Z	Impedance (real and imaginary)	Ω

Greek symbols

Symbol	Definition	Unit
A	absorption coefficient	
α_T	energy accommodation coefficient	
α_v	accommodation coefficient for evaporation	
β_F	Collision frequency in free-molecule regime	$cm^3\ s^{-1}$
$\beta(v\text{-}v')$	collision frequency of particles of volume v and v'	$cm^3\ s^{-1}$
δ	delta function	
ε	total emission ratio of the particle	
ε_p	spectral emission ratio of the particle	
ε_{pf}	Dimensionless pre-factor (value = 1)	
$\hbar\omega$	photon energy	eV
θ	diffraction angle	°
λ	wavelength of X-ray beam	nm

Symbol	Definition	Unit
λ_1, λ_2, $\lambda_{detection}$	detection wavelength	nm
λ_{laser}	wavelength of the laser	nm
μ	gas viscosity	g cm^{-1} s^{-1}
v_i, v_j, v, v'	particle volume	cm^3
v^*	critical particle volume	cm^3
ρ	density	g cm^{-3}
ρ_p	mass density of the particle	g cm^{-3}
ρ_∞	vapour density at distance of infinity from particle	g cm^{-3}
ρ_s	vapour density at particle surface	g cm^{-3}
σ	resistivity	$S.m^{-1}$
σ_0	friction stress	Pa
σ_g	geometric standard deviation	
σ_y	yield strength	Pa
τ_f, τ_c	characteristic time for coalescence and coagulation	s

Constants

Symbol	Definition	Value
c_o	velocity of light in vacuum	299792456 ms^{-1}
e	elementary charge	$1.6 \cdot 10^{-19}$ C
k_B	Boltzmann constant	$1.38 \cdot 10^{-23}$J K^{-1}
N	Avogadro's number	moles/molecule
Π	pie	3.1428
σ	Stefan-Boltzmann constant	$5.67 \cdot 10^{-8}$ W m^{-2} K^{-4}

Abbreviations

Acronym	Definition
AES	auger electron spectroscopy
BET	(Brunauer, Emmett, Teller)
CEM™	controlled evaporation and mixing
CMD	count mean diameter

Acronym	Definition
DRA	diffuse reflectance accessory
EDX	energy dispersive X-ray spectroscopy
EELS	electron energy loss spectroscopy
FWHM	full width at half maximum
GDE	general dynamic equation
HAB	height above burner
HF	high frequency
HR-TEM	high-resolution transmission electron microscope
IDC	inter-digital capacitor
IS	Impedance spectroscopy
LF	low frequency
MBAPD	molecular beam assisted particle deposition
Nd:YAG	neodymium: yttrium-aluminium-grant-laser
NO-LIF	nitrogen oxide-laser induced fluorescence
PDF	probability density function
PID	proportional-integral-derivative
PM	photomultiplier
PMC	pre mixing chamber
PMS	particle mass spectrometer
TEM	transmission electron microscope
TEOS	tetraethoxysilane
TiRe-LII	time resolved laser induced incandescence
TMT	tetramethyl tin
TTIP	titanium tetra isopropoxide
UV light	ultra violet light
UV-VIS	ultra violet-visible
VOC	volatile organic compound
XRD	X-ray diffraction

1 Introduction

Currently research, development, and production of technologies based on nanomaterials have leapt from its infancy several decades ago to high levels of commercial activities [1,2]. While much effort is on developing new technologies, most emphasis is on the improvement and consolidation of existing technologies based on initial potentials observed in nanosized materials. The growth and development in nanotechnology has been fundamentally propelled by inter-disciplinary cooperation in the areas of natural science, engineering, and business management. This cooperation facilitates speedy realization of ideas, as well as goal-oriented research based on a balanced economic strategy. The result is increasing financial and resource investment in nanotechnology, which is expected to exceed a $1trillion by 2015 [3].

Nanoparticles, which are commonly defined as particles below 100 nm are considered the fundamental building blocks of most nanomaterial based devices. Many materials in nature (bulk) that exhibit special properties like magnetism, hardness, and different pigmentation, have fuelled the research towards the development of special devices and applications based on these properties. The properties of Nanomaterials differ from bulk due to higher atom concentration on the nanomaterial surface, with decreasing particle diameter. Hence, increased surface area to volume ratio is common for nanosized materials, in comparison to bulk [4]. Research interest in nanomaterials ranges from single elements like silicon and iron, through to nitrides, carbides and metal oxides (MO_x), which is the focus of this research.

Metal oxides (MO_x) occur naturally in different configuration, and have been exploited for millions of years due to their unique properties such as hardness, colour, porosity, brittleness etc. Zinc oxides (ZnO), iron oxide (Fe_2O_3), silicon oxide (SiO_2) are some metal oxides that have sustainably been produced commercially in several million tons annually for several decades. The oxides have been engineered for applications in UV shielding cream, pigments, and catalysis. However, current investigations of these materials are revealing further properties, especially when these materials are processed (i.e. turned into transparent thin films) or “functionalized” (i.e. modification of the surface group). This has fuelled utilization of these materials for devices such as touch screen displays, gas sensors and solar cells.

The unique properties exhibited by metal oxides are due to their physico-chemical properties based on their particle size, morphology, crystallinity etc. Metal oxides can be electrically conducting, non-conducting or semi-conducing depending on their physical properties. Semi-conducting metal oxide particles are of particular interest because of the ease to influence their conductivity by varying parameters such as the ambient gas composition, particle size, temperature of exposure etc [5]. Nanosized tin oxide has been established as a semi-conducting metal oxide, which changes its conductivity under different conditions (oxidizing and reducing). This special feature of tin oxide makes it a potential material for gas-sensing, and is currently used in many solid state gas-sensing devices. However, its "response and relaxation time" (the time it takes to reach its maximum conductivity when exposed to a gaseous medium, and vice versa) is relatively low. Furthermore, tin oxide exhibits poor "sensitivity" (change of conductivity in the presence of a gaseous medium) towards some gases, which limits its applicability as a material for sensing diverse gases.

Titania (TiO_2) is the most widely researched metal oxide, which is used for pigments and photo-mineralization of volatile organic compounds (*VOCs*). The photo-mineralization of TiO_2 coupled with its transparency, makes it a widely used material for coating glass, which is sold as "self cleaning glass" by firms like Pilkington and Saint Gobain. However, this ability to reduce *VOCs* upon irradiation with light (UV) is constrained by low efficiency, due to the relatively low UV content of sunlight [6,7]. Research into nanosized TiO_2 has revealed that doping titania with Fe_2O_3 or nitrogen, results in a shift of the absorption spectrum of titania towards higher efficiency, upon exposure to sunlight. However, the transparency of the material is lost by this "functionalization" (material colour changes to red-brown due to Fe_2O_3 content), hence the material cannot be used to coat transparent surfaces. Furthermore, the surface group of titania can be modified to make it hydrophilic or hydrophobic, whereby hydrophilicity of titania is essential for applications such as self cleaning glass.

These two illustrations of the applicability of nanosized SnO_2 and TiO_2 particles, establish the challenges posed by nanomaterials and the need for continued research into the factors that influence material properties. The synthesis route employed in generating semi-conducting MO_x nanoparticles significantly affects their properties (i.e. particle size, morphology and crystallinity). For most synthesis route, varying the experimental parameters directly influences the properties of the generated metal oxide

particles. Therefore, investigating the extent of these effects on the material, often serves as the basis for most synthesis based research on nanoparticles.

Several methods have successfully been employed for both laboratory and industrial synthesis of nanosized metal oxides [8-10]. The choice of synthesis route is often guided by the product, cost, safety etc. One such method is gas-phase synthesis of metal oxides in a flame reactor[11]. The advantages of this process include; wide operational scale (laboratory, pilot plant and industrial plants are possible), low operational cost, purity of product material, easy control of material properties by varying synthesis parameters and high product yield. For this synthesis route, the temperature-time history has been identified as one of the most important factors that influence particle size, crystallinity, and morphology [11]. A typical size dependent effect observed in MO_x was reported for premixed flame synthesized Fe_2O_3 nanoparticles, whereby the blocking temperature of the particles were observed to vary between 50 and 150 K for particle diameters between 4 and 10 nm [12].

Several metal oxides (TiO_2, GeO_2, SnO_2, SiO_2-Fe_2O_3) have been successfully synthesized using different kinds of flame reactors [13-17]. However, for the purpose of this research a premixed H_2/O_2/Ar flame operated in a low-pressure reactor was used to synthesize a variety of single metal oxides and mixed oxide particles. The objective of this research is focused on the investigation into the synthesis of semi-conducting MO_x nanoparticles for well defined applications. Good theoretical understanding of the objectives, coupled with advanced characterization techniques, are required to set-up a synthesis structure, which in the middle of a constant feedback loop is necessary for continuous improvement of the synthesized MO_x nanoparticles. The fundamental queries that drove this study are as follows:

a) What is the relationship between the experimental parameters such as temperature, pressure, residence time etc, on the structure and properties of the semi-conducting MO_x?

b) How can the properties of semi-conducting MO_x be tuned or improved for application purposes?

c) How can deposition of semi-conducting MO_x nanoparticles on surfaces for characterization or incorporation in devices be achieved?

d) Which characterization methods can deliver detailed information on material systems?

The premixed flame was chosen as the synthesis route for all investigations in this study, because of the huge success achieved with this method for the generation of MO_x nanoparticles [18,19]. The reactor equipped with an *in-situ* particle mass spectrometer for particle size analysis, was modified for the synthesis of diverse semi-conducting MO_x nanoparticles. *Ex-situ* characterization of the flame synthesized materials was performed with X-ray diffractometery (*XRD*) for information on crystal structure and composition. Brunauer-Emmett-Teller (*BET*) adsorption isothermal was used for surface area characterization. High resolution transmission electron microscope (*HR-TEM*) was used for information on particle-size, morphology, and composition. Impedance spectroscopy (*IS*) was used for information on conductivity and charge carrier transport, while ultraviolet-visible spectroscopy (*UV-VIS*) was used to obtain information on the optical absorption spectrum of the material.

In this study, the theory behind flame synthesis of MO_x particles is presented in chapter 2 for purpose of clarity and basic understanding of this thesis. Chapters 3, deals with characterization methods, flame reactor set-up, and various equipment description. Detailed results obtained from synthesis of SnO_2, TiO_2, SnO_2/TiO_2 and diagnostic work on soot particles with time resolved laser induced incandescence (*TiRe-LII*) are presented in chapter 4. The summary of this dissertation is presented in chapter 5, while chapters 6 and 7 are the references and the appendix respectively.

2 Theory

2.1 General flame phenomena

Flames can simply be described as self propagating subsonic reaction wave usually with a luminous zone and heat release [20]. The terms, "premixed" and "diffuse" are commonly used to describe the mixing nature of combustion gases before ignition. The laminar premixed flame that was used for this research is characterized by the flame thickness and laminar burning velocity (v_f), which is defined as the propagation velocity of a reaction zone normal to its surface and relative to the unburned gas. These properties are consequently influenced by fuel type, equivalence ratio, pressure, and temperature. The laminar burning velocity is important because it is the factor that describes the flame shape and stability properties such as blow-off and flashback [21]. The fundamental laminar burning velocity v_f is correlated to the speed of fresh gas v_g and speed of flame propagation v_p according to the following equation.

$$v_f = v_p \pm v_g \tag{2.1}$$

For flame propagation in similar direction as the flow of fresh gas, the minus operation in equation 2.1 is valid, and vice versa for counter gas flow and flame propagation. The following conditions will arise for varying laminar burning velocity and fresh gas speed velocity:

Stationary flame front	$v_f = v_g$	(2.2)
Flashback	$v_f > v_g$	(2.3)
Blow-off	$v_f < v_g$	(2.4)

Premixed flames are either operated as freely-propagating or burner-stabilized, whereby burner-stabilized are typically one dimensional (flat disc shaped flame). In burner stabilized flames, the gaseous reactants enter the flame with a velocity equal to the flame propagation velocity. This is followed by combustion reactions that proceed rapidly through a thin flame front yielding products and intermediates. However, since the flame heats the products, the product density is less than the reactant density, hence,

to ensure flame continuity, the burned gas velocity must be higher than that of the unburned gas.

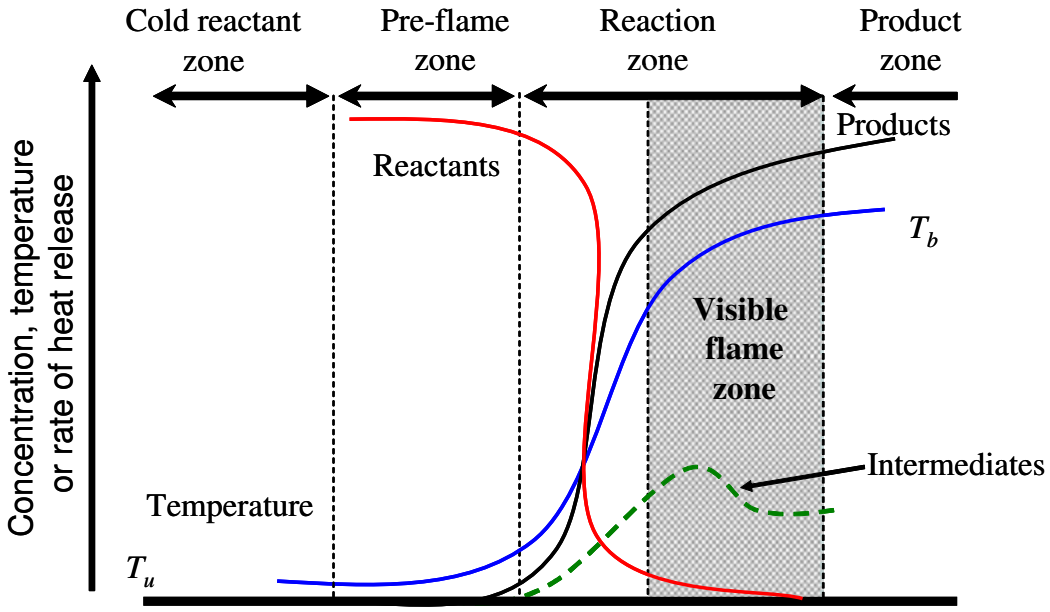

Figure 2.1: Profile of laminar flame showing temperature, reactants and products distribution [21]

Figure 2.1 shows temperature, reactants and products distribution across various zones of the laminar flame whereby T_u and T_b are the temperatures of the unburned gas and burned gas respectively. According to the detailed structure of the flame, the temperature increases smoothly from initial to final state, while the intermediates and products concentration will increase with decreasing reactant concentration. In the reaction zone the flame is often visible due to the luminescence of electronically excited species such as CH, CN, C_2, CHO and CO_2; however, non-hydrocarbon systems such as H_2/O_2 flames are invisible, whereby their presence can only be confirmed by measuring high temperatures radiating from the flame.

1-dimensional flat flame burners are often the burner of choice for combustion studies in laboratories and in some radiant burners. These burners can either be operated adiabatically, or non-adiabatically. For non-adiabatic flat flames, the burner head which is often a sintered matrix is water cooled. Constant extraction of heat from the flame via the water-cooled burner head decreases the laminar burning velocity, thereby allowing flames to be stabilized over a relatively wide range of flow conditions [22]. The ability to operate the flame under varying flow conditions is crucial for flame synthesis of materials, which often require varying inlet gas flow rates and compositions.

2.2 Parameters influencing premixed flame combustion synthesis

For the purpose of this research, premixed flame synthesis was selected as the route for the generation of nanosized semi-conducting MO_x. The premixed flame consists of hydrogen (H_2) as fuel, oxygen (O_2) as oxidizer and argon as inert gas component. The fuel/oxidant ratio, inert additives, pressure and temperature are the main factors that influence the laminar burning velocity and consequently the flame generated products.

2.2.1 Influence of fuel/oxidant ratio

The fuel/oxidant ratio is used for defining the upper (rich mixture) and lower (lean mixture) flammability limit, which establishes the region for sustainable combustion. When coupling flame chemistry with material synthesis (especially for MO_x generation), the fuel/oxidant ratio selected can influence the stoichiometry of the synthesized metal oxides [23,24].

The fuel/oxidant ratio also influences the flame temperature, whereby it is often assumed that a direct relationship exists between maximum flame temperature and maximum laminar burning velocity. However, this relationship varies with respect to different fuels and oxidants [25]. Maximum flame temperatures, as well as the overall temperature distribution during material synthesis, influence thermal dissociation of precursors, gas phase reaction of species, as well as sintering and surface growth phenomena of nanomaterials. The temperature-time profile during this process influences the properties, such as particle size, morphology and crystallinity of the material.

2.2.2 Influence of inert gas additives

The addition of inert gases such as argon (Ar), nitrogen (N_2) and helium (He) to flames influences the physical properties of the flame such as temperature, conductivity and specific heat capacity, thermal diffusivity and chemical inhibitions of reactions [26]. For the synthesis of materials using varying concentration of Ar as an additive to the premixed H_2/O_2 flame, significant changes in the physical properties of the particles are not expected. The inert gas additive serves as a “flexible” component of the inlet gas mixture, which can be varied to achieve a particular temperature or volumetric flow rate, so as to ensure flame stability. Furthermore, the cold gas inlet velocity can be

varied by changing the Ar content of the inlet gas mixture. This in turn can influence the residence time for particle growth in the reactor.

2.2.3 **Influence of pressure**

The flammability limits of laminar premixed flames are also affected by a change in pressure. The limits for H_2 become slightly narrower with increasing pressure, while other hydrocarbons show the opposite effect with change in pressure[26]. During this research, operating the premixed flame under low-pressure conditions (typically at 30 mbar), was known to stretch the flame front. Information about the flame temperature and specie distribution within this extended front can thus be investigated with non-intrusive diagnostic methods. However, unlike the velocity of fresh gas that can be widely varied, the change in reactor pressure is limited to a small range (between 20 and 60 mbar), whereby operations outside this range can lead to either blow-off or a pulsating flame front. Increase in reactor pressure slightly increases the mean particle diameter of synthesized nanomaterials and in some cases the particle morphology [27].

2.2.4 **Influence of temperature distribution**

The temperature distribution of the 1-dimensional premixed, burner-stabilized $H_2/O_2/Ar$ flame, operated in low-pressure regimes, can be influenced by the cold gas flow, the gas mixing ratio and the inert gas content. Results from the temperature distribution has been simulated or measured with thermocouples and reported [28,29]. The obtained results often do not adequately compensate for the heat loss by radiation, which is sometimes difficult to incorporate into the measurement and analysis algorithm. The maximum flame-temperature and temperature-distribution are important for the thermal dissociation of the precursor during particle synthesis. Whereby, they influence the coagulation and coalescence steps of the particle formation process. Hence the mean particle diameter, particle size distribution and particle morphology are influenced by this factor. Furthermore, the temperature profile may determine if a doped, segregated or nanocomposite arrangement will be generated for the selected synthesis route.

2.3 **Fundamentals of gas-to-particle conversion**

Low-pressure, gas-phase synthesized materials are often characterized by small particle size, narrow particle size distribution, and spherical morphology. The most important step during gas phase synthesis is the gas-to-particle conversion, which involves several

overlapping step rapidly occurring within a very short time frame. These steps are hereby presented for both single component MO_x and multi-component material system synthesis.

2.3.1 Gas-to-particle conversion for single component metal oxide (MO_x) systems

Gas-to-particle conversion that yields a single component metal oxide (MO_x) occurs by condensation of supersaturated species in the low-pressure flame reactor. Upon introduction into the flame, some dilute precursor vapour containing the metal source such as iron pentacarbonyl $Fe(CO)_5$ is thermally dissociated, followed by a gas-phase reaction with oxygen, nucleation, and condensation of particles at lower temperatures downstream of the flame (see Figure 2.2). Other precursors such as titanium tetra-isopropoxide TTIP and tetraethoxysilane TEOS, do not require additional oxygen in order to generate the metal oxide, due to the sufficient oxygen content of the precursor. As the particle concentration increases due to condensation, the particle growth mechanism becomes more a function of coagulation, coalescence, and surface growth, which leads to a mix of agglomerated and non-agglomerated particles with varying particle diameter (see Figure 2.2).

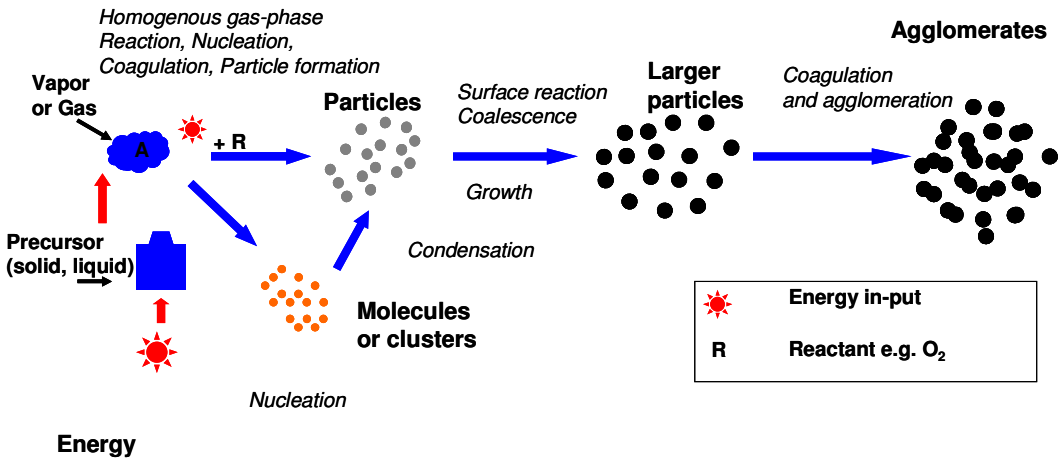

Figure 2.2: Gas-to-particle conversion for a single component powder generation [30]

Several models, theories and dissertation have been proposed to describe in detail the fluid and particle dynamics, transport, and chemical phenomena involved with gas-phase synthesis of particulate materials [31-33]. From all these methods, the *general dynamic equation* (*GDE*) is widely used to model gas-to-particle conversion [32]. It describes the aerosol dynamics with respect to the particle size distribution;

furthermore, it encompasses nucleation, condensation, coagulation and coalescence, and is expressed [34,35]as:

$$\frac{\partial n}{\partial t}+\frac{\partial (Gn)}{\partial v}-I_f(v^*)\delta(v-v^*)= \qquad (2.5)$$

$$\underline{\boldsymbol{a}} \qquad \underline{\boldsymbol{b}} \qquad\qquad \underline{\boldsymbol{c}}$$

$$\frac{1}{2}\int_0^v \beta(v-v',v')n(v-v',t)n(v',t)dv'-n(v,t)\int_0^\infty \beta(v,v')n(v',)dv'$$

$$\qquad\qquad \underline{\boldsymbol{d}} \qquad\qquad\qquad \underline{\boldsymbol{e}}$$

The property n is number concentration of the particles, v is particle volume, v^* is the critical volume, v' is the average particle volume, β is the collision frequency of the particles and t is time. The first term (**a**) in the equation describes the rate of change of the particle size distribution with time (particle concentration). The second term (**b**) involves the growth law, which represents the gain or loss of particles within a size range by condensation, while the third term (**c**) on the left hand side describes the formation of new particles with critical size $v*$ by nucleation at the rate of I_f. The other two terms (*d* and *e*), describe the gains and loss of particles within a given volume class as a result of Brownian coagulation. Equation 2.5 is however, only valid for spherical particles, and does not take into account particle diffusion as well as velocities due to external forces (e.g. thermophoresis).

2.3.1.1 **Homogenous nucleation**

Homogenous nucleation occurs when clusters grow to a size whereby the rate of formation is higher than the rate of destruction. This implies that homogenously nucleated clusters are larger than the critical cluster size [36]. Nucleated clusters are sometimes thermodynamically unstable due to evaporation and partial pressure influences, unless they are sufficiently large enough, and partial pressure conditions around the cluster is greater than vapour pressure above the curved surface of the cluster (*Kelvin effect*) [30]. Thus, the highly supersaturated state necessary for nucleation is achieved by decreasing the equilibrium vapour pressure through cooling of the gas. In order for clusters to grow and form particles, the saturation ratio (which is the ratio of the actual pressure of the specie, to the equilibrium vapour pressure over a flat surface) must be above 1.

The classical nucleation theory is one of the simplest theories used to describe homogenous nucleation. This theory though not necessarily numerically correct, is useful in establishing the dependence of nucleation rate on parameters such as surface tension and saturation ratio [32,37]. Based on this theory, the rate of formation of stable particles (I_f) from nucleation is expressed as [30]:

$$I_f = \left(\frac{P_1}{(2\pi n_1 k_B T)} \right) \left(\frac{2v_1 \sigma^{1/2}}{(k_B T)^{1/2}} \right) n_1 \exp\left(\frac{-16\pi v_1^2 \sigma^3}{3(k_B T)^3 (\ln S_{at})^2} \right) \tag{2.6}$$

From equation 2.6, the nucleation rate is strongly dependent on the surface tension term σ^3 and the saturation ratio S_{at}, whereby a 2 to 10 order of magnitude change in the saturation ratio results in a 70 order of magnitude change of the nucleation rate. Furthermore, the surface tension is material specific and can vary in many orders of magnitudes for different material. This often results in different nucleation rate for various materials synthesized under similar conditions.

After the nucleation process, particle growth can occur by one or several processes that includes; a) physical condensation of vapour onto particles, b) chemical reaction on the particle surface (surface growth), c) diffusion of a reactant into the particle, followed by a reaction within the particle. Furthermore, particle collisions (coagulation) occurring across phase transitions, and coalescence, results in larger particles, aggregates and agglomerates.

2.3.1.2 **Coagulation, Coalescence and Agglomeration**

Coagulation involves the collision of two particles, which stick to form a new, larger particle. Coagulation is interconnected to nucleation and coalescence, and describes the fusion of particles that have collided. Coagulation influences the overall particle size distribution, whereby the particle number, and surface area decreases due to the formation of larger particles. The rate of change of the concentration of particles with size v by coagulation is a measure of the particle size distribution $n(v)$, and is expressed as:

$$\frac{dn(v)}{dt} = \frac{1}{2} \int_0^v \beta(v, v-v') n(v') n(v-v') dv' - n(v) \int_0^\infty \beta(v, v') n(v') dv' \tag{2.7}$$

a **b**

In equation 2.7, $\beta(v,v')$ represents the collision frequency of two particles with volume v and v'. The first term (***a***) on the right hand side represents the formation of particles with volume v by coagulation. Double counting of collisions is avoided by multiplying the result by a factor 0.5. The second term (***b***) represents losses by coagulation of particles with volume v.

In the free molecular regime where the Knudsen number (ratio of mean free path to a characteristic length) is far greater than unity, ($Kn >> 1$), and in the absence of substantial external field forces, coagulation of spherical particles occurs by particle diffusion through the continuous gas (Brownian motion). The collision frequency β_F for Brownian coagulation in the free molecular regime is thus expressed as [32]:

$$\beta_F = K_F\left(\frac{3}{4\pi}\right)^{1/6}\left(\frac{1}{v_i}+\frac{1}{v_j}\right)^{1/2}(v_i^{1/3}+v_j^{1/3})^2 \tag{2.8}$$

$$K_F = \left(6k_BT/\rho_P\right)^{0.5} \tag{2.9}$$

Coagulation is preceded by coalescence, and is described as the fusion of particles after collision. Coalescence is dependent on temperature, material properties, particle size, and is driven by the reduction of the radius of particle volume. An approximate expression that describes the coalescence of two or more spherical particles into a single spherical particle is [38]:

$$\frac{da}{dt} = \frac{1}{\tau_f}(a-a_s) \tag{2.10}$$

The properties a_S and a represents the surface areas of a spherical particle and agglomerate respectively. From equation 2.10, the characteristic time for particle coalescence τ_f is described as the time needed to reduce the excess surface area of the agglomerate over that of a single sphere with similar mass by a factor of 0.63 [30].

Depending on the reactor system and the coalescence time, several types of particle morphology can be obtained as shown in Figure 2.3.

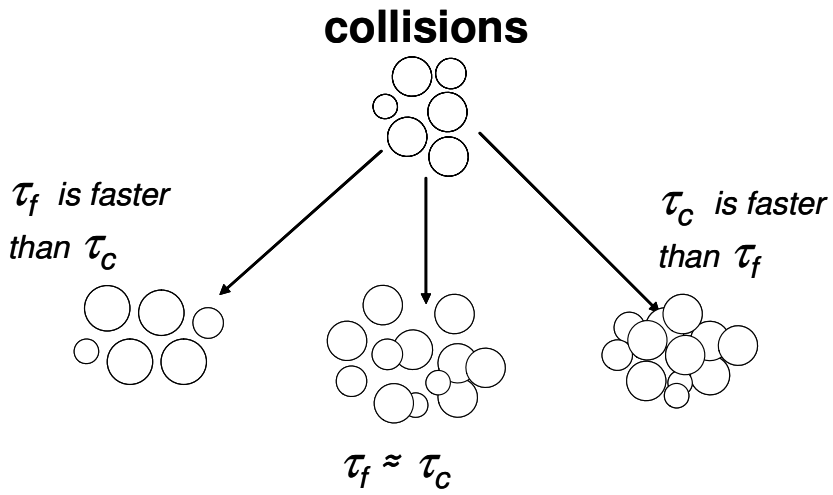

Figure 2.3: Interplay between characteristic times for coagulation and coalescence and the various particle morphologies obtainable [30]

In the first case scenario, the coalescence time τ_f is shorter than the coagulation time τ_c, that results in perfect spherical particles. Furthermore, the particle growth is not a function of the material property in this case, rather growth is collision limited. In the second case scenario, τ_f is much longer than τ_c, and particles exist as aggregates, hence growth is coalescence limited. For this case, the particle size is a function of parameters that influence coalescence, such as temperature and material properties. For most gas-phase synthesis in low-pressure reactors, the coagulation and coalescence do not particularly follow any of the two case scenarios described, and, a combination of both situations occur simultaneously, induced by the case $\tau_f \approx \tau_c$

Flame synthesized particles always consist of an ensemble of non-, soft- and hard-agglomerated particles, whereby *Pratsinis et.al* [39] reported distinctive zones during high temperature synthesis where these particles can be found. Depending on the interplay between characteristic time for coagulation and coalescence, which are influenced by experimental parameters, the degree of agglomeration of a material system can be controlled. Using silica as a model material, it was reported that the cooling rate influences the on-set of the formation of hard-agglomerates, while increased maximum temperature accelerates reaction kinetics, prolongs coalescence and facilitates the formation of larger primary particles, with low degree of agglomeration. Furthermore, increasing the precursor concentrations enhances both primary and

agglomerate particle growth, while large primary particles and small soft agglomerated particles are generated by prolonged heating time followed by instant cooling.

2.3.2 **Gas-to-particle conversion for multi-component metal oxide systems**

Gas-to-particle conversion that results in multi-component system containing two or more different metals can occur during flame synthesis of nanosized materials. Based on the precursors, the reaction kinetics of the precursors, temperature-time history, multi-component arrangements such as mixed and coated oxides can be generated [40-43]. Mixed metal oxides consist of two or more metal that are chemically bonded with oxygen in a composite arrangement such as $X_aY_bO_c$, where X and Y represents the metals, O represents oxygen, a, b are the fractions of the metals in the oxide, while c represents the oxidation state of the oxide (1, 2, 3 depending on the metals). The coated oxides arrangement involves the encapsulation of one oxide with another oxide, and unlike the mixed oxides, the oxides are chemically segregated.

The synthesis of mixed oxide in the low-pressure flame reactor is performed with two different precursors that are co-currently transported into a pre-mixing chamber in the reactor, where they mix with the combustion gases before going into the flame. Several steps can occur when multiple precursors are simultaneously exposed to high temperature sources like flames [43]. However, for the purpose of simplicity emphasis is placed on the formation of mixed oxides, which is relevant to this study. A simplified schematic illustration of possible processes involved with the formation of the multi-component oxide materials is presented in Figure 2.4:

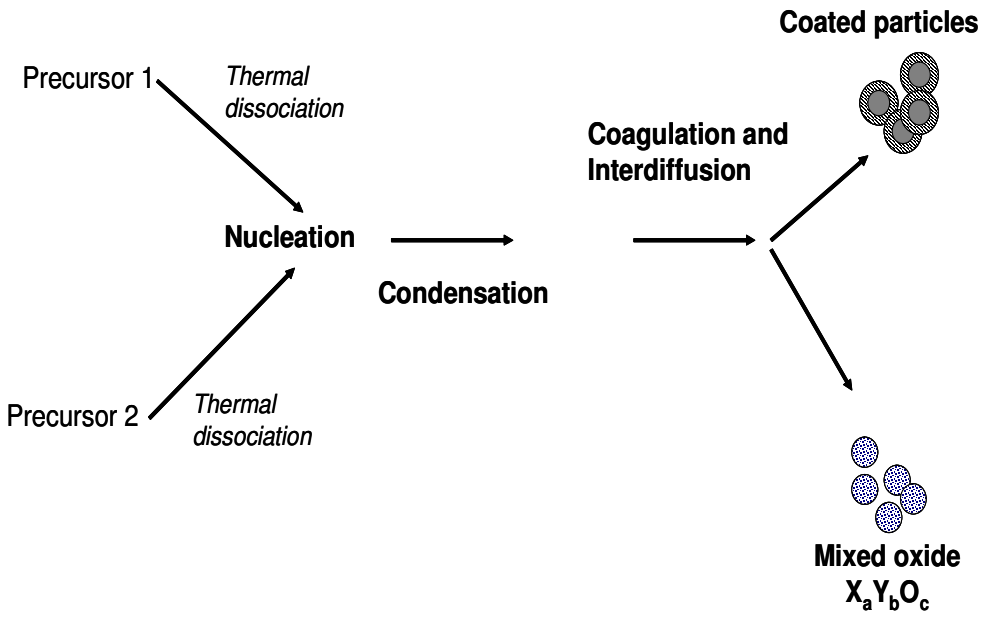

Figure 2.4: Simplified schematic illustration of gas-to particle conversion involving two precursors, which yields multi-component metal oxide systems

Upon entering the flame, the precursors undergo thermal dissociation, nucleation, condensation, coagulation and inter-diffusion. For the formation of mixed oxide particles in the low-pressure flame, the process can either be kinetically or thermodynamically controlled depending on the precursors involved [30]. Kinetic controlled mixed oxide formation, often involves chemical reactions between the metal species of the precursors with oxygen in the gas-phase. The resulting supersaturated mixed oxide condenses at lower temperatures into solid particles. Despite gas-phase formation of the mixed oxides, species distribution within the particle is not often uniform. For coated particle systems, thermodynamic controlled synthesis involves segregation of one phase to the particle surface, which is wetted and becomes the core that will be coated [44]. Kinetic controlled synthesis on the other hand is influenced by formation kinetics and vapour pressure differences between the precursors. This results in the formation of an initial material from a precursor with low vapour pressure. Downstream of the flame at lower temperatures, the second species becomes supersaturated and condenses on the surface of the initially formed material, hence creating a coated particle system. [45].

2.4 Physical and optical properties of nanosized semi-conducting metal oxides

Nanosized materials often exhibit properties different from bulk, which include Hall-Petch effect, change in band gap, as well as quantum size effect. Furthermore, particle size distribution, mean particle diameter, particle morphology and crystallinity are several properties that influence the characteristics exhibited by these materials.

2.4.1 Particle morphology

MO_x can exhibit different types of morphology, such as, cubic, rod, chain, tube, spherical etc [46-48]. Spherical, non-hollow particles are often generated from gas-phase synthesis of oxides in low-pressure flames. However, particles generated from this synthesis route often consist of both soft and hard agglomerates. Agglomerates are defined for this study as an assembly of particles rigidly joined together due to partial sintering, while aggregates are an assembly of particles loosely attached to each other. The formation of agglomerates in flames is due to incomplete coalescence as a result of reduced temperature and low residence time. The resulting particles often have morphologies that deviate from standard shapes, hence, morphologies of particle systems are characterized by their fractal dimensions D_f as shown in Figure 2.5

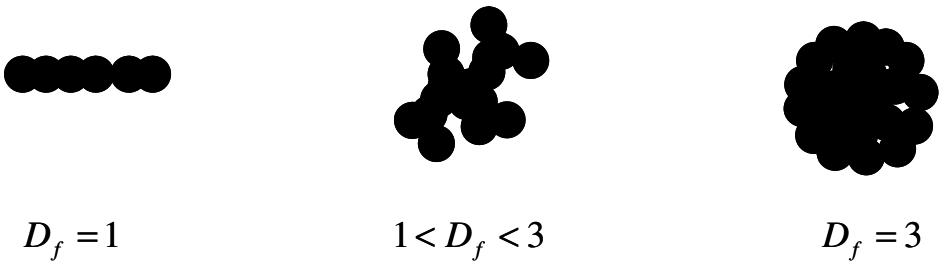

Figure 2.5: Schematic illustration of agglomerate fractal dimension

For spheres consisting of primary particles, the fractal dimension $D_f = 3$, for platelet $D_f = 2$ and for fibres $D_f = 1$. A general expression for fractal like aggregates composed of N_f primary particles is [30]:

$$N_f = \varepsilon_{pf} (2R_a / d_0)^{D_f} \tag{2.11}$$

In equation 2.11, R_a represents the characteristic length of the aggregate (radius of gyration), d_0 is the primary particle diameter, and ε_{pf} is a dimensionless pre-factor,

usually assigned a value of 1. Furthermore, the aggregate aspect ratio (which is ratio of the length to width of the aggregate), can be used to characterise and investigate changes in the particle morphology [49].

2.4.2 **Crystallinity**

Crystallinity refers to the regular repetition arrangements of atoms or molecules in a unit cell over a relatively larger distance within a particle. It plays an important role in determining the suitability of several materials for such applications like optoelectricity, catalysis, and photoluminescence [50]. Nanoparticles can either be polycrystalline, comprising of several crystallites, or single crystalline, with just one crystallite per particle. Crystallite formation for high temperature processes is determined by the atoms of the material involved, and the temperature-time history, whereby for high temperature and long residence time, ordered arrangements of atoms commonly occur.

MO_x (Al_2O_3, SnO_2, WO_3 and Ga_2O_3) synthesized in flames can exhibit several metastable or stable crystal arrangements [51,52], depending on the temperature-time history. The metastable structures can often be transformed into stable crystal arrangements via phase transition at elevated temperatures. The size of the crystallites of most flame synthesized MO_x differs slightly from the actual particle size, because the crystallite size describes the length scale above which atoms within a particle are ordered. In contrast, the particle size encompasses both the crystallite size and the amorphous layers that are often observed to encapsulate the ordered crystalline core of most flame synthesized metal oxides. The amorphous nature of the shell is due to high concentrations of atoms on the shell, which are not ordered. The relatively high concentrations of atoms on the surface of the MO_x are both electrically and coordinatively un-saturated, hence, they readily react with species in the environment to form a chemical bond, which passivates the surface of the MO_x particles. The crystallinity of metal oxides is often investigated with X-ray diffractometry (*XRD*) and high resolution-transmission electron microscope (*HR-TEM*). From the diffraction patterns obtained from *XRD* analysis, crystallite sizes can be calculated using the *Scherer's* equation

$$L = \frac{0.9 \cdot \lambda}{B \cdot Cos\theta} \tag{2.12}$$

Whereby, L is the crystallite diameter, λ is the wavelength of the X-ray and B is the full width at half maximum (*FWHM*).

2.4.3 **Hall-Petch effect**

Reducing the grain size into the nanometer range influences the mechanical properties of materials. This relationship is described by the Hall-Petch equation that relates yield stress σ_y to the grain size of a material d as shown in the equation below [53]:

$$\sigma_y = \sigma_0 + \frac{k}{d^{0.5}} \qquad 2.13$$

Where σ_0 is friction stress and k is a constant. Hence, reducing the grain size of a material from 10 μm to 10 nm increases the strength by a factor of about 30, theoretically [54]. A similar relationship exists between hardness and the grain size, whereby hardness was observed to increase with the inverse of the square root of d. This rate of increase was observed to be material specific, whereby Ni and Fe show the highest changes. Increasing interaction of dislocations with grain boundaries results in the suppression of dislocation motions. This yields a pile-up of dislocations at the grain boundaries, which is responsible for the increased hardness with decreasing grain size. However, it has been established that at low grain sizes (in nanosized range), a reverse Hall-Petch effect is observed in most materials. This was attributed to increasing diffusion accommodation of the grain boundaries, as well as superelastic behaviour at elevated temperatures.

2.4.4 **Band model**

Solid materials consist of bands composed of ensemble of atoms that are located in discrete energy levels as shown in Figure 2.6. Each band can contain 2N electrons, where N represents the number of primitive unit cells in the crystal. Electrons fill the bands, up to the Fermi energy E_F, which is determined by the total electron density [55].

Figure 2.6a represents a metal with an uneven number of electrons per atom, hence the highest occupied band will be half full and the Fermi energy exists in the middle of the highest occupied band (also known as the valence band, whereby the lowest occupied band is referred to as the conduction band). Electrons just below the Fermi energy can easily be excited above this energy with an electric field. Hence

acceleration of electrons with an electric field is relatively easy and explains why metals are excellent conductors.

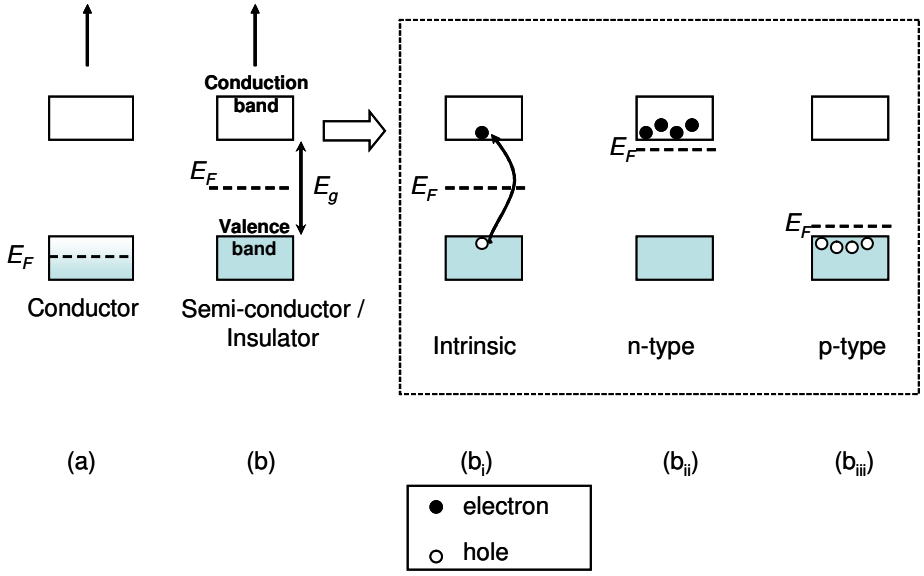

Figure 2.6: Band model for a) conductor, b) semi-conductor and insulator, $b_{i\text{-}iii}$) as well as various configurations obtainable for semi-conducting materials (options enclosed in the box)

Semi-conductor or and insulators have even number of electrons per atom, therefore the valence band is full and the Fermi energy lies between the valence and the conduction band. The next available state where electrons can jump to is the conduction band, whereby a minimum energy (band gap) is required to excite the electrons into this state. Hence semi-conductors and insulators are relatively poor conductors in comparison to metals. The difference between semi-conductors and insulators is the band gap, whereby, semi-conductors have smaller band gaps than insulators, and can conduct some degree of electricity at room temperatures. As temperature increases, the conductivity of semi-conductors improves.

Figure 2.6b_i shows the band model of a semi-conductor whereby an electron is excited from the valence band into the conduction band. The absence of the electron in the valence band creates a "hole" that behaves like a positive charge. The electron in the conduction band and the hole in the valence band can both conduct electricity, whereby, conduction by thermally excited electrons and holes in pure crystals are known as intrinsic. Other possible configurations of semi-conductors include n-type doping, where a material with an extra electron is introduced into the crystal lattice of the semi-conductor (i.e. doping of a group IV semi conductor with atoms of a group V material).

The new material (dopant) donates one extra electron for each dopant atom and the extra electrons lie in a donor state just below the conduction band. The Fermi energy must lie close to the conduction band as shown in Figure 2.6b$_{ii}$, hence the electrons can easily be excited into the conduction band at room temperature. The electrical properties of this n-type semi-conductor are determined by the extrinsic electron from the dopant atom. Another configuration is p-type doping whereby the semi-conductor is doped with a material with less electrons (i.e. doping of group IV semi-conductor with atoms of a group III material). Due to the deficiency of an electron per dopant atom, each dopant atom can accept an electron from the valence band. The acceptor levels (empty states) lie just above the valence band, hence, electrons can easily be excited to these empty states at room temperature. This creates a high concentration of holes in the valence band that determines the extrinsic electrical conductivity of this material.

2.4.5 **Band-gap**

The band gap (E_g) has previously been described as the minimum energy required to excite an electron from the valence band into the conduction band. Electrons can be excited by absorption of photon energy (light) $\hbar\omega$. However for a successful inter-band transition, the photon energy must be greater than the band gap ($\hbar\omega > E_g$). Electrons excited from the valence band into the conduction band, creates a hole in the valence band, hence inter-band absorption results in creation of electron-hole pairs.

Band gap can either be direct or indirect as shown in the *E-k* diagram of Figure 2.7. The major difference between direct and indirect band gaps is the relative position of the conduction minimum and the valence band maximum in the *Brillouin* zone.

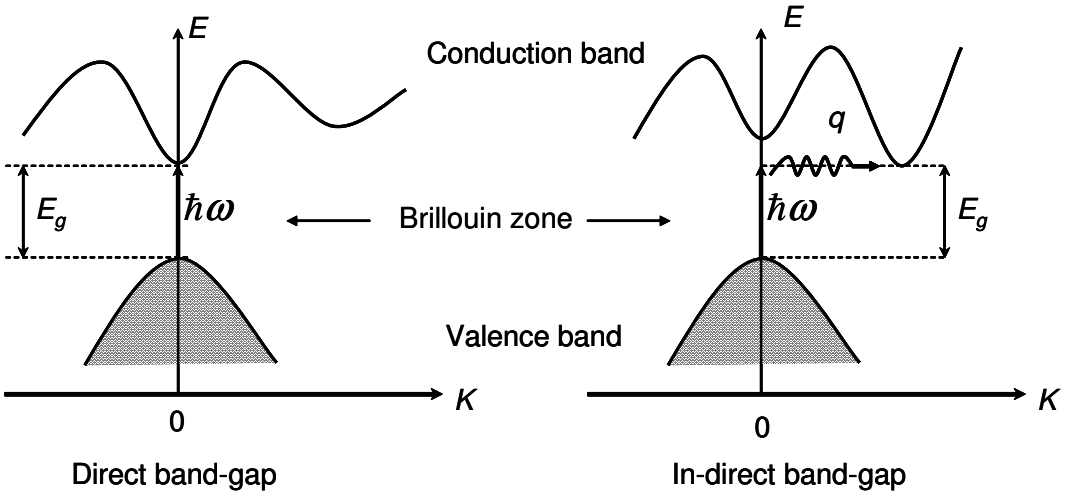

Figure 2.7: Illustrations of direct and indirect band gap of semi-conducting materials

For direct band gap materials, the conduction band minimum and valence band maximum occur at the centre of the zone at $k = 0$. However, for indirect band gap material, it occurs somewhere else at $k \neq 0$, typically near the zone edge or close to it. Furthermore, electron vector does not significantly change during photon absorption process for direct band gap materials, hence, photon absorption is represented with vertical lines in the *E-k* diagram of Figure 2.7. However, for indirect band gap, photon absorption is insufficient to excite electrons from the valence band into the conduction band. Additionally, the inter-band transition requires a phonon to conserve momentum. Phonons are atomic vibrations in the crystal lattice that have resonant frequencies in the infrared spectral region [55]. In Figure 2.7, *q* and the wavy lines represents phonon absorption or emission.

2.4.6 **Quantum size effect**

Many fundamental properties of nanosized materials such as melting point, saturation magnetization, photoluminescence differ from bulk. Quantum size effect occurs when the size of materials decrease into the nanometer range, which leads to quantum confinement of electrons and holes in all directions. Hence a shift of the band gap of materials towards higher energies (lower wavelength) is observed [56]. For nanocrystalline semi-conductors, a size dependent bad gap has been established due to quantum localization [57], which results in band gap increase.

2.4.7 **Inter-band absorption**

Inter-band transitions in materials occur when electrons jump from the lower energy state of the valence band into the conduction band, by absorption of photons with energy greater than the band gap of the material. The photon wavelength and corresponding energy values is presented in Figure 2.8. For a material with band gap of 3 eV, photon with wavelength below 413.3 nm (see Figure 2.8) is required to instigate electron excitement, which results in an electron-hole pair.

The formation of electron-hole pairs in nanosized materials fundamentally influences their photoconductivity, whereby the conductivity is proportional to the density of free electrons and holes. Therefore the conductivity increases due to the generation of free charge carriers after inter-band absorption of photons [55].

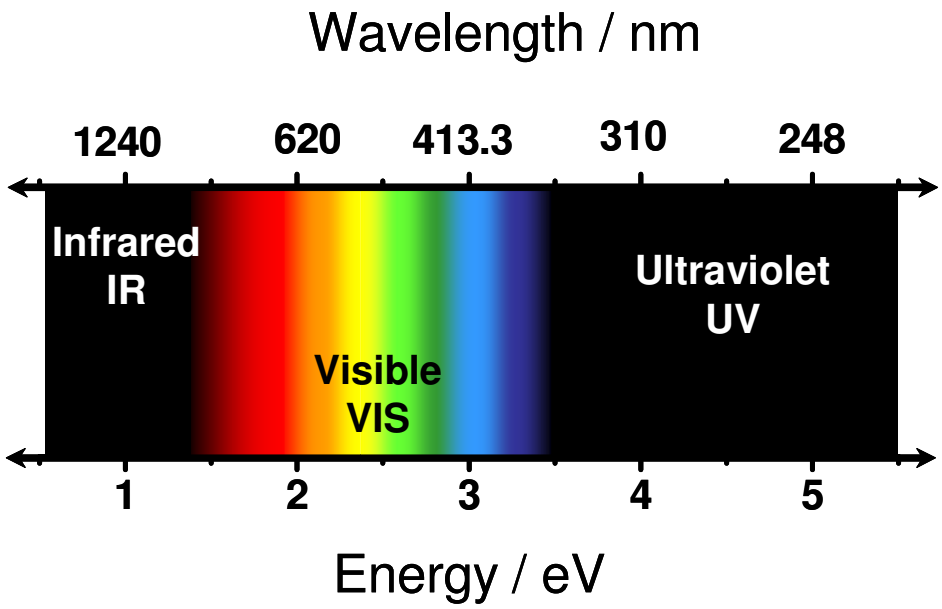

Figure 2.8: Photon spectrum in wavelength and energy showing the infrared, visible and ultraviolet regions of the spectrum

When an electron-hole pair is bound together in stable orbitals by mutual coulomb attraction between them, an exciton is formed. Excitons can exist as free excitons that are characterized by large radius and free movement within the crystal, or as tightly bound excitons with smaller radius, which are localized on individual atoms sites. The generation of electron-hole pairs in materials has been established as the basis for photocatalytic activity reported for materials like TiO_2. The mechanism for the

photocatalytic behaviour of TiO_2, is illustrated in Figure 2.9. It is based on the generation of electrons and holes upon exposure to UV light (with a wavelength of 390 nm or lower). As a result, negatively charged electrons are excited from the valence to the conduction band and react with oxygen in the environment to form super oxide anion (see left side of Figure 2.9). Consequently, the positively charged holes in the valence band dissociate water in the ambient into hydrogen, and hydroxyl radical (see right side).

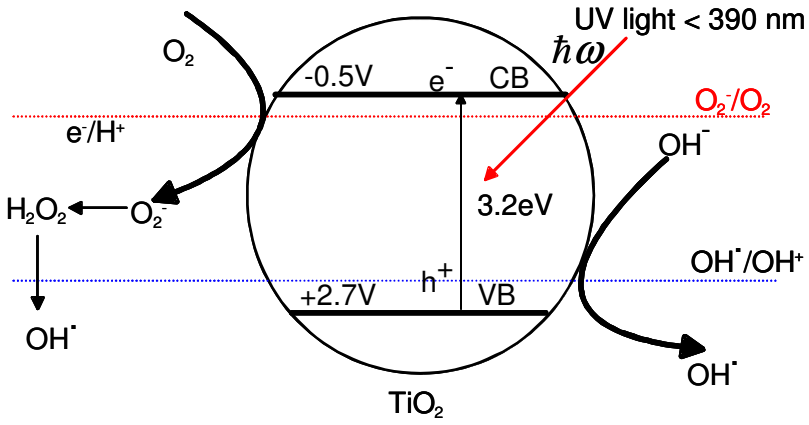

Figure 2.9: Photocatalytic mechanism in TiO_2 showing electron-hole generation and REDOX of H_2O and O_2

The radicals generated from this action consequently oxidize and reduce volatile organic compounds (*VOC*) into less complex materials that can be easily disposed.

3 Experimental set-up, in-situ and ex-situ analytical methods

The synthesis of nanosized MO_x was realised in a low-pressure premixed flame reactor. The experimental set-up includes precursor mixing and delivery systems, the low-pressure flame reactor, particle collection and sampling devices as well as an *in-situ*-particle mass spectrometer (*PMS*), coupled to the low-pressure flame reactor. A schematic of the processes involved is presented in Figure 3.1.

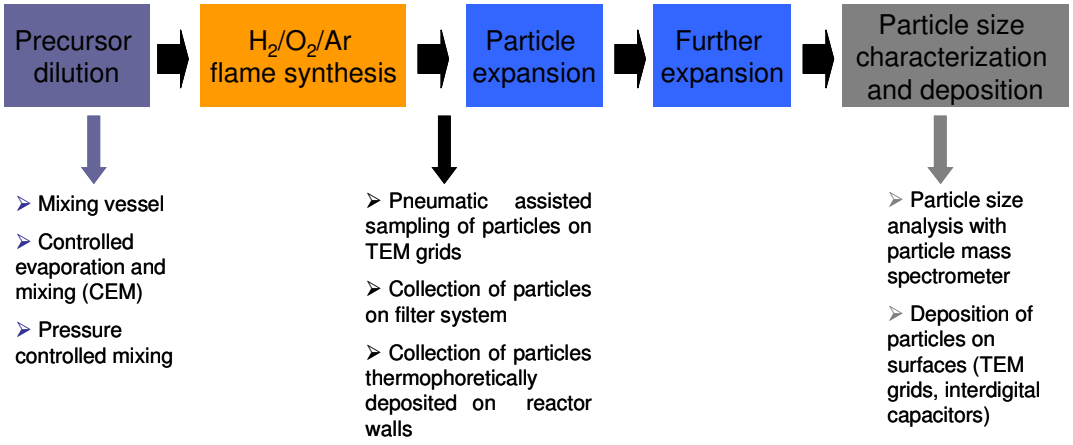

Figure 3.1: Flow sheet of process operations for MO_x nanoparticle synthesis in the low-pressure premixed H_2/O_2/Ar flame

Additionally, a non-intrusive time resolved–laser induced incandescence (*TiRe-LII*) measuring technique for particle sizing was used to independently confirm result from the *PMS* investigation, using soot as sample particle material. The detailed description of the set-ups and measuring techniques are presented in this chapter.

3.1 Precursor dilution systems

For the synthesis of MO_x nanoparticles, dilute concentrations of metalorganic precursor(s) are transported with mass flow controllers into the H_2/O_2/Ar premixed flame. Three different precursor dilution methods were used during this study, whereby the selection and suitability of each method was based on the vapour pressure of the precursor at room temperature.

3.1.1 Mixing vessel method

The mixing vessel method is based on the partial-pressure of the gases, as well as on the assumption that the gases and vapours behave like ideal gases. This method is suitable

for precursors with vapour pressure higher than 10 mbar at 25°C, and has been previously used in several investigations to dilute tetramethyl tin, iron pentacarbonyl, trimethyl aluminium and tetramethyl germanium [19,58,59]. The set-up of the mixing vessel method is illustrated in Figure 3.2

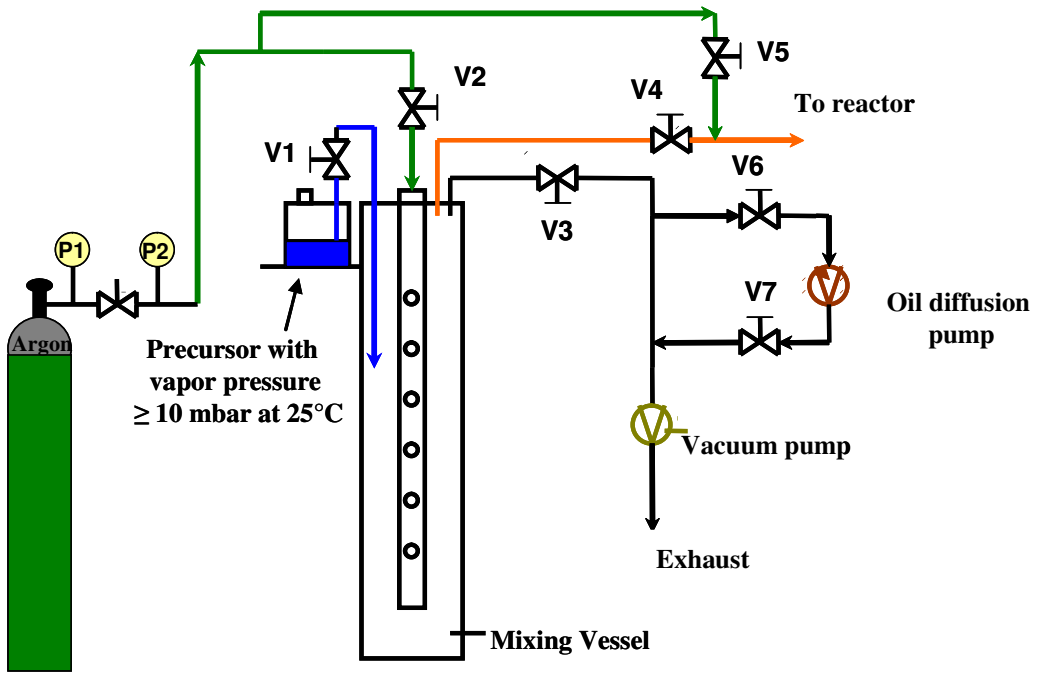

Figure 3.2: schematic of the precursor mixing vessel set-up

The 50 litres mixing vessel is initially evacuated with a combination of vacuum and oil diffusion pumps to low pressure (approx 10^{-5}mbar) conditions. Subsequently, vapour from the precursor vessel is sent into the mixing vessel by opening a valve V1 between the mixing vessel and the precursor vessel. The pressure in the mixing vessel is constantly monitored, and at 10 mbar precursor partial pressure inside the vessel, V1 is closed. Argon is then introduced into the mixing vessel through a 6 mm steel pipe via V2, until the pressure in the mixing vessel reaches 1000 mbar. The pipe extends to the bottom of the mixing vessel, whereby the end of the pipe is terminated and argon streams out from tiny openings along the pipe length into the vessel and dilutes the precursor. This design ensures some degree of turbulence, which enables the generation of a homogeneously dilute precursor mixture. This result in 1 % precursor mixture, diluted with argon, that is then sent to the reactor via 6 mm steel pipes. By varying the degree of dilution, precursor concentrations within ranging from 300 to 3000 ppm are realized with this method.

3.1.2 **Controlled evaporation and mixing**

The controlled evaporation and mixing (*CEM*™) device from *Brohnkorst Netherlands*, enables delivery of precise concentrations of diluted and evaporated liquid precursors to the reactor. This precursor dilution set-up was used for the synthesis of titania from titanium tetra isopropoxide (TTIP). TTIP has a very low vapour pressure at room temperature (below 1 mbar at 25°C), hence an alternative precursor dilution method that offers effective control of precursor concentration was employed for the synthesis. The set-up of the *CEM* shown in Figure 3.3 consists of a liquid flow meter, a mixing valve, an evaporator and a mass flow controller.

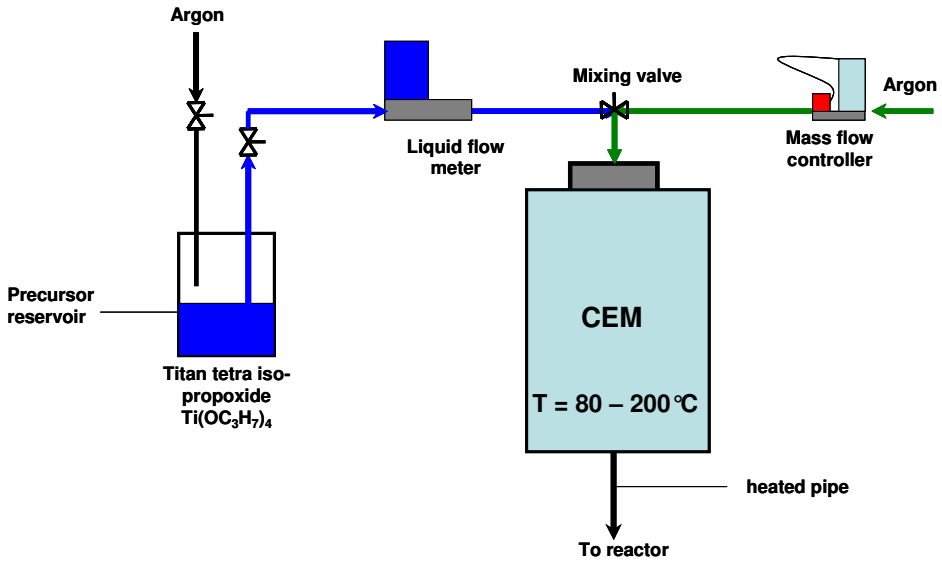

Figure 3.3: schematic presentation of the controlled evaporation and mixing device

The *CEM* device was employed for the controlled mixing and evaporation of titanium tetra isopropoxide *TTIP* [$Ti(OC_3H_7)_4$]. Typical *TTIP* mass flow rates obtainable with this method are between 0.5 to 1.5 g/h *TTIP* diluted with Argon. The precursor that was placed in a reservoir was pressurized to 3 bars by an argon stream. This pressure forces the liquid *TTIP* to flow outwards from the reservoir through a liquid flow meter towards the evaporating device. A metering valve located above the evaporator, allows a defined mass flow rate of *TTIP* to be mixed and metered with argon at the mixing valve. Depending on the required precursor dilution, a desired argon stream is regulated by a mass flow controller and both fluids flow co-currently into the evaporation chamber. In the evaporator, the premixed *TTIP* is evaporated at temperatures between 80 and 200°C. The heated precursor/argon mixture is transported into the low-pressure reactor via heated lines to prevent re-condensation of the precursor. A major advantage of the *CEM*

is the effective control of precursor concentration through accurate metering and dilution of the precursor. However, argon dilution flow rates are relatively high, which often results in the pulsation of the low-pressure flame. Secondly, condensation of the precursor occurs behind the burner head, because of the difficulties associated with completely and effectively heating the transport lines up to the flame. Therefore, precursor concentrations in the flame cannot be accurately established. These instabilities are undesirable for research purposes due to the difficulties associated with reproducing results under these conditions. Furthermore, material properties can vary widely as a result of these inconsistencies.

3.1.3 **Pressure controlled mixing**

The *CEM* device is ideal for mixing and evaporating precursors with low vapour pressure at room temperature. However, due to the high dilution flow rates (argon), required to ensure very low concentrations of precursor, the total volumetric flow rate from the *CEM* is often too high for the low-pressure flame. An alternative method to generate dilute concentrations of *TTIP* or other low-vapour pressure precursors is the pressure controlled mixing shown schematically in Figure 3.4

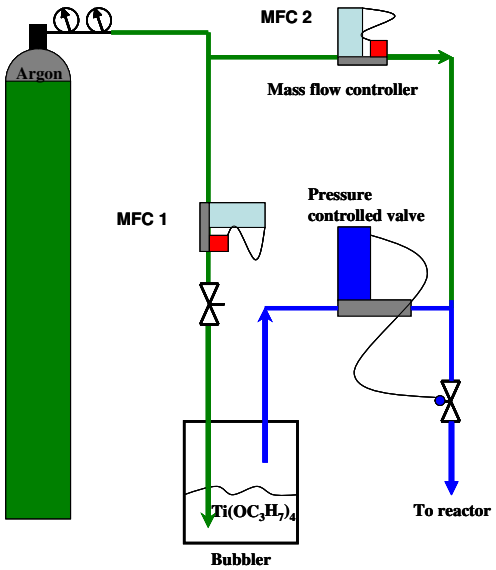

Figure 3.4: Schematic presentation of the pressure controlled mixing device set-up

This method is based on empirical calculation of precursor concentrations using the partial pressure of the precursor at different bubbler pressure. The set-up is directly attached to the low pressure reactor, therefore, the reactor pump creates vacuum conditions in the line directly connected to the reactor. A defined low flow rate of argon

is sent into the bubbler with mass flow controller MFC 1, and the argon becomes saturated with *TTIP* vapour. The concentration of the *TTIP* vapour in the saturated argon can be controlled by varying the bubbler pressure, using a pressure controlled valve attached to the transport line (*TTIP* out flow line) as shown in Figure 3.4. The valve that is connected to the low-pressure reactor, adjusts the bubbler pressure to the set value, which influences the amount of TTIP that is in the gas phase. The saturated *TTIP*/argon mixture consequently flows out of the bubbler towards the low-pressure reactor into the flame. In other to further control the concentration of TTIP/argon mixture going into the reactor, additional argon is metered by a mass flow controller MFC 2 via the by-pass line. The major advantage of this set-up is that it enables generation of dilute concentrations of low vapour pressure precursors at room temperature, without heating up the set-up and transport system. Furthermore, due to the relatively low volumetric flow rate, this system does not significantly affect the stability of the flame, unlike the *CEM*. Typical *TTIP* concentration levels obtainable with this method are from 300 to 10000 ppm, depending on precursor vessel pressure.

3.2 **Flame synthesis of metal oxide nanoparticles**

Nanosized metal oxide particles were generated during this study in a low-pressure, burner-stabilized premixed $H_2/O_2/Ar$ flame reactor with peripheral equipment connected to the reactor. Low-pressure synthesis was selected because pressure offers an additional parameter that can be varied to influence the material properties. Furthermore, low-pressure conditions cause a stretched reaction zone that can be investigated for information on flame temperature and atom specie concentration. A schematic illustration of the particle synthesis set-up is illustrated in Figure 3.5. It consists of the combustion gases bottles (H_2, O_2, C_2H_4, Ar), mass flow controllers, vacuum and oil diffusion pumps, as well as the reactor, which is divided into the synthesis, expansion and analysis chambers. Furthermore, thermophoretic sampling device, particle filter system and particle mass spectrometer are attached.

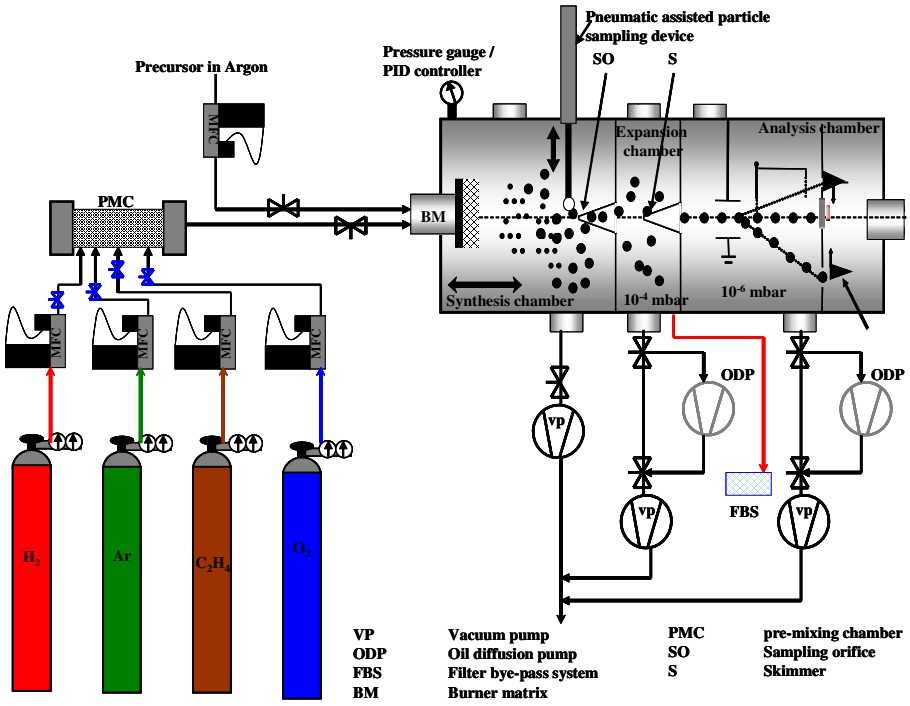

Figure 3.5: Schematic presentation of low-pressure premixed H_2/O_2/Ar flame reactor

3.2.1 **The low-pressure flame reactor**

The low-pressure premixed flame reactor consists of 3 cylindrical chambers (combustion, expansion and analysis), operated at different vacuum conditions. The reactor chamber shown in Figure 3.6 has optical windows for process visualization, vacuum pump connections, heated filament for flame ignition and sampling orifice for aerosol expansion.

According to Figure 3.6, the combustion gases are initially delivered by mass flow controllers to a pre-mixing chamber filled with glass pearls to stimulate intensive mixing. The premixed combustion gases consequently flow into the reactor to the water cooled burner matrix where the flame is ignited and stabilized. For visualization and controlled ignition purposes, the flame is initially generated with a C_2H_4/O_2/Ar mixture flowing over an electrically heated tungsten wire. Once the flame has been ignited; the C_2H_4 flow is systematically reduced while the H_2 flow is increased as the flame fuel source. The precursor(s), diluted with argon, using one of the 3 dilution techniques previously described, is consequently introduced into the reactor by a mass flow controller(s). The diluted precursor and the combustion gases temporarily mix in a chamber directly behind the burner matrix to ensure homogenous distribution, before entering the colourless H_2/O_2/Ar flame. The pressure in the synthesis chamber of the

reactor can be varied between 20 and 50 mbar with a *PID* pressure controller. Upon entering the flame, the diluted precursor is dissociated, followed by exothermic gas-phase reaction, which yields a supersaturated vapour of a metal oxide. Down stream of the flame at lower temperatures, the vapour condenses into particles that grow by coagulation, coalescence and surface growth (see schematic in Figure 3.6). The synthesized particles are deposited thermophoretically on a cooled substrate in the synthesis chamber, as well as on the walls of a filter system attached to the reactor.

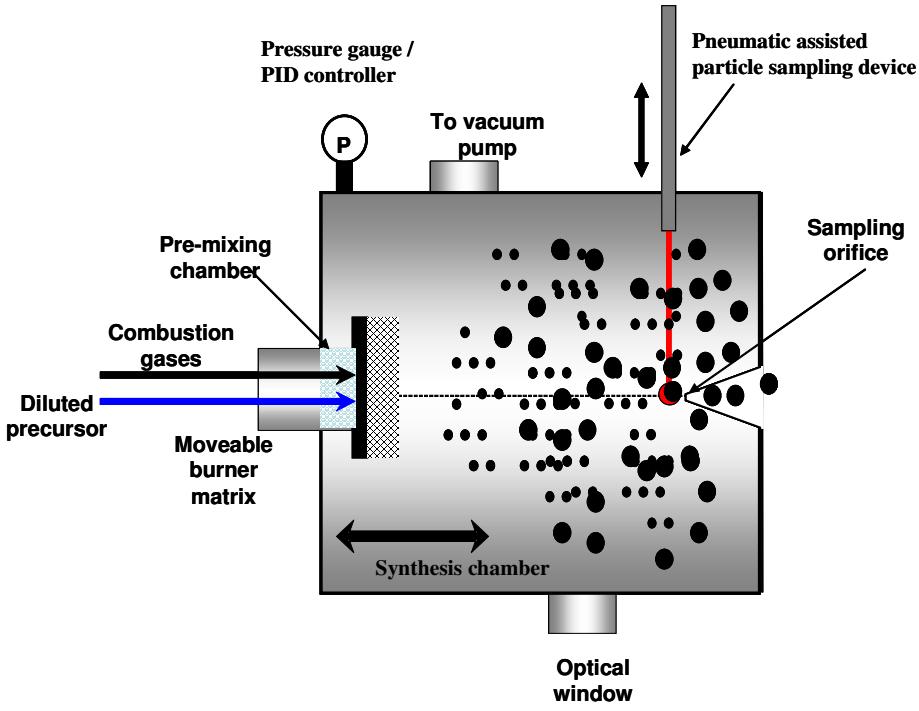

Figure 3.6: Schematic illustration of the combustion chamber of the low-pressure premixed flame reactor

3.2.2 Thermophoretic sampling of particles and pneumatic assisted sampling

Some particles synthesized in the flame reactor are thermophoretically sampled on a water cooled plate downstream of the flame. The sampled particles are then characterized by ex-situ methods or used directly for applications. Thermophoresis as described by Hinds [33], refers to the migration of particles due to a temperature gradient. A model that describes thermophoresis in free molecular region ($Kn >, 1$), indicate that hot gas molecules, due to high thermal velocity, transfer a higher impulse to particles than colder molecules during gas-molecule particle collision. This influences particles migrating towards lower temperatures, with relatively insignificant influence on the particle size. Expressions for the thermophoretic power and velocity

show that they are functions of the gas-phase pressure, temperature gradient, gas molecule mean free path, particle temperature, particle diameter and kinematic viscosity of the gas [33]. Thermophoresis in the low-pressure reactor is due to cooling of the external reactor walls by convection at ambient conditions. This is an unwanted phenomenon, although as a result, macroscopic quantities of particles can be collected for quantitative analysis from the internal walls of the combustion chamber. Wanted thermophoresis is achieved on a water cooled plate located in the combustion chamber. Particles thermophoretically sampled on this cooled plate are collected after synthesis by gentling scraping off the film with a spatula into a container.

For the investigation of the particle size distribution, morphology, crystallinity and degree of agglomeration, thermophoretically sampled particles were analyzed by transmission electron microscopy (*TEM*). For this purpose, pneumatic assisted sampling of particles on *TEM* grids at a position very close to the sampling orifice is often performed (see illustration in Figure 3.6). This method that was used and described in detail elsewhere [27], involves the rapid insertion into the synthesis chamber of a *TEM* grid placed in a holder on a pneumatic cylinder. The residence time of the *TEM* grid in the chamber can electronically be controlled and ranges from 15 to 500 ms. Despite the intrusive nature of this method, the insertion into the combustion chamber is rapid (see Figure 3.6) but parallel to flow of combustion aerosol. Therefore, particles are thermophoretically deposited on the *TEM* grids and the distortion of the flame profile is negligible. The short residence time in the synthesis chamber and comparatively low temperature of the *TEM* grid, prevents further growth of particles sampled on the *TEM* grid.

3.2.3 **Filter by-pass system**

The synthesized particles were also collected on a filter by-pass system schematically shown in Figure 3.7. The essence of this filter was to trap particles entrained by the vacuum pump of the combustion chamber, so as to prevent deposition of the particles in the pumping system.

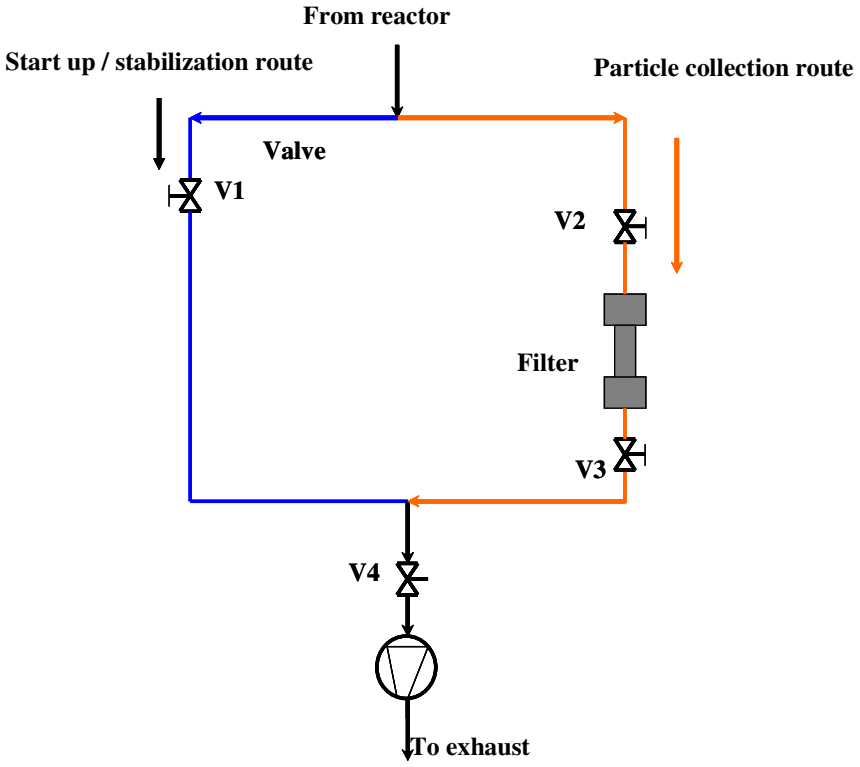

Figure 3.7: Schematic illustration of the filter by-pass system

The filter system consists of a start-up and stabilization route, through which the gaseous exhaust products of the combustion process flows through. Before flame ignition, valves V1 and V4 are opened while V2 and V3 are closed to achieve the pressure necessary for flame ignition. After flame ignition and introduction of precursor (particle formation is occurring), V2 and V4 are opened, followed by simultaneous closure of V1. Synthesized particles laden in the reaction mixture but entrained by the vacuum pump, are trapped in a cylindrical paper filter system (25 x 100 mm) positioned in the filter, seen Figure 3.7. During the synthesis process, the pores of the filter become covered, leading to gradual pressure drop in the synthesis chamber. A change of filter is thus required and can be performed without stopping the experiment by switching to the start-up and stabilization route. Based on this enhanced recovery system, increased quantities of synthesized MO_x can be obtained from the flame reactor.

3.3 Particle mass spectrometer (PMS)

A major property of nanomaterials that influences their unique properties is the particle diameter and consequently the particle size distribution. It has been reported that changes in mean particle diameter of Fe_2O_3 can result in either ferromagnetism or

superparamagnetism [60]. Investigating and controlling the mean particle diameter during synthesis is therefore important for generating functional materials for specific applications. During the synthesis of MO_x nanoparticles, an in-situ particle mass spectrometer (*PMS*), coupled to the flame reactor was used to investigate the particle size distribution of the materials. The *PMS* schematically illustrated in Figure 3.8, shows the nozzle (sampling orifice) and a skimmer both located downstream of the flame in the synthesis and expansion chambers respectively [61].

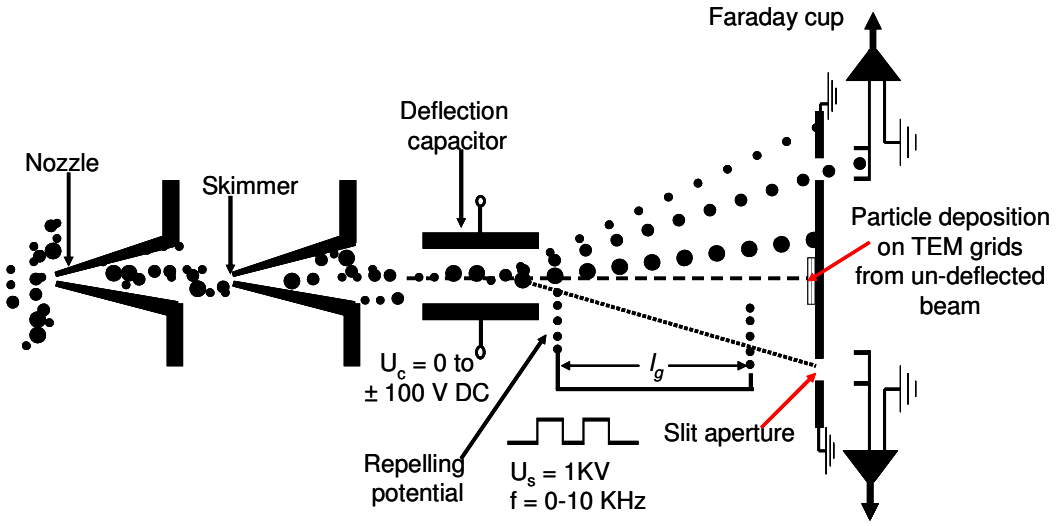

Figure 3.8: Schematic presentation of the particle mass spectrometer (*PMS*) showing particle deposition possibility [61]

Due to the pressure difference in the chambers (30, 10^{-4} and 10^{-6} mbar), sample aerosols are continuously extracted from the synthesis chamber into the expansion chamber. The centre of the expanded aerosol is further expanded through a skimmer into the low-pressure analysis chamber, resulting in a particle laden molecular beam, which can be analyzed with the *PMS* or deposited on substrates for ex-situ analysis. The deposition of particles in the molecular beam on substrates within the analysis chamber, is described as the "molecular beam assisted particle deposition method" (*MBAPD*). This method was used extensively for transmission electron microscope (*TEM)* analysis and impedance spectroscopic (IS) analysis of metal oxides synthesized in the low-pressure reactor.

The *PMS,* which is based on the behaviour of charged particles in an electric field, consist of a deflection capacitor with length l_k, width b_k and an aperture at a

distance L_{PMS} from the deflection capacitor, and Faraday-cups behind an aperture for particle charge detection (see Figure 3.9) [61].

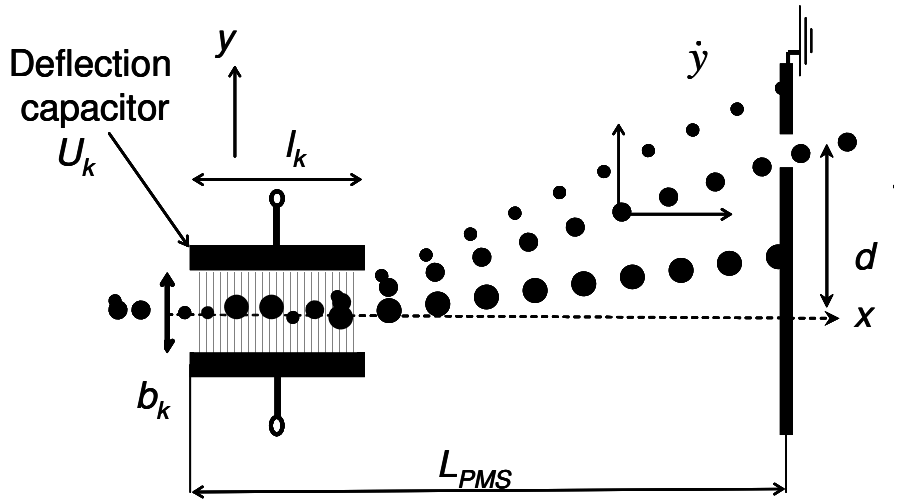

Figure 3.9: Schematic of particle deflection within the PMS

During operation, a charged particle-laden molecular beam centrally enters the deflection capacitor that consists of two parallel plates. An electric field is generated by introducing a scanning voltage U_k between the parallel plates of the capacitor. The charged particle is deflected from its original path along a trajectory. Based on the condition that the electric field exists only within the capacitor plates, and the field lines are orthogonal to the capacitor surface, the electric field strength can be mathematically represented as $\left|\vec{E}\right| = U_k / b_k$. The deflected charged particle, experiences a force of $\left|\vec{F}_y\right| = n_e e U_k / b_k$ which is perpendicular to the capacitor surface. With respect to its mass, the consequent acceleration and deflection of the charged particle away from it original trajectory (*x*-direction) is expressed as:

$$\ddot{y} = n_e \cdot e \cdot U_k / b_k \cdot m_p \tag{3.1}$$

The trajectory of the particle in the deflection capacitor can be calculated with the following equations [62]:

$$y = 0.5 \cdot n_e \cdot e \cdot U_k / (b_k \cdot m_p) t^2 \qquad x = v_p \cdot t \tag{3.2}$$

$$\dot{y} = n_e \cdot e \cdot U_k / (b_k \cdot m_p) t \qquad \dot{x} = v_p \tag{3.3}$$

Since the electric field does not extend beyond the capacitor parallel plates, there is no further deflection in the *y*-direction, and hence the particle continues along a straight trajectory. The trajectory can then be calculated, taking into consideration the constant velocity components $\dot{x}$ and $\dot{y}$ as follows:

$$y = n_e \cdot e \cdot U_k \big/ (v_p^2 \cdot m_p) \cdot l_k / b_k \cdot (x - l_k/2) \qquad \text{for } x \geq l_k \qquad (3.4)$$

Every particle with mass m_p and charge n_e has a distinctive path, therefore, the previously focused molecular beam is expanded into a fan of trajectories as a result of the deflections. Mass selection is thus achieved by filtering the trajectories with an aperture located downstream of the deflection capacitor at a distance $x = L_{PMS}$ in the *x*-direction, with an aperture size of Δd and a distance of $y = d$ from the centre axis in the *y*-direction. Therefore, to calculate the kinetic energy of the deflected particle, the following equation is required:

$$E_{kin} = \frac{1}{2} \cdot m_p v_p^2 = U_k \cdot n_e \cdot e \cdot \frac{l_k}{b_k} \cdot \left(\frac{2 \cdot l}{d} - \frac{l_k}{d} \right) \qquad (3.5)$$

The geometric dimension of the *PMS* and the value of an elementary charge e = 1.6 x 10^{-19} C are computed into a constant (K_{PMS}). By re-arranging equation 3.5, the mass of the particle that was deflected with a voltage of U_k, and passes the aperture, can be calculated when the particle velocity and number of elementary charges per particle is known:

$$m_p = K_{PMS} \cdot n_e \cdot U_k \big/ v_p^2 \qquad (3.6)$$

The value of the constant K_{PMS} for the purpose of this research is $4.31 \cdot 10^{-18}$ J/V. The *PMS* analysis with regard to particle size is based on the assumption that all particles are spherical, have an elementary charge and the velocities of the particles are equal (*Fuchs theory*) [63].

For the successful characterization of the particle size distribution with the *PMS*, the particles have to be charged, the particle velocity and the number of elementary charges on the particles are required. The charging mechanism is assumed to be a result of diffusive transport of ions to particles, which are transported within the gas medium. The charges result from thermal electron emission, which occurs during the combustion process. The charging probability has nearly a Boltzman distribution and can be described by *Fuchs theory* [63], whereby, for particles larger than 20 nm, a 32 %

probability for one elementary charge and 1 % for binary charge was postulated. Hence, the possibility of binary charging for particles below 10 nm is almost zero, therefore, it can be assumed that most of the particles synthesized in the low-pressure reactor have one elementary charge. A typical *PMS* signal is shown in Figure 3.10.

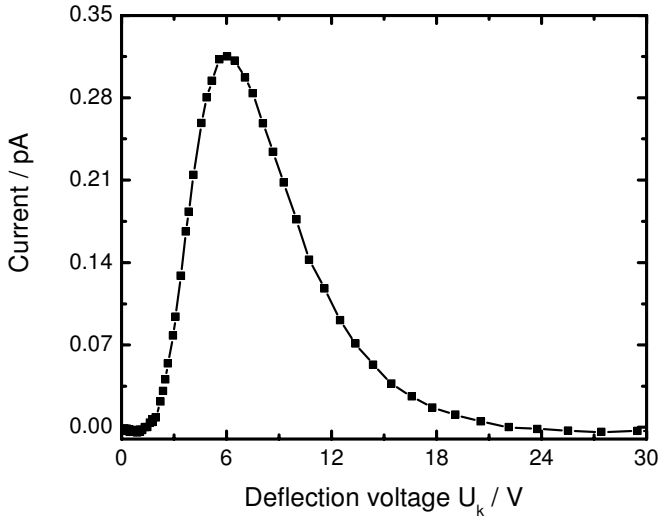

Figure 3.10: Typical *PMS* signal for nanosized particles synthesized in the low-pressure flame reactor

It is presented as a deflection-voltage *vs*. particle-current plot. The maximum current detected within a given time interval was for $U_k = 6$ V. For the computation of the particle size distribution, the particle velocity is thus required. This is measured with a "chopping device" that is schematically illustrated in Figure 3.11.

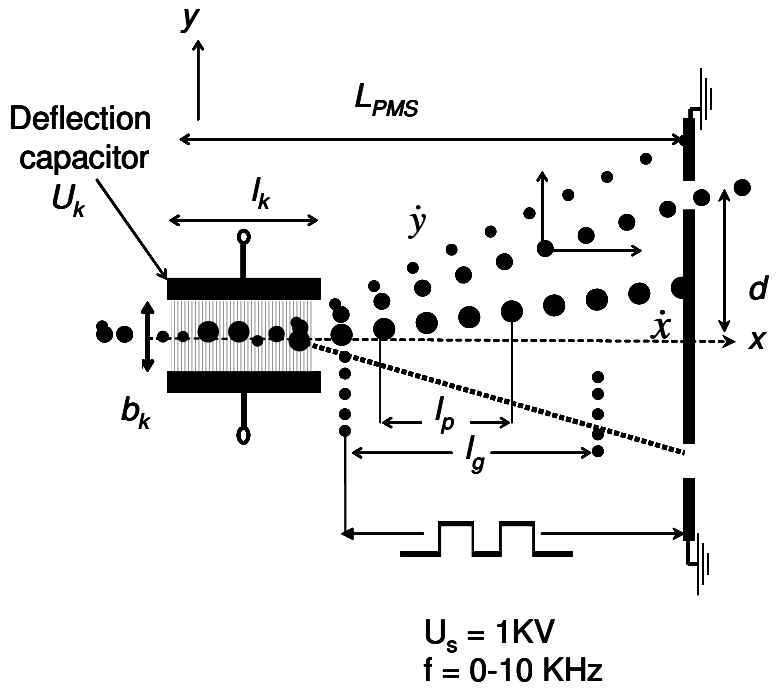

Figure 3.11: Schematic of *PMS* velocity measurement

The measurement begins with the selected beam of charged particles passing through two grids in series, supplied with synchronously repelling potentials. The upper grid form packages of charged particles that go through at zero potential, but are repelled when the voltage is increased to 1 KV. The length of the packages l_p is a function of the frequency of the grid voltage f and the particle velocity v_p. Only very few or no particles pass through the second grid if the package length l_p is an odd-numbered multiple of the grid distance. By changing the frequency of the deflection voltage U_k, a fluctuating particle current I_p with maxima and minima is obtained that obeys the following conditions [61]:

$$v_p = 2 \cdot f_{\min,i} \cdot l_{p,i} \tag{3.7}$$

$$l_{p,i} = l_g, \frac{l_g}{3}, \frac{l_g}{5}, etc$$

Equation 3.7 describes the determination of the particle velocity, whereby the frequencies $f_{\min,i}$ that causes a minimum of current flux I_p, has to be determined [61]. The first minimum of the velocity signal that must satisfy the expression $l_{p,i} \equiv l_g$ can be difficult to identify from the frequency dependent signal of the velocity measurement. Hence it was established that the difference between two minima corresponds to:

$$\Delta f_{\min} = 2 \cdot f_{\min,i} \tag{3.8}$$

The sensitivity of the *PMS* at higher deflection voltages increases due to disproportionate evaluation of the current for higher particle mass [61]. Therefore the *PMS* signal (voltage/current) plot does not represent the probability density function (*PDF*) of the distribution. The *PDF* can thus be obtained from the *PMS* signal by averaging the measured particle current $I(U_k)$ with a factor $U_{k,O}/U_k$, whereby $U_{k,O}$ represents an arbitrary reference voltage. The *PDF* is then expressed as follows:

$$PDF(m_p) \propto U_{k,O} \cdot \frac{I(U_k)}{U_k} \tag{3.9}$$

A typical velocity measurement signal for nanosized particles is presented as a current *vs*. frequency plot in Figure 3.12.

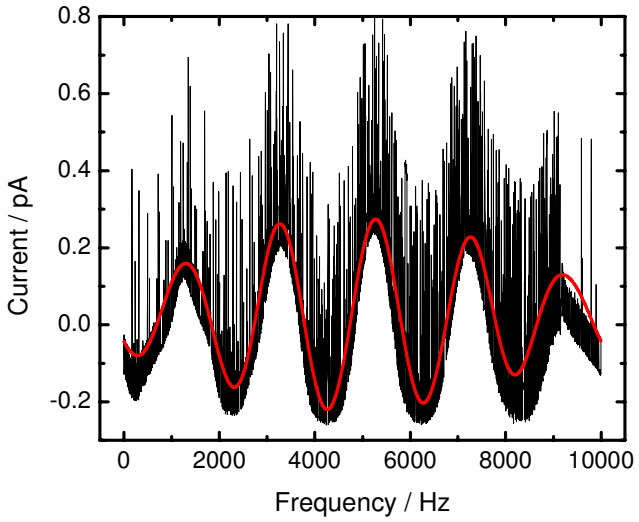

Figure 3.12: Velocity measurement signal for SnO_2 particles synthesized in the low-pressure reactor

The black lines represent the raw signal obtained from measuring the particle velocity, while the red curve represents a fit of the original signal. From Figure 3.12, a particle velocity v_p = 507 m/s was calculated. Based on the assumption that the particles have spherical morphology, the probability density function *PDF* of the synthesized particles can therefore be calculated with the particle velocity v_p, the signal from Figure 3.10, equations 3.6 and 3.9, as well as the bulk density of the particle. A typical example of the calculated particle mass distribution is shown in Figure 3.13. The particle size

distribution is calculated from the mass distribution and presented as the insert in Figure 3.13.

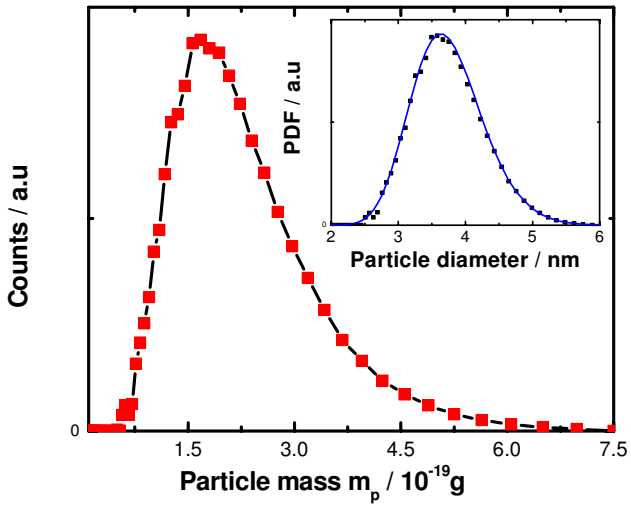

Figure 3.13: Typical particle mass distribution and particle size distribution for MO_x nanoparticles synthesized in the low-pressure flame reactor.

The count mean diameter (*CMD*) and the geometric standard deviation (σ_g) of the synthesized MO_x can be obtained by analyzing the size distribution (insert in Figure 3.13) with a log normal function. The relationship between the *CMD*, and σ_g is expressed as follows:

$$f\left(d_p^0\right) = \frac{1}{\sqrt{2\pi}\cdot d_p \cdot \ln\sigma_g} \exp\left[\frac{(\ln d_p - \ln CMD)^2}{2(\ln\sigma_g)^2}\right]\partial d_p \qquad (3.10)$$

The *CMD* represents a statistical mean of the particle size, while the σ_g indicates the percentage of the sample particle with diameters that deviate from the *CMD*.

3.4 Laser induced incandescence

Online characterization of nanoparticle sizes was performed using the in-situ particle mass spectrometer (*PMS*). The result obtained from the *PMS* is often validated with ex-situ methods such as *TEM* image analysis and *BET* particle surface characterization that do not provide real time information of the size distribution. An alternative non-intrusive, real time particle sizing method is the time resolved laser induced incandescence (*TiRe-LII*). It involves rapid heating of particles with a short laser pulse

up to high temperatures, and consequently detecting its cooling profile with respect to time, by measuring the laser induced particle radiation. This profile can thus be correlated to the volume of a spherical particle, which can be computed to obtain a count mean diameter. The *TiRe-LII* has previously been applied to particle sizing in various reactors and diesel engines successfully [64,65].

3.4.1 **Theory of TiRe-LII**

The TiRe-LII is based on time resolved detection of the particle's radiation, which has been heated up to very high temperatures by very short laser pulse. The model, which was used for this investigation was developed by [66] and further improved in [67].

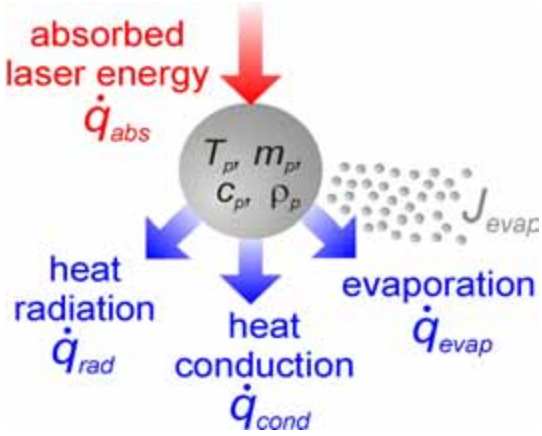

Figure 3.14: Energy and mass balance of a single spherical particle during heating [67]

It is based on the energy and mass balance of a single spherical particle during heating and cooling as illustrated in Figure 3.14. For *TiRe-LII* analysis, the particles are heated to maximum temperatures (max temp = T_p^0), whereby the temperature is measured with two colour pyrometry. Consequently, the particle size as a function of cooling time is calculated with numerical solutions of differential equation systems. It is assumed that there is a distinct separation between the heating and cooling periods (no overlaps). The heat and mass fluxes involved when a single particle is heated by a short laser pulse is expressed as:

$$\frac{d}{dt}(m_p \cdot c_p \cdot T_p) = \dot{q}_{abs} - \dot{q}_{cond} - \dot{q}_{rad} - \dot{q}_{evap} \tag{3.11}$$

$$\frac{dm_p}{dt} = -J_{evap} \tag{3.12}$$

The term $\dot{q}_{abs}$ represents energy absorption of the particle and is expressed as :

$$\dot{q}_{abs} = m_p \bar{c}_p \frac{dT_p}{dt} \tag{3.13}$$

The other terms in equation 3.10, describe energy loses by radiation, conduction, and evaporation. The expression ignores energy fluxes due to particle oxidation, thermal annealing and thermionic electron emissions [68]. The energy loss by conduction in the free molecular regime (Kn>>1) can be expressed by the following equation:

$$\dot{q}_{cond} = \frac{\alpha_T \cdot \pi \cdot d_p^2 \cdot p_g \cdot c_{tg}}{8} \left(\frac{\kappa+1}{\kappa-1} \right) \left(\frac{T_p}{T_g} - 1 \right) \tag{3.14}$$

In this equation α_T is the translational energy accommodation coefficient, which describes the efficiency of energy transfer during molecular collision. The other properties include the heat flux by radiation, which is expressed as:

$$\dot{q}_{rad} = \pi \cdot d_p^2 \cdot \varepsilon \cdot \sigma \cdot (T_p^4 - T_g^4) \tag{3.15}$$

The total emission coefficient ε was assumed to be 1.00 for the purpose of this research, while σ represents the Stefan-Boltzmann constant.

The heat flux due to evaporation is dependent on the evaporation enthalpy Δh_v and rate of evaporation J_{evap} :

$$\dot{q}_{evap} = J_{evap} \cdot \Delta h_v \tag{3.16}$$

$$J_{evap} = \alpha_V \cdot 0.25 \cdot \pi \cdot d_p^2 \cdot c_{td} (\rho_s - \rho_\infty) \tag{3.17}$$

From equation 3.15, a mass accommodation coefficient α_V = 1.0 was assumed for this investigation. The densities at the particle surface and infinity ρ_s , ρ_∞ respectively, are represented in equation 3.15 whereby ρ_s can be calculated with the *Clausius-Clapeyron* equation

3.4.1.1 **Particle heating**

The maximum temperature T_p^0 reached by the particle after absorption of laser energy is required as a necessary input to model the cooling profile of the particle. For spherical particles, absorption of electromagnetic radiation is described by *Mie theory* [69], which

states that the heat up temperature T_p^0 is independent of the particle diameter, for particles with diameters far much smaller than the laser wavelength (Rayleigh limit).

Alternatively, two-colour pyrometry can be applied for the experimental determination of T_p^0 without involving the complex refractive index term. However, the particle emission signals S_P at two different wavelengths λ_1 and λ_2 are required to calculate the particle temperature. Calibration for this method is performed with a black body radiation and assuming a refractive index for the laser wavelength. The following expression is valid for particles within the Rayleigh limit:

$$\frac{\varepsilon_P(\lambda_2)}{\varepsilon_P(\lambda_1)} \approx \frac{\lambda_1}{\lambda_2} \tag{3.18}$$

Therefore, the maximum particle temperature T_p reached is assumed to be similar to the maximum temperature of the particle T_p^0 that absorbs the laser energy.

3.4.1.2 **Particle cooling**

TiRe-LII of soot particles in the flame reactor is performed under low-pressure conditions. Soot particles were selected as a model material for this investigation because of the relative success in measuring it in diesel engines [65]. Hence measurement of soot particles synthesized in the low-pressure flame reactor with *TiRe-LII* serves as a basis for investigating the applicability of this measuring technique in this reactor. The success of this process can thus be extended to metal oxide synthesis in the low-pressure reactor.

The influence of pressure on the three heat fluxes (radiation, conduction and evaporation) involved with particle cooling for a 15 nm carbon particle is hereby presented in Figure 3.15. It shows the heat fluxes for particles dispersed in argon at various heat-up temperatures for pressures of 45 mbar and 1000 mbar, respectively. The heat fluxes from evaporation and radiation are independent of pressures from 1000 mbar and below. In contrast, the heat flux as a result of heat conduction is pressure dependent, whereby at atmospheric pressure a linear dependence on the particle temperature is observed. However, at low-pressure conditions heat conduction is almost zero for the relevant particle temperature regions and thus has no effect on particle cooling. Due to the free molecular conditions in the combustion chamber of the low-pressure reactor, only few collisions occur between particles and surrounding gas

molecules, hence particle cooling by heat conduction is suppressed. At low particle temperatures, the heat flux is due to radiation, while at higher particle temperatures (above 3000 K) evaporation becomes the dominant heat loss mechanism.

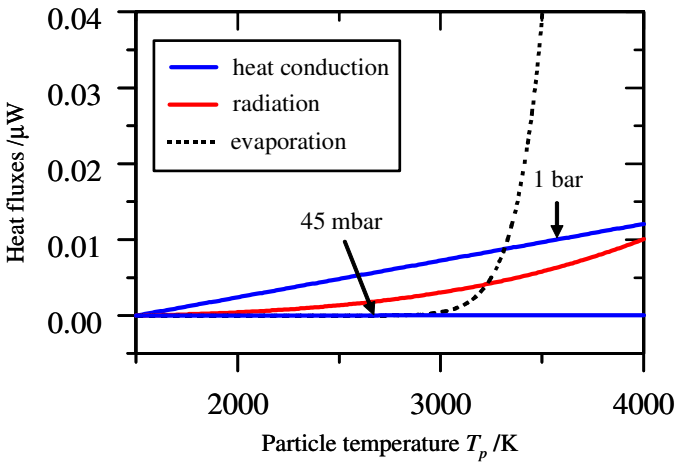

Figure 3.15: Pressure influence on heat fluxes affecting particle cooling [67]

The emission signal at the detection wavelength $\lambda_{\text{detection}}$ is a fundamental input for the *TiRe-LII* analysis, whereby this signal can be related to a particle temperature using Planck's law [70]. The measured radiation is a summation of various particle diameters that represents a polydisperse size distribution, typical for nanosized particles synthesized in the flame under low-pressure conditions.

3.4.2 *TiRe-LII* experimental set-up

The *TiRe-LII* set-up for particle size analysis in the low-pressure flame reactor consists of a laser and an optical detection unit as schematically presented in Figure 3.16. The laser used for this analysis is an *Nd:YAG* laser (spectron SL 454G-10) with a wavelength of 1064 nm. The particles are heated with the laser having a beam diameter of 8 mm and pulse energy of up to 500 mJ, for pulse duration of 6 ns. However, for the validation experiments with soot particles, pulse energy of 240 mJ that corresponds to energy density of 0.48 J/cm^2 was used. The laser beam was adjusted to sample particles at the entrance of the sampling nozzle located downstream of the premixed flame in the reactor. The essence of this localized measurement is to ensure that particles sampled and analyzed with the *PMS* are identical to *TiRe-LII* analyzed particles. The laser beam after passing the sampling spot is absorbed by a beam dump made of a non-reflective black body.

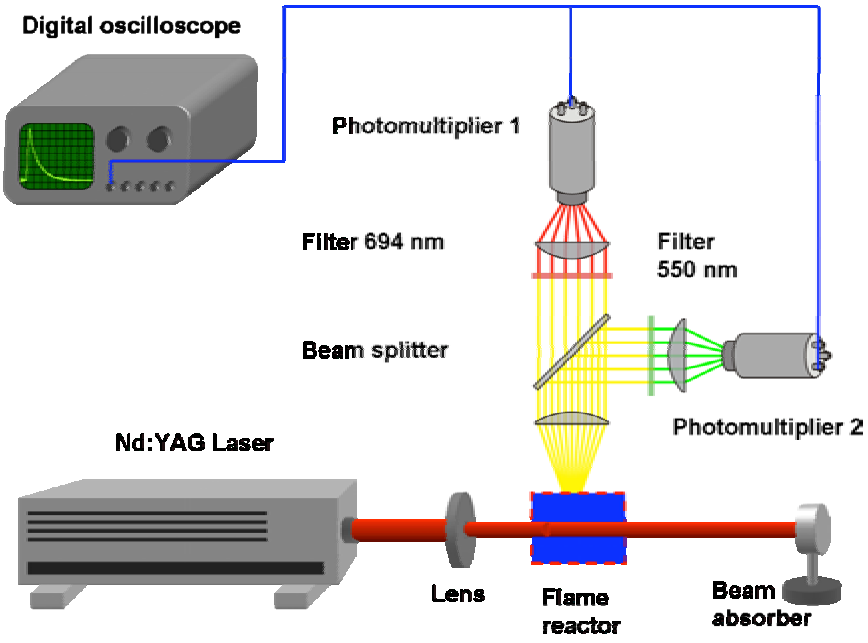

Figure 3.16: Schematic presentation of the *TiRe-LII* set-up for particle size analysis in the low-pressure flame reactor

The signal detection system is arranged perpendicular to the laser beam axis and consists of an optical lens with a focal length f_L = 150 mm and diameter = 50 mm. The optical lens focuses all the signals from particles heated at the localized sampling position in the combustion chamber. A beam splitter located within the optical detection unit, splits a part of the signal (50/50) by 90°, resulting in 2 signal beam paths. Narrow band filters with centre wavelength at 550 and 694 nm (*FWHM* = 10 nm) are placed along each path and collecting lenses with f_L = 50 mm (diameter = 50 mm) focus the signal on the cathodes of two high speed photomultipliers (*PM*). The *PMs* are integrated with amplifiers (SMT MEA 1030 V8DA with HAMAMATSU R7400U-04, rise time τ = 0.78 ns), and the signals are digitalized and stored by a 1-GHz digital oscilloscope (LeCroy LC584AXL). The oscilloscope samples at a rate of 2Gs/s that corresponds to a 0.5 ns time resolution.

3.5 Ex-situ characterization techniques

After the synthesis of MO_x particles in the synthesis zone of the low-pressure premixed H_2/O_2/Ar flame reactor, the generated particles were collected for different ex-situ analyses. These investigations include X-ray diffraction (*XRD),* Brunauer-Emmett-Teller absorption isothermal (*BET),* High resolution-transmission electron

microscope (*(HR)TEM),* Ultraviolet-Visible spectroscopy (*UV-VIS)*, and Impedance spectroscopy (*IS*), are designed to deliver information about the physical and unique properties of the nanosized materials. The theoretical descriptions of the physics behind these characterization techniques are hereby presented.

3.5.1 **X-ray diffraction (XRD)**

X-ray diffraction is a non-destructive method used to determine information about the chemical composition and crystal structure of both naturally occurring as well as synthesized materials [71]. Furthermore, the presence of impurity in the crystal lattice of another material can be detected in some cases with *XRD* analysis.

Atoms within a crystal are located in a 3-dimemsional lattice. This arrangement can be described as a series of parallel levels, whereby the levels are separated from each other by a specific distance (*d*) called lattice planes, which is crystal structure specific. During *XRD* measurement, a Bragg reflection is observed when a monochromatic X-ray beam with a wavelength (λ) is incident upon a crystalline material at a defined angel (Θ), and the distance of the lattice planes with respect to λ corresponds to:

$$n\lambda = 2d\sin\Theta \tag{3.19}$$

Whereby *n* is an integer and is usually assigned a unit value. By varying the incident angle (Θ), the intensities of the Bragg reflection for polycrystalline materials can be detected, measured and presented in a diffractogram. For crystalline materials, Bragg reflections with relative intensities are observed for defined 2Θ values. These relative intensities coupled with 2Θ values can be assigned to a specific material, thus it is used as a material characterization technique. Furthermore, the crystallite size (*L*) of the material can be calculated with the full width at half maximum (*FWHM*) (*B*), obtained from the Bragg reflections of the diffractogram and *Scherrer's* equation:

$$L = \frac{0.94 \cdot \lambda}{B \cdot Cos\Theta} \tag{3.20}$$

The crystallite size does not represent the mean particle diameter of the material and thus differs slightly from it. However, it provides critical information on how large the crystallites are. The crystallite size is closely related to the mean particle diameter and often used to indicate its tendency.

A *Panalytic X'pert MSD* X-ray device with either cobalt or copper X-ray source was used for the diffraction analysis of the MO_x powders synthesized in the low-pressure flame. The diffractometer is equipped with a highly sensitive semi-conductor for obtaining highly resolved Bragg reflections. For the XRD investigation, slurry of the metal oxide made by mixing the MOx powder with a few drops of non-polar cyclohexane was placed on a silicon single crystal substrate. The slurry was evenly distributed on the substrate, after which it was exposed to an X-ray beam. The substrate was set at a speed of 2 rotations per second so as to enable even exposure of the slurry to the beam. Analysis of the patterns obtained from the XRD investigation were consequently performed with the aid of a database software *X'pert High score* from *Panalytic*.

3.5.2 **Brunauer-Emmett-Teller (BET) absorption isothermal**

BET Nitrogen absorption is a widely used surface area characterization technique, based on the adsorption of gas molecules on the surface of solid materials (MO_x). This method is based on the extension of the *Langmuir* theory for monolayer to multilayer adsorption [72], and was established by **Brunauer, Emmett** and **Teller** (*BET*). From this analysis, a total surface area S_{total} and a specific surface area are computed with the monolayer adsorbed gas quantity (v_m), Avogadro's number (N), adsorption cross section (s), molecular weight of adsorbate (M), and weight of sample solid (a_{wt}), as shown in the following equations:

$$S_{total} = \frac{(v_m N s)}{M} \tag{3.21}$$

$$S = \frac{S_{total}}{a_{wt}} \tag{3.22}$$

The *BET* specific surface obtained (S) can be converted to a particle diameter with the density of the material and the assumption that the particle has a spherical morphology. The particle diameter is obtained with the following equation:

$$D = \frac{6}{S\rho} \tag{3.23}$$

Whereby (D) is the *BET* diameter of the particle.

A *Nova 1000* from Quantachrome *BET* measuring equipment was used in the course of this research. This equipment includes a heating and vacuum station for thermally desorbing volatile organic compounds adsorbed on the surface of powders to be investigated. A 5 point *BET* measurement procedure was typically used for powders investigated during this research.

3.5.3 *UV-Vis* spectroscopy

UV-Vis spectroscopy is a fundamental, optical analytical method for investigating the reflection, transmission and absorption properties of multi-phase materials (gas, liquids and solids). It is used to obtain information on sample materials (nanoparticles) such as optical band gap, blue shift, quantum size effects, as well as directly measure the absorption edge of the material. The absorption edge is defined as the transition between the strong short-wavelength and the weak long wavelength absorption in the spectrum of the semi-conducting solid. The spectral position of this edge is determined by the energy separation between the valence and the conduction bands of the material. Several types of *UV-Vis* investigation methods exist, and the choice of technique is often guided by the nature of the material to be investigated (i.e. solid or liquid), as well as the information required about the material. However, for the purpose of this research nanosized materials were investigated with the diffuse reflectance method of *UV-Vis* analysis that uses a praying mantis *DRA* (diffuse reflectance accessory). For this method, light is projected on the sample material, horizontally positioned in the spectrophotometer (*UV-Vis* measuring equipment). Diffusely reflected light from the sample is collected by two large hemispherical mirrors positioned above the sample. The reflected light is then directed towards the instrument detector, where information on the optical properties of the material is registered.

A varian carry 400 UV-Vis spectrophotometer designed for diffuse reflectance analysis was used. The powder samples were placed inside a sampling cup provided with the praying mantis accessory. The cup was overfilled with sample materials into a mound that was then flattened with a blade along the surface of the mound, to create a 3 mm diameter sample surface. Variation of surface flatness and parking density were minimized by making the sample as flat and densely parked as possible. A baseline correction was performed using Teflon™ placed in a sample cup in the same manner as the sample material. This was followed by diffuse reflectance analysis of the material that results in a spectrum graphically displayed as percentage reflectance against

wavelength of the light beam. From the detected reflection, a spectrum based on the absorption and scattering coefficient is obtained. This spectrum, which is based on the absorption and scattering coefficient of the sample material, is described by the *kubelka* and *munk* expression [73]. This expression defines the scattering relationship as a function of the particle size and wavelength of incident beam. From the *UV-Vis* spectrum, information about the material band gap can be extrapolated and calculated, while changes in the absorption edge due to doping, presence of impurities, or blue shift based on quantum size effect can be observed.

3.5.4 **Transmission electron microscopes (TEM and HRTEM)**

The transmission electron microscopes functions similarly like a light microscope, however, electrons are focused on a substrate as a thin beam with the aid of an electromagnetic lens instead of a light beam [74]. Unlike in light microscope where magnification is limited by the wavelength of the incident photon, the wavelength of electrons can be tuned and exhibit both wave-like and particle functions. Therefore, when accelerated by an electric field and focused by electric and magnetic fields, electrons can act like a beam of radiation, whereby the wavelength is dependent on their energy, which can be varied by changing the flux of the accelerating field. This result is a far lower wavelength than light and the electrons can still interact with substrates due to its charges.

For the purpose of this research investigation, a *TEM* (Philips CM12) and a high resolution transmission electron microscope *HRTEM* (FEI Technai 20) were employed for microscopic investigation of particles deposited on TEM micrographs. The *TEM* with a maximum resolution of 750000 was mainly used to visualize particle size ($d_p > 2$ nm) and morphology, degree of agglomeration, particle composition (energy dispersive X-ray spectroscopy *EDX*) and to some extent crystallinity through diffraction patterns. The *HRTEM* with a maximum resolution of 10^6 is equipped with electron energy loss spectroscopy (*EELS*) for investigating atomic compositions of materials. Furthermore detailed *EDX* and diffraction patterns can be obtained due to its higher resolution.

3.5.5 **Impedance spectroscopy IS**

Impedance spectroscopy (*IS*) is a useful method to characterize the electrical properties of MO_x nanoparticles. The process involves the applying an electrical stimulus (voltage

or current) to materials (deposited between two electrodes, or 4-point measurement), and investigating the corresponding response [75]. This process is performed with the basic assumption that the properties of the electrode-sample system do not vary with time. The objective of *IS* is to obtain information on the variation of the intrinsic properties of the sample materials based on parameters such as temperature, stoichiometry and surrounding atmosphere. Several microscopic processes, which contribute to the overall electrical response of the sample system, occur when the electrode-sample system is electrically stimulated. These processes include:

a) transport of electrons through the electronic conductors

b) transfer of electrons between electrode-sample interface

c) flow of charged atoms via defects in the sample system

Several methods exist to induce stimuli for *IS* measurement. However, the most common approach (method used for this research) involves the measurement of impedance directly in the frequency domain by applying a single-frequency voltage to the interface. This is consequently followed by measuring the phase shift (real part Z'), as well as the amplitude (imaginary part Z'') of the resulting current at that frequency. The impedance measurement can be performed over a wide frequency range from mHz to MHz. The intrinsic properties, which can be measured by IS are broadly divided into 2 categories. The first group consists of properties that are related to the materials such as conductivity, dielectric constant and charge mobility equilibrium. The other group consists of properties such as adsorption-reaction rate constant, capacitance of the interface region, and diffusion coefficient of neutral species that relate to the electrode-sample interface.

IS signals can be presented in a nyquist diagram, whereby the *X*-axis represents the real part Z', while the *Y*-axis represents the imaginary part Z''. The experiments are typically performed within a specific temperature and frequency range. The analysis of the *IS* data is performed based on a detailed electrical model consisting of passive electronic devices such as resistors, capacitors and inductors. The experimental impedance data can be analyzed using fitting algorithms and comparing it to equivalent circuits consisting of these devices. Some sample combinations describing different transport processes are shown in Figure 3.17.

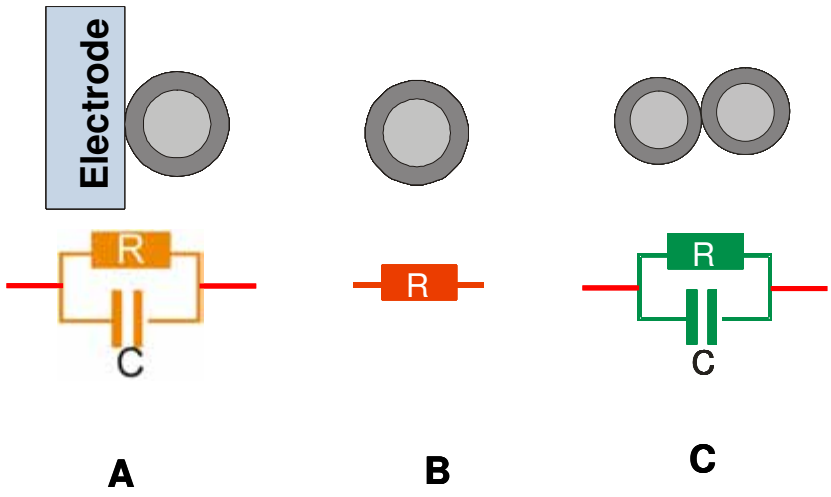

Figure 3.17: *RC* circuits representing a) electrode-sample interaction; b) sample particle; c) particle-particle interaction.

As can be seen from Figure 3.17, the charge carrier transport process can thus be described for (A) an electrode-particle system, (B) through a single particle and (C) particle-particle system. By means of the special fit algorithms, contributions from A, B and C can be separated and their activation energy calculated, from an Arrhenius plot of their conductivity σ_c as shown below:

$$G = G_0 \cdot e^{-Ea/k \cdot T} \tag{3.24}$$

Whereby: $G \rightarrow \frac{1}{z} \rightarrow \sigma_c$

G represents the conductance, which is directly proportional to the conductivity, but inversely proportional to the resistivity of the material.

For impedance measurements, a Solatron SI 1255 frequency response analyzer (FRA) in combination with a dielectric interface SI 1296 was used in the frequency range between 1 Hz and 1MHz with 17 points per decade. The control of the FRA, the data recording and the temperature adjustment were realized with a computer.

4 Synthesis of particles in a low-pressure flame

The results of the synthesis and characterization studies performed on several single and mixed oxide nanoparticles are presented in this chapter. Emphasis is placed on the effects of experimental parameters during synthesis on the physical properties of the oxide materials. In this chapter the results of the synthesis of tin oxides, tungsten oxides, titanium dioxide as well as mixed tin-titanium oxide are presented. Furthermore, results on the implementation of an optical *in-situ* particle sizing technique for on-line determination of mean particle diameter in the low-pressure flame reactor are presented.

4.1 Metal oxides synthesis in the low-pressure flame

The objectives of this study were to investigate the synthesis of nanosized metal oxide particles in the premixed low-pressure flame and consequently characterize the properties associated with these materials. The optical and electrical properties of these materials were characterized by *UV-VIS* reflectance spectroscopy, and impedance spectroscopy. Other physical properties such as particle size distribution, crystallinity, and surface area were also analyzed. Before presenting the results from synthesis of the metal oxides, it is important to report some information on 2D-flame temperature measurement of the H_2/O_2/Ar premixed flame, operated in low-pressure conditions. The importance of these results cannot be over emphasized due to the strong influence of the temperature on the particle size, morphology and to some extent crystallinity.

The maximum flame-temperature from the synthesis process is influenced by the equivalence ratio ϕ of the flame. For a 1-dimensioanl premixed H_2/O_2/Ar flame, with equivalence ratios $\phi = 0.667$ and 0.375, temperatures corresponding to 1379 and 1306 K ± 25 K, respectively, have been measured with NO-laser induced fluorescence (*NO-LIF*). The overall temperature profile of the flame is presented in Figure 4.1

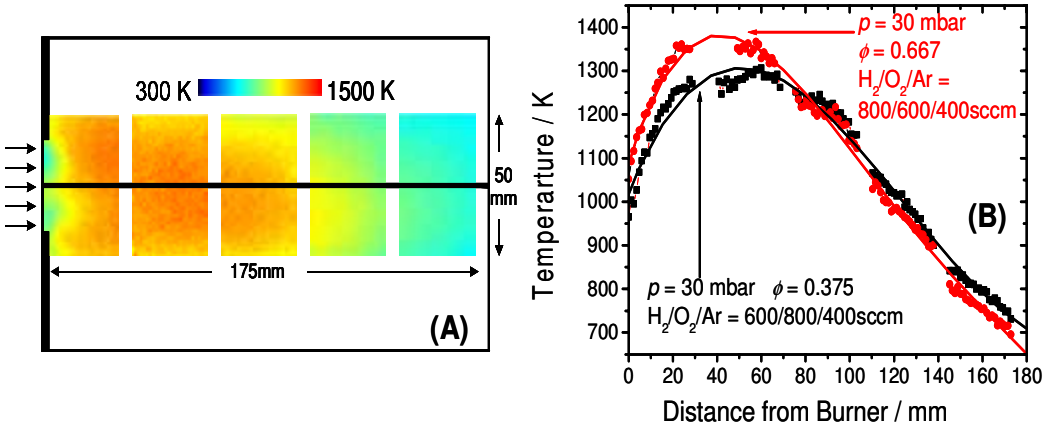

Figure 4.1: a) 2D-NO-LIF temperature distribution of an isobaric premixed $H_2/O_2/Ar$ flame along a low-pressure reactor; b) Corresponding temperature profiles for different equivalence ratios

The advantage of this method over previously referenced methods is that it is calibration free and non-intrusive [76,77]. The two ϕ-values used, represent the range of fuel/oxidant ratios often selected for synthesis of metal oxide nanoparticles MO_x. Despite the difference in the maximum flame temperature for both ϕ, the cooling profiles downstream of the flame appear similar. This identical profile can be attributed to non-adiabatic conditions that exist in the reactor due to heat loss on the reactor wall.

The maximum flame temperature varies between 1250 and 1375 K depending on the equivalence ratio selected. Furthermore, the maximum flame temperature was observed to increase with increasing reactor pressure due to increased reactions per unit volume. The maximum flame temperature is generally not significantly affected by low concentrations of metalorganic precursors (200-300 ppm). However, different precursors (carbonyls, metalorganics, and halogen based precursors) may exhibit different chemistry in a high temperature environment, which results in a slight temperature deviation. For example, tungsten hexafluoride (WF_6) was observed to slightly slow the flame chemistry of the 1-dimmsiaonl premixed $H_2/O_2/Ar$ flame, resulting in a lower maximum flame temperature. In contrast, iron pentacarbonyl $Fe(CO)_5$ creates a luminous flame, whereby, the maximum flame temperature increases slightly by about 100 K.

4.1.1 **Synthesis of SnO_2 nanoparticles**

The synthesis of nanosized SnO_2 nanoparticles was achieved by doping the low-pressure flame, stabilized on a water cooled bronze matrix, with dilute concentrations of tetramethyl tin (*TMT*) $Sn(CH_3)_4$. The properties of this precursor is presented in Table 7.1 in Appendix A. Synthesis of SnO_2 in diffusion flames have been reported previously [49,78], however, the objective of this study was to use a premixed $H_2/O_2/Ar$ flat flame operated in low-pressure conditions to investigate the synthesis of SnO_2 nanoparticles. Working under low-pressure conditions, creates a stretched flame front that can be investigated with non-intrusive spectroscopic methods for information on atom concentration and flame temperature distribution. Furthermore, with this arrangement, pressure becomes an additional parameter that can be used to influence the physical properties of SnO_2 nanoparticles.

For the synthesis of tin oxide nanoparticles, 1 % *TMT* diluted with 99 % Ar by volume was realized in the mixing vessel. The experimental conditions used are as follows:

TMT concentration	300 – 1000 ppm
Reactor pressure P_D	30 – 50 mbar
H_2 / O_2 ratio	0.6 – 0.75
Inlet gas velocity v_u	1.32 m/s
Height above burner *HAB*	40 – 200 mm

For simplicity sake, the synthesis of SnO_2 from *TMT* precursor will be represented with the following single step reaction:

$$Sn(CH_3)_4 + 8O_2 \rightarrow SnO_2 + 6H_2O_{(g)} + 4CO_{2(g)} \qquad 4.1$$

The process begins with the thermal dissociation of *TMT*, yielding *Sn* radical that reacts with oxygen to form a supersaturated vapour of SnO_2 that condenses into particles at lower temperatures downstream of the flame. The synthesized SnO_2 particles were consequently characterized to determine their physical properties, as well as possible changes with respect to varying experimental parameters. Some reported properties of bulk SnO_2 are presented in Table 7.2 in Appendix A.

4.1.2 Characterization of flame synthesized SnO_2 nanoparticles

The characterization of the flame synthesized SnO_2 nanoparticles is broadly divided into *in-situ* (particle mass spectroscopy *PMS*), and *ex-situ* characterization methods (X-ray diffraction spectroscopy *XRD*, Transmission electron microscopy *TEM*, ultra-violet spectroscopy *UV-Vis*, impedance spectroscopy (*IS*).

4.1.2.1 Particle mass spectrometry

The particle mass spectrometer (*PMS*) was used during this investigation to obtain real time information on the particle size distribution of SnO_2 nanoparticle during the synthesis process. The *PMS* was consequently used to study the effect of height above burner (*HAB*), precursor concentration C_P, and reactor pressure P_D, on the mean particle diameter and geometric standard deviation σ_g of the synthesized materials. A typical *PMS* signal and velocity measurement of SnO_2 nanoparticles is presented in Figure 4.2. A maximum current of 0.29 pA was detected at a deflection voltage of 6.5 V for SnO_2 particles synthesized at height above burner (*HAB*) = 90 mm, C_{TMT} = 300 ppm.

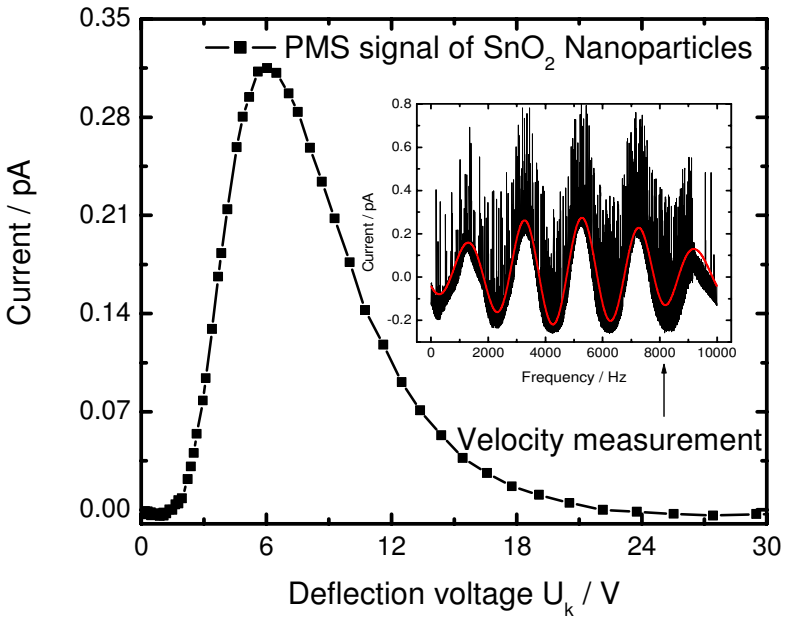

Figure 4.2: PMS signal and velocity measurement (insert) of at *HAB* = 90 mm, H_2/O_2 = 0.95, Ar / (H_2 + O_2) = 0.505, C_{TMT} = 300 ppm

The particle size distribution was determined with the bulk density of the material (see appendix A) and the information obtained from Figure 4.2. The result is presented in

Figure 4.3, from which the PDF parameters of $CMD = 3.9$ nm and $\sigma_g = 1.15$, were determined.

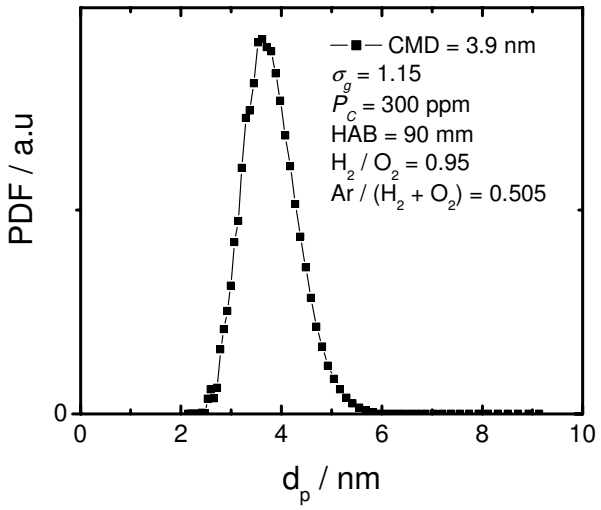

Figure 4.3: PDF of the particle diameter of of SnO2 nanoparticles determined from Figure 4.2

The influence of height above burner (*HAB*) on the mean particle diameter is presented in Figure 4.4. The error bars represent the geometric standard deviation of the particle size distribution.

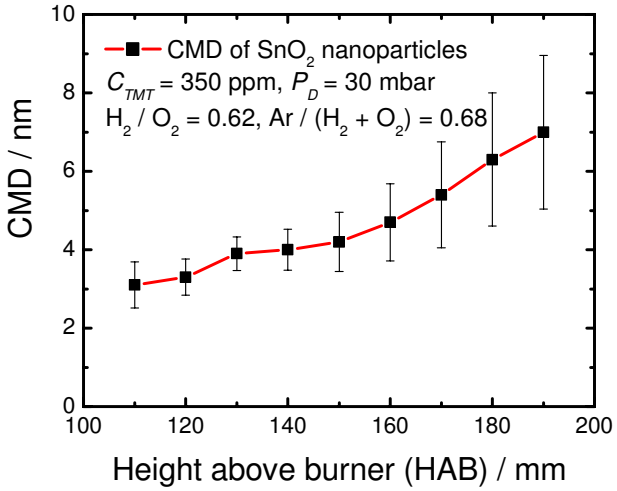

Figure 4.4: Influence of *HAB* on the count mean diameter of SnO_2 particles synthesized in the low-pressure flame reactor

A progressive increase of the *CMD* values were observed for increasing *HABs*. A 100 % increase of the *CMD* from 3.1 nm to 7 nm was observed for *HAB* changes from 100 mm to 190 mm. This phenomenon has been reported in detail by previous investigations on the synthesis of several metal oxide nanoparticles using this low-pressure reactor [12,27,79]. The increasing *CMD* has been attributed to longer time for coagulation and coalescence in the synthesis chamber, due to high concentration of particles suspended in the aerosol medium. The standard geometric deviation σ_g from the particle size distribution was also observed to increase with increasing *HAB*, whereby a maximum of $\sigma_g = 1.283$ was measured at *HAB* = 190 mm (see Figure 4.5). This result can be attributed to the temperature-residence time history of the particle in the synthesis chamber. Due to the temperature differences in the axial and radial directions of the reactor, coagulation and coalescence rates that are temperature and time dependent are strongly influenced. Hence as time and temperature decreases along the direction of flow, incomplete coalescence of particles results in loose particles, agglomerates and aggregates. The influence of *HAB* on the geometric standard deviation of the synthesized MO_x nanoparticles is presented in Figure 4.5.

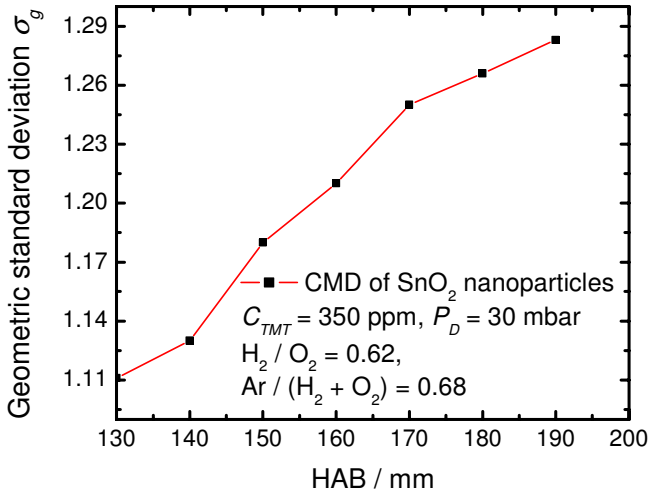

Figure 4.5: Change in the geometric standard deviation of SnO_2 nanoparticles with respect to the height above burner *HAB*

The σ_g was observed to increase with rising *HAB*. This can be attributed to the higher number of agglomerates and aggregates formed as a result of incomplete coalescence

influenced by the temperature-time history of the process. Hence at higher *HABs* the particle size distribution becomes more polydispersed.

The influence of precursor concentration on the *CMD* of SnO_2 particles was investigated by varying the flow rate of dilute concentrations of *TMT* into the reactor. In order to maintain the total volumetric flow rate, the difference from varying the precursor flow rate was compensated by adjusting the argon flow rate. In Figure 4.6, the change of the *CMD* is presented as a function of the precursor concentration and the height above burner (*HAB*). A progressive increase of the *CMD* with rising *TMT* concentration is observed due to more frequent coagulation and coalescence as a result of elevated specie concentration. The *CMDs* for all precursor concentration investigated, established a direct relationship with increasing *HAB* values. Hence for elevated *HAB* values, the *CMDs* show a corresponding increase due to increased characteristic times for coagulation and coalescence. However, at higher *HABs* (downstream of the flame), the combustion chamber temperature is relatively lower, hence, the coagulation and coalescence processes often results in a mix of single particles, agglomerates and aggregates.

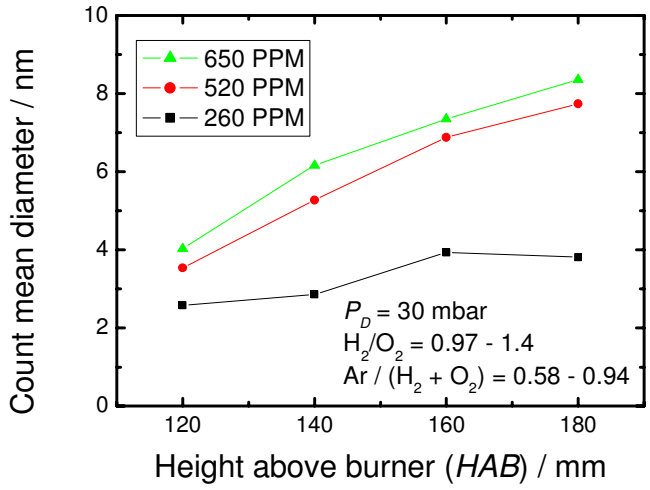

Figure 4.6: Change in the count mean diameter of SnO_2 nanoparticles with respect to precursor (*TMT*) concentration and height above burner (*HAB*) in the low-pressure flame reactor

4.1.2.2 **X-ray diffraction (*XRD*)**

The as-synthesized particles were analyzed with an X-ray diffractometer (Pan analytic X'pert), so as to confirm the synthesized metal oxide, and obtain information on its crystallinity. From Figure 4.7, the Bragg reflections on the diffractogram were matched to the tetragonal rutile structure of SnO_2. It is the most stable phase that occurs at high temperatures, hence, the temperature and residence time available during synthesis were sufficient for the creation of the most stable crystal structure of this metal oxide. Lattice parameters reported for SnO_2 are presented in Table 7.3 in Appendix A.

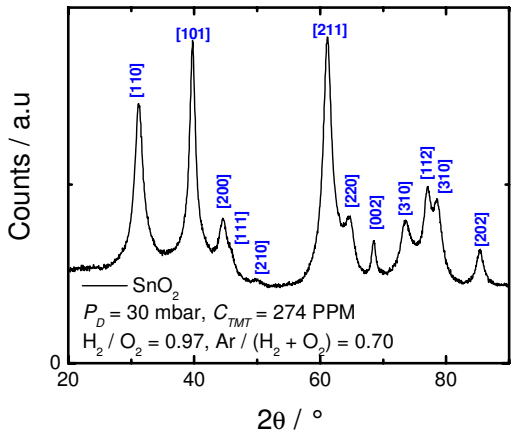

Figure 4.7: X-ray diffractogram of SnO_2 nanoparticles synthesized in the low-pressure flame reactor

The tetragonal crystal structure of SnO_2 (Figure 4.8) has a space group D4h [P42/mm][Jar76], whereby each unit cell of the crystal structure contains 4 oxygen and 2 tin atoms (see Figure 4.8).

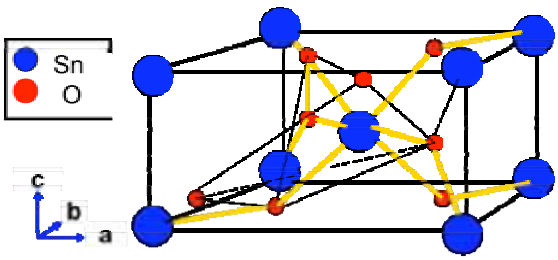

Figure 4.8: schematic of the tetragonal (rutile) crystal structure of flame synthesized SnO_2 nanoparticles

Each tin atom is octahedrally coordinated from six oxygen atoms. Three tin atoms located approximately at the corners of an equilateral triangle surround every oxygen atom, whereby, this arrangement is referred to as the 6:3 coordination [5].

The lattice parameters calculated from the *XRD* diffractogram (Figure 4.7) are $a = b = 0.472$ nm and $c = 0.3155$ nm, which are slightly lower than $a = b = 0.4737$ nm and $c = 0.3185$ nm reported in literature for bulk SnO_2 [5]. The difference can be attributed to size-effects such as Hall-Petch, reverse Hall-Petch, and surface stress, associated with the scale down of bulk materials to the nanosize regime. Furthermore, the crystallite size of the flame synthesized SnO_2 particles was calculated from the diffractogram (Figure 4.7) with the *Scherrer* equation, and the full width at half maximum (FWHM), from a *Lorentz* fit of a Bragg reflex. A crystallite size $d_{pcrystallite} = 4.1$ nm was calculated, which is within the size range of *CMDs* obtained from the *PMS* analysis.

4.1.2.3 **Transmission electron microscope (TEM)**

TEM analysis of the SnO_2 particles was performed with a *CM 12* transmission electron microscope. The SnO_2 particles were sampled on the *TEM* grids using two different methods. In the first method the *TEM* grid was placed on a pneumatic assisted particle sampling device that uses compressed air to quickly insert and withdraw the *TEM* grid to a position, directly in front of the sampling orifice, downstream of the flame (see Figure 3.5) in the reactor. Particles sampled at this position are assumed to be stable (no significant changes with respect to size and morphology), due to their proximity to the sampling orifice. Particles that go through the sampling orifice are instantaneously "frozen" due to the supersonic expansion into the free molecular. Even though the pneumatically assisted *TEM* sampling method is relatively fast (few milliseconds), and can be operated without stopping the experiment, particles sampled on *TEM* grids often exhibit some degrees of soft agglomeration due to thermophoretic deposition.

The second method involves sampling the particles from the molecular beam, which arises after subsequent expansion of the aerosol from low-pressure to vacuum conditions. This method referred to as molecular beam-assisted-particle-deposition (*MBAPD*), can be used to deposit particles laden in the molecular beam on surfaces and structures, as well as to perform PMS analysis. The advantage of this method is the deposition of highly dispersed particles with low degree of agglomeration on *TEM* micrographs. This method is however constrained by blockage of the sampling

orifice during experiment, especially when high precursor concentrations are involved. Furthermore, due to the high dilution of the aerosol during expansion, deposition of particles on substrates usually requires a few hours before a monolayer on a spot diameter of 3 mm is achieved.

The *TEM* micrograph seen on Figure 4.9 shows flame synthesized SnO_2 nanoparticles sampled from the molecular beam. The particles have very poor contrast, which is typical for oxide materials due to their high oxygen content. However, the particles morphology is identifiable and observed to be spherical. The insert *A* shows an overview image of the micrograph, whereby, the particles appear to be slightly agglomerated with both hard and soft agglomerates. The insert *B* shows a diffraction image of the SnO_2 particles. The bright rings indicate the relatively good crystallinity of the material, which is further confirmed by the presence of lattice fringes seen as ordered parallel lines on the surface of the particles (Figure 4.9).

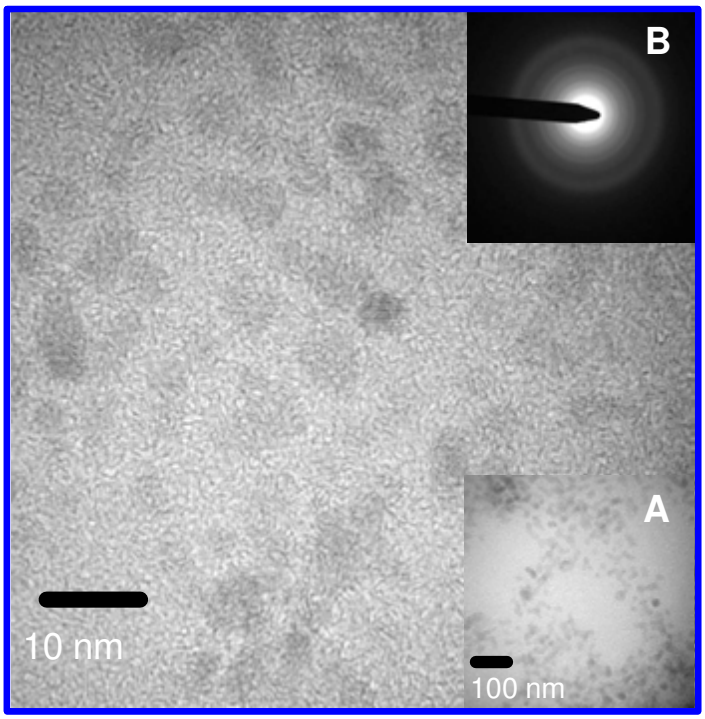

Figure 4.9: *TEM* micrographs and diffraction image of flame synthesized SnO_2 nanoparticles sampled with pneumatically assisted *TEM* sampling device

The diameters of the particle are below 10 nm, which further validates the result obtained from the *PMS* analysis. In order to compare the result from *PMS* with *TEM* image analysis, several hundred particles sampled on the *TEM* micrograph were characterized with the software *Imagetool*™. The measured particle diameters were

subsequently classified with frequencies and a histogram of the particle size distribution was generated. The histogram was fitted with a normal distribution and compared to the *PMS* result. During this experiment, the height above burner *HAB* was kept constant at 90 mm, reactor pressure was 30 mbar, precursor concentration was kept at 274 ppm and hydrogen/oxygen ratio was set at 0.97. The result of the comparative analysis is presented graphically in

Figure 4.10. From the results, both particle size analysis methods (TEM analysis and PMS) are in good agreement, whereby, slight differences in the mean particle diameter and the geometric standard deviation exist. This disparity can be attributed to the errors involved with both measurement methods however the differences are accepted to be within error limits [80].

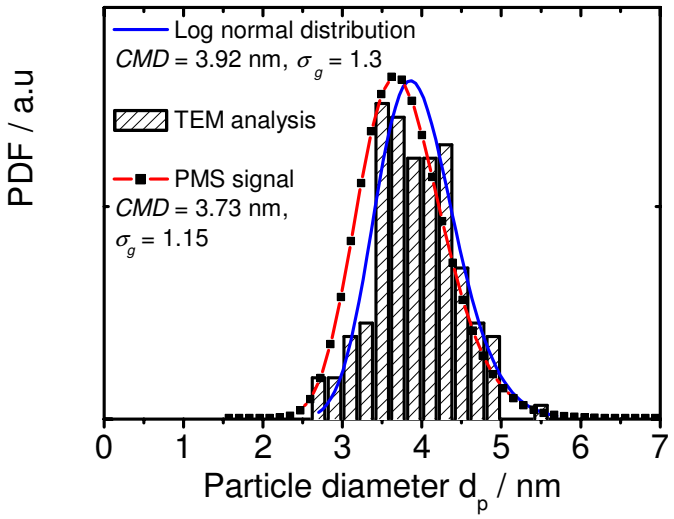

Figure 4.10: Comparative analysis of PMS generated mean particle diameter and TEM image analysis generated mean particle diameter.

4.1.2.4 **UV-spectroscopy**

SnO_2 by virtue of its band gap and composition is classified as a transparent conducting oxide, therefore, investigation of its optical property was performed using a *UV-Vis* spectrophotometer. The powder sample was placed in a small sample holder in the spectrophotometer and exposed to a light beam with a scanning wavelength from 700 - 200 nm. The reflectance of the material with respect to the incident light wavelength is shown in Figure 4.11*a*. From the reflectance spectrum, it was observed that the as-synthesized SnO_2 particles show its maximum reflectance in the visible range (from

400 nm Figure 4.11), however, in the UV range, the reflectance progressively decreases, which indicates strong absorption in this range. In order to ascertain the absorption properties, as well as the band gap of this material, the *Kubelka-Munk* function, *F(R)* that allows the optical absorbance of sample to be approximated from its reflectance is employed. The function is expressed as:

$$F(R) = \frac{(1-R)^2}{2R} \qquad 4.2$$

From this expression, semi-conducting materials can be analyzed with a *Tauc plot* [81], whereby $(F(R)\cdot h\nu)^n$ against $h\nu$ is plotted and n = 0.5 (direct band gap) and 2 (indirect band gap material). On the T*auc plot*, a linear region just above the optical absorption edge is fitted and extrapolated to the photon energy axis as illustrated in Figure 4.11B. The intercept on this axis represents the band gap of the material under investigation.

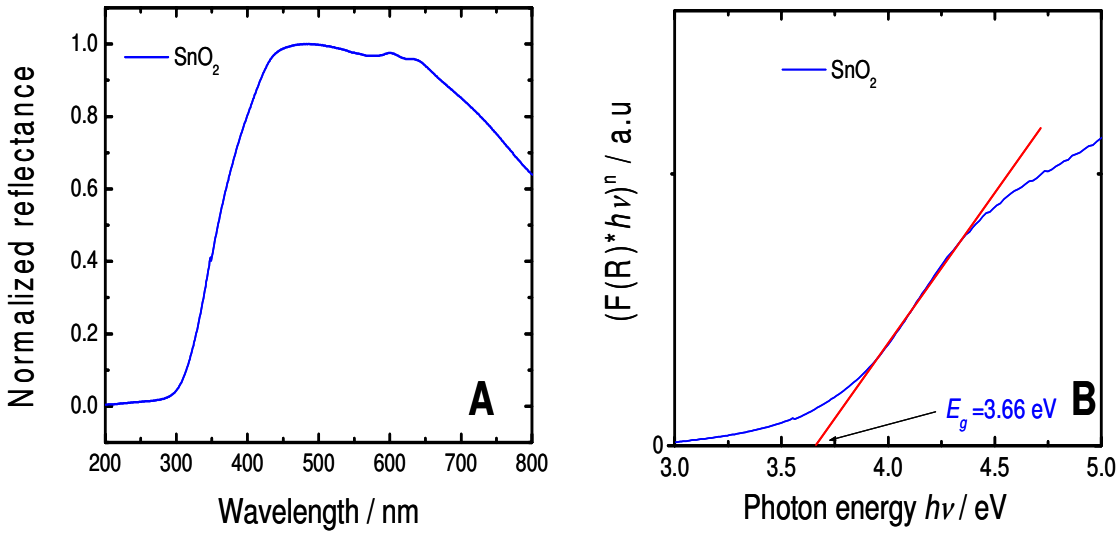

Figure 4.11. A) Reflectance spectrum of SnO_2 with respect to wavelength light beam; B) *Tauc plot* of SnO_2 nanoparticles indicating optical band gap of the material

From the *tauch plot* analysis, a band gap of 3.66 eV was obtained for the flame synthesized SnO_2 nanoparticles. This value slightly differs from the literature reported value of 3.6 eV by about 60 meV [82]. The difference can be attributed to blue-shift due to quantum size effects, and is accepted to be within tolerable limits. The band gap of a material is a key indicator of its efficiency to harvest light upon exposure.

4.1.3 **Tuning the stoichiometry of tin oxide (SnO_x for $1.4 \leq x \leq 1.8$)**

Tin is known to exhibit stable oxidation states of 2 and 4, however oxidation states that lie between those values have also been identified [83]. Such sub-oxides are of huge interest due to increased charge carrier concentration, as a result of deficiencies created by the absence of oxygen atoms from the crystal structure. Several experiments have been designed and performed to investigate the conditions necessary for the formation of these sub-oxides as well as the degree of sub-stoichiometry exhibited by these materials. These experiments are similar to those performed for SnO_2 synthesis, however, the H_2/O_2 ratios were progressively increased with the objective that the stoichiometry of the synthesized metal oxide will be "tuned" correspondingly. The sub-stoichiometry of the synthesized metal oxides were analyzed with Auger electron spectroscopy (*AES*) that gives information about the stoichiometry of materials up to a depth of about 3 nm. Finally the materials were characterized and their properties compared to fully oxidized SnO_2.

During the SnO_2 synthesis experiment, a H_2/O_2 ratio of about 1 was used that ensured excess O_2 with respect to stoichiometric values required for complete combustion of H_2. Stoichiometrically, a H_2/O_2 ratio of 2 should be adequate for the complete combustion of H_2, however, this value was adjusted to 1.97 to accommodate the oxygen requirement for the precursor. The reactor pressure was maintained at 30 mbar, the inlet gas velocity was 1.32 m/s, and the precursor concentration was set at 500 ppm.

The H_2/O_2 ratio of 1,97 should be sufficient to yield fully-oxidized SnO_2 nanoparticles, however, a thin gray coloured film was observed on the walls of the reactor, which could not be recovered for *ex-situ* analysis. SnO particles are gray coloured and have low evaporation enthalpy. The absence of macroscopic quantities of this monoxide in the reactor can be attributed to the relatively high temperature downstream of the flame (see Figure 4.1) that hinders condensation of large quantities of supersaturated SnO vapour in the reactor. Hence, entrainment of the vapour through the pumping system occurs and "good" *PMS* signals could not be obtained due to low particle concentration. It is then concluded that the H_2/O_2 ratio of 1.97 did not provide sufficient oxygen for the generation of SnO_2 nanoparticles, rather a lower oxide (SnO) present in the reactor as a thin film was observed.

For the next set of experiments, the H_2/O_2 ratio was further reduced by increasing the oxygen concentration. The selected H_2/O_2 volumetric ratios were 1.7, 1.4 and 1.27. Pressure and inlet velocity were maintained from the initial experiment, while the precursor concentration was varied between 500 and 1000 ppm.

Unlike in the initial experiment, light yellow to off-white coloured powders were obtained from all the experiments, which indicates some differences between the particles. The stoichiometries of these particles were characterized by Auger electron spectroscopy (*AES*) as shown in Figure 4.12. The relative intensities of the Sn and O Auger peaks from the flame synthesized materials were compared to that of standard, commercial SnO_2, initially measured. The result of this comparison establishes the degree of sub-stoichiometry of the flame synthesized materials. The *AES* result of the flame generated particles indicates that SnO_x nanoparticles, with stoichiometries corresponding to $1.4 \leq x \leq 1.8$ were obtained (Figure 4.12). This implies that despite the excess oxygen in the flame, the particles were not completely oxidized. Furthermore, some degree of carbon contamination on the SnO_x particles was observed from the *AES* result, which was attributed to the carbon content of the metalorganic precursor. This result indicates that stoichiometric O_2 concentrations are insufficient for synthesis of fully oxidized tin oxide particles with respect to this synthesis route, and reactor geometry.

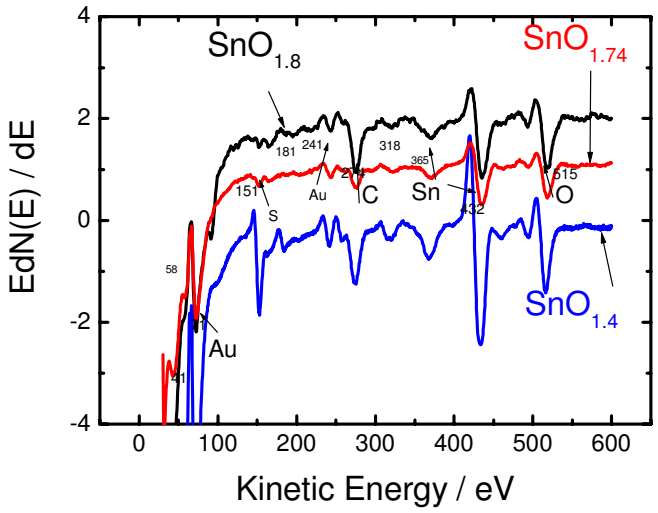

Figure 4.12: Auger electron spectroscopy of SnO_x nanoparticles "tuned" in the low-pressure flame reactor

Based on the result obtained from previous investigations, the volumetric H_2/O_2 ratio was set at 0.97, which corresponds to a significant excess of O_2. The pressure and inlet gas velocities were maintained as in the previous experiments, while the precursor concentration was varied between 200 and 700 ppm.

White nanoparticles corresponding to SnO_2 were obtained from this investigation, which was confirmed by *AES*. The quantity of SnO_2 nanoparticles obtained was significantly higher than that obtained for each of the previous SnO_x experiments. The results from these investigations show that stoichiomteric H_2/O_2 ratios are inadequate for the synthesis of fully oxidized materials. This phenomenon can be partially attributed to $OH^{\bullet}$ distribution within the system as well as flame chemistry involving dilute concentrations of metalorganic precursors. $OH^{\bullet}$ is assumed to be responsible for the oxidation of species released during thermal dissociation of the metal organic precursor. However, 1-dimension simulation of its concentration in the reactor was investigated with *CHEMKIN's PREMIX*™ and presented in Figure 4.13 [84].

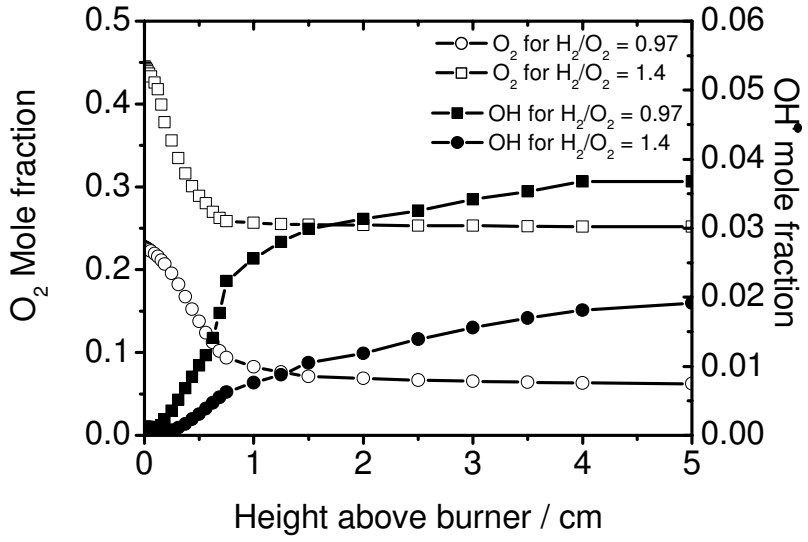

Figure 4.13: *PREMIX*™ simulation of O_2 and $OH^{\bullet}$ concentrations above burner matrix for $H_2/0_2$ ratios of 1.4 and 0.97

The simulation indicates that the O_2 concentration is depleted at about 2 cm height above burner, while a progressive increase in $OH^{\bullet}$ concentration is observed accordingly. The $OH^{\bullet}$ concentration is vital for the "high speed" oxidation process and its concentration with respect to height above burner is indicative of the degree of

oxidation at the position. Hence, the oxidation process is assumed to be complete at 5 cm height above burner due to no further increase of the $OH^{\bullet}$ concentration.

Tin oxide stoichiometries are displayed as a function of the H_2/O_2 ratio in Figure 4.14 whereby the stoichiometries have been determined by Auger electron spectroscopy (*AES*).

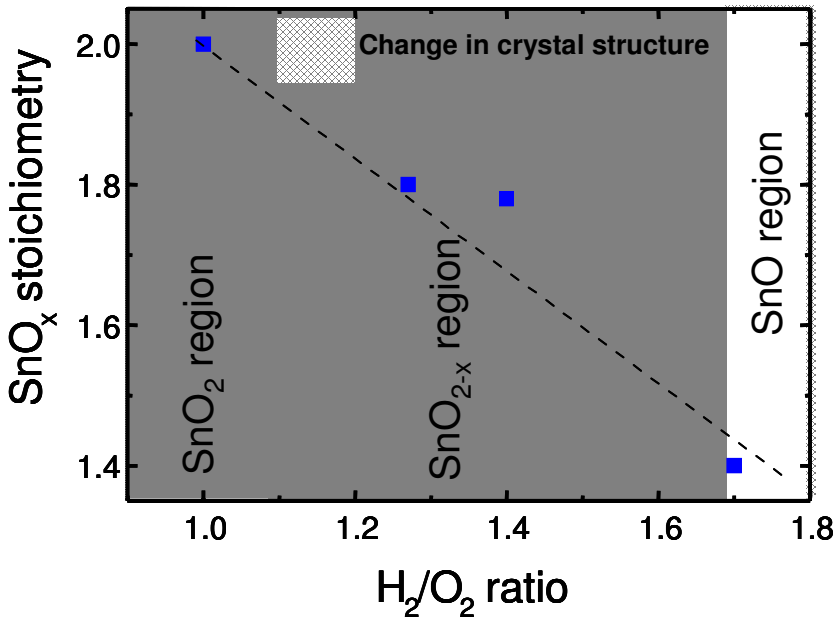

Figure 4.14: Tin-oxide stoichiometries with respect to H_2/O_2 ratios in the low-pressure premixed flame reactor

From the illustration in Figure 4.14, the SnO and SnO_2 regions are relatively small in comparison to that of SnO_x. Furthermore, a linear relationship exists between the H_2/O_2 ratio and the resulting tin-oxide stoichiometry [23,80]. This confirms that the tin-oxide stoichiometry can be effectively "tuned" during flame synthesis by varying the H_2/O_2 ratios.

The physical properties of the SnO_x nanoparticles were further characterized with the *PMS*, *XRD* and *UV-spectroscopy* and the results compared to those for SnO_2 nanoparticles. The trend of the mean particle diameter with respect to *HAB* for SnO_x nanoparticles is similar to that for SnO_2 nanoparticles (Figure 4.15). The increase in mean particle diameter was observed to be directly proportional to *HAB*, as was similarly seen for SnO_2 nanoparticles.

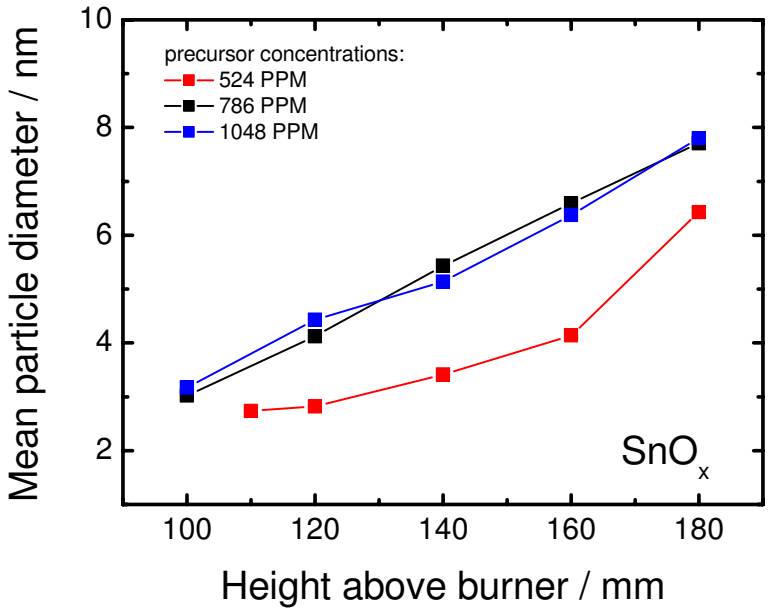

Figure 4.15: Influence of *HAB* on the count mean diameter of SnO_x particles synthesized in the low-pressure flame reactor

XRD analyses were performed on almost all the tin oxides to investigate any significant differences that might be as a result of the various stoichiometries. Commercial SnO is known to have a different crystal structure in comparison to SnO_2. However, the crystal structure of flame synthesized SnO could not be analyzed, due to lack of macroscopic quantities for this investigation.

The *XRD* of $SnO_{1.74}$ particles showed no significant difference in comparison to SnO_2 as seen in Figure 4.16, hence, the crystal structure of $SnO_{1.74}$ can be assumed to be almost identical with that of SnO_2 particles. It is expected that $SnO_{1.74}$ particles that has some oxygen deficiency in the crystal lattice will exhibit some major differences in comparison to SnO_2 particles when analyzed by *XRD*. This is because loss of oxygen in the crystal lattice should lead to the re-adjustment of the lattice, which inherently can influence the crystal structure and the lattice parameters. However, the absence of oxygen atoms in the crystal lattice does not result in a collapse of the crystal structure rather the lattice parameters slightly change towards a structurally stable arrangement in order to annul the effect of the oxygen deficiency in its crystal lattice. This theory has not been experimentally proven, however, preliminary results from on going *ab-initio*

simulation into oxygen deficiency in the SnO_2 crystal lattice seems to support this statement.

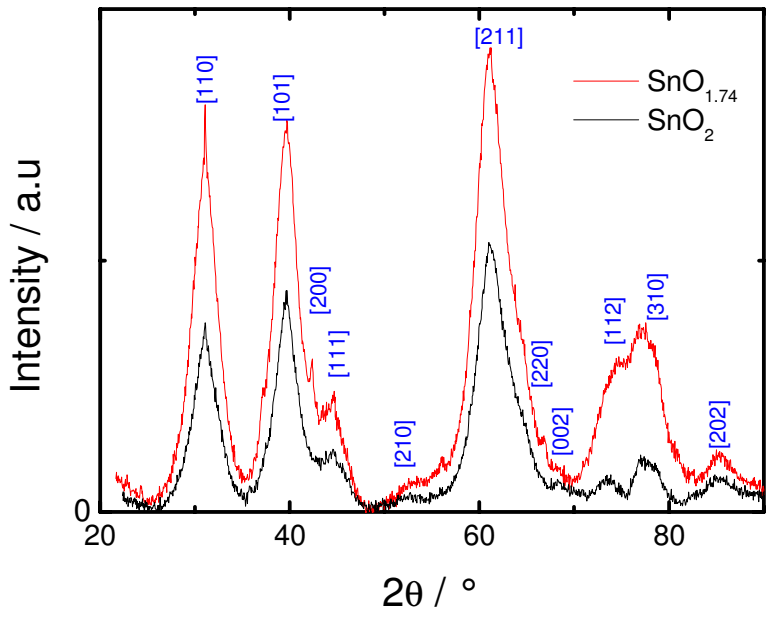

Figure 4.16: X-ray diffractogram of $SnO_{1.74}$ and SnO_2 nanoparticles synthesized in the low-pressure flame reactor

In order to understand the formation of Sn-atoms from the precursor tetramethyl tin (TMT) and its subsequent oxidation by O_2, some high temperature shock tube experiments have been performed [85]. A shock tube is a high temperature wave reactor, in which gas mixtures can be instantaneously heated up to constant high temperatures for about 1 to 2 µs. Thermal dissociation reactions initiated in that way can be followed by spectroscopic methods and evaluated in terms of rate coefficients.

The thermal dissociation of the Sn-precursor (*TMT*) and the subsequent oxidation by O_2 was studied in mixtures of *TMT*/O_2, diluted in Ar at temperatures 1025 K $\leq T \leq$ 1390 K and a pressure of about 1.6 bar [86]. A typical experimental result is shown in Figure 4.17. The time $t = 0$ characterizes the arrival of the shockwave and the associated sudden temperature increase. The precursor decomposes forming Sn-atoms during the first 300 µs, thereafter, the Sn-concentration decreases due to oxidation by O_2. The computer simulation (red line) is able to verify the experimental finding, but the oxidation product SnO and SnO_2 could not be recognized.

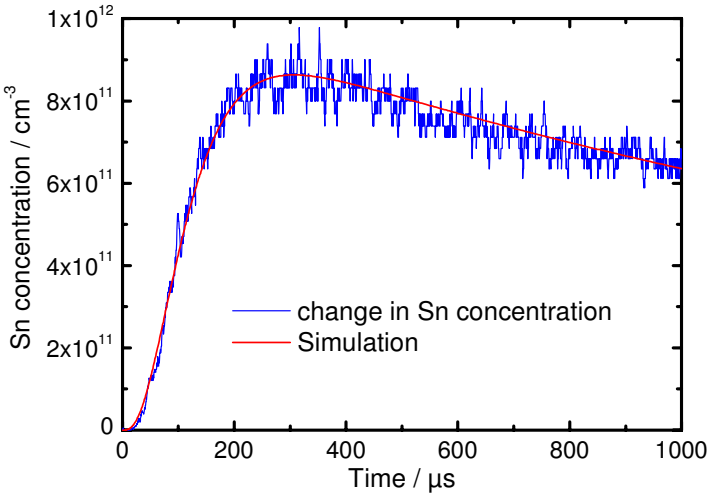

Figure 4.17: Measured Sn-concentration profile showing a rapid formation during *TMT*-dissociation and subsequent consumption due to oxidation by O_2.

Therefore, additional shock tube experiments [85] were performed using SnO-nanoparticles, which were generated in a tube furnace and later dispersed in O_2/Ar gas mixtures. At the high post-shock temperatures, the particles evaporate, which could result in the formation of gas phase SnO. Further oxidation by O_2 was directly measured by detecting the appearance of O atoms from experiments performed in the temperature range 1700 K $\leq T \leq$ 2300 K at pressures around 100 KPa

$$SnO_g + O_2 \rightarrow SnO_{2g} + O \qquad (4.3)$$

A rate coefficient of the above reaction was determined and reported as:

$$K = 10^{14.78} \exp^{(23530\ K/T)}\ cm^3\ mol^{-1}s^{-1}$$

The corresponding Arrhenius diagram is presented in the figure below.

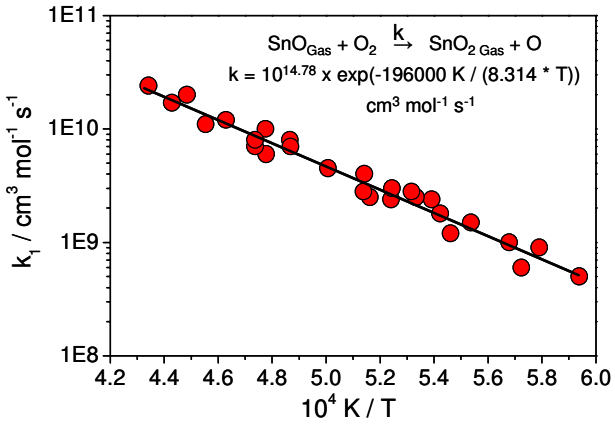

Figure 4.18: Arrhenius diagram of the rate coefficient for the reaction $SnO_g + O_2 \rightarrow SnO_{2g} + O$ determined based on O-atom measurements

4.1.4 **Electrical properties of SnO_2 and SnO_x nanoparticles**

Electrical characterization of the flame synthesized tin oxides was performed with impedance spectroscopy. Tin oxide like many transparent conducting metal oxides, has the potential to change its conductivity when exposed to different gases (oxidizing and reducing). The possibility of characterizing the behaviour of tin oxides with respect to changes in their conductivity can potentially be applied to gas-sensing devices.

The SnO_x nanoparticles were deposited on an inter-digital capacitor (*IDC*) using the molecular-beam-assisted-particle-deposition method (*MBAPD*). The *IDC* shown in Figure 4.19A, was positioned in the analysis chamber of the low-pressure reactor, with a specially constructed holder. Positioning the *IDC* device correctly in the reactor is of utmost importance, due to the relatively small dimension of the device, as well as small contact area of the molecular beam.

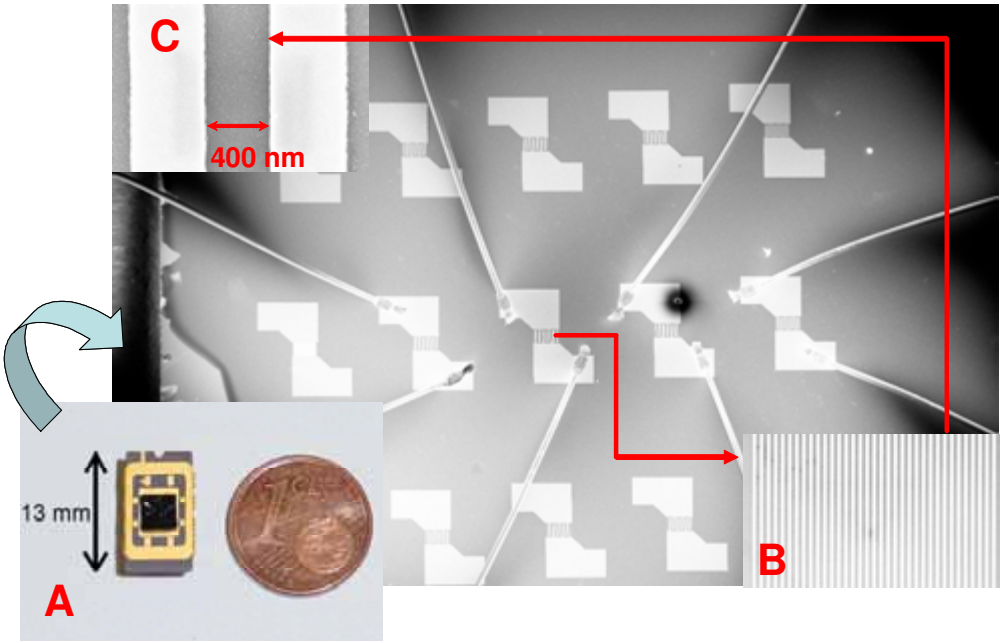

Figure 4.19: Photo and *SEM* image of various magnifications of an inter-digital capacitor structure (*IDC*) for impedance spectroscopic analysis of nanoparticles

Consequently, tin oxide particles in the molecular beam were separately deposited on the structure that consists of gold fingers with a distance of 200 nm and width of 400 nm. These fingers have a parallel arrangement and cover an area of 50 µm by 100 µm as shown by the magnifications in Figure 4.19*b* and *c*. The fingers are contacted, and the entire device was placed in a separate set-up after particle deposition for *IS* measurements.

A *Nyquist plot* (Figure 4.20) generated from the *IS* measurement shows the resistance distributions of SnO, $SnO_{1.74}$ and SnO_2 nanoparticles. The commercial SnO material was pressed into a small disk and *IS* analysis performed using another set-up that was previously described elsewhere [87]. It must be stated that the influence of the sample preparation method, which differs for SnO and $SnO_{x\ (1<x\leq 2)}$ is considered as non-consequential on the result presented in Figure 4.20.

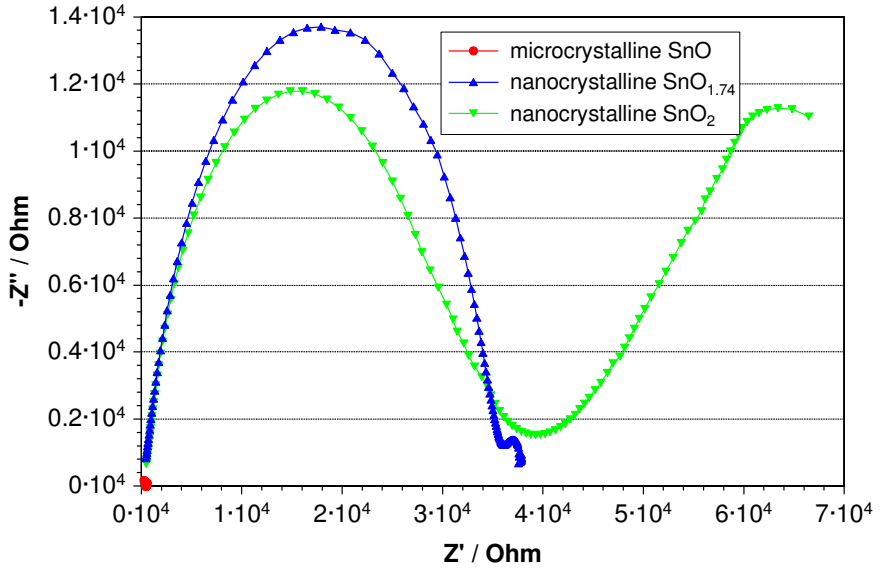

Figure 4.20: *Nyquist plot* of commercial SnO, $SnO_{1.74}$ and SnO_2 nanoparticles showing resistance contributions of these materials for both high frequency (HF) and low frequency (LF) measurements

The *Nyquist plot* indicates the resistivity of the tin oxides measured by impedance spectroscopy. The z'-axis represents the real part of the impedance analysis while the z''-axis represents the imaginary part. From Figure 4.20, it was observed that SnO exhibits the smallest resistance in comparison to $SnO_{1.74}$ and SnO_2. Hence it can be concluded that the conductivity of SnO (see red point on Figure 4.20) is significantly higher than that of $SnO_{1.74}$ and SnO_2. In the same context, $SnO_{1.74}$ and SnO_2 nanoparticles reveal two contributions to the overall impedance, whereby, $SnO_{1.74}$ shows a smaller resistance in the low frequency (LF) range. These contributions originate from bulk and grain boundary conduction processes that can be separated with AC methods. However, these results confirm the enhancement of conductivities with decreasing oxygen content, which arises from oxygen atom deficiencies in the crystal lattice of the material.

Based on this observation, detailed impedance measurements of SnO_x were performed in synthetic air in the temperature range from 343 to 503 K, for increasing and decreasing temperatures. Figure 4.21 shows the *Nyquist* diagram of two measurements at 433 K, the first during the heating process and the subsequent cooling process. For both measurements, the results show semi-circles as expected for semi-conducting materials. The second measurement (cooling) showed enhanced conductivity.

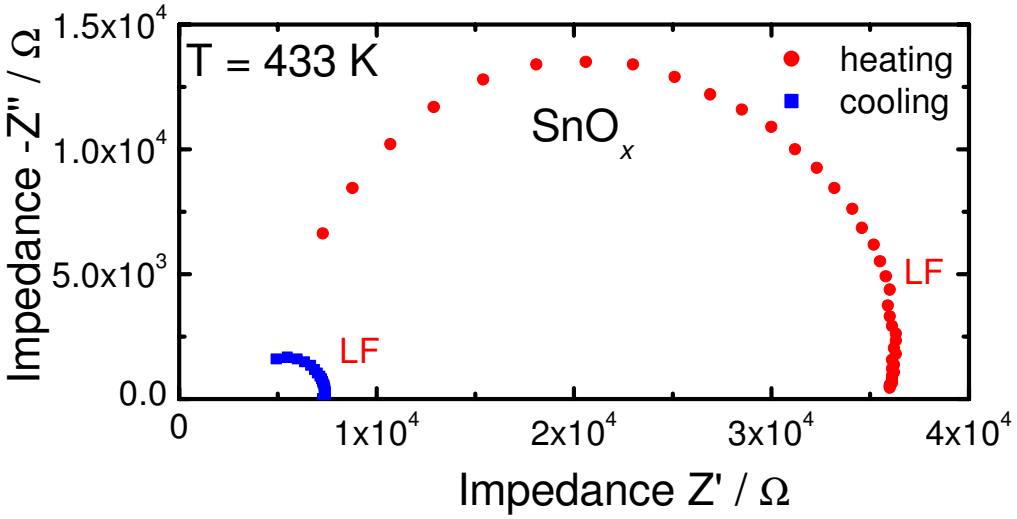

Figure 4.21: Nyquist plot of SnO_x nanoparticles measured during heating and cooling of the sample material

Based on the low frequency conductivity values, the temperature dependence was analysed by means of an Arrhenius diagram (Figure 4.22). The activation energy of the charge carrier transport process represented by the heating process can be extracted from the slope of the low temperature range and has been calculated to be 302 meV [80]. The overall conductivity is however relatively better due to a sintering process that improves the grain boundary contacts.

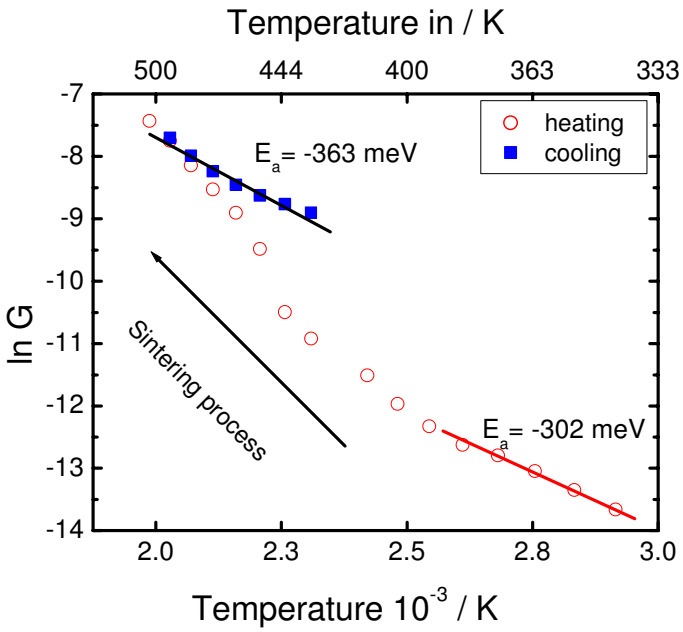

Figure 4.22: Arrhenius diagram obtained from analysis of the Bode plot of SnO_x nanoparticles for both heating and cooling of the sample material

The difference in conductivity between heating and cooling can be attributed to physical changes of the material. Starting from 400 K, the conductivity increases some orders of magnitude and remains significantly high when the sample is cooled down. This behaviour is well known for nano-particulate materials and can be attributed to sintering processes without growth. However, the activation energy for the charge carrier transport process after sintering can be extracted and calculated to be -363 meV. Furthermore the sintering process resulted in no significant growth rather better contact between the particles were observed from the scanning electron microscope (*SEM*) images.

From the result of the electrical investigation of SnO_x particles, the temperature dependent semi-conducting behaviour of this material was confirmed. The semi-conducting behaviour of tin oxide has been reported to be influenced by the particle size [83], hence particle size control is essential for obtaining tailored materials.

4.2 Titanium dioxide nanoparticles (TiO_2)

Titania (TiO_2) is the most widely researched metal oxide in the world and has been in commercial production for over 60 years. However, research into its synthesis, functionalization, characterization, and commercialization continues with huge interest [2,11]. The interest in titania stems from its unique properties, which have been applied to pigments, UV-protection creams, and more recently in photocatalysis as well as solar cells. The mean particle size, crystallinity, and morphology are some of the properties that determine its suitability for various applications previously enumerated. The objective of this study was to investigate the conditions necessary for the synthesis of nanosized titania in the low-pressure premixed flame reactor, as well as characterize its properties. Finally the photocatalytic efficiency of the flame synthesized titania was investigated and compared with commercial titania P25 from Degussa.

4.2.1 Synthesis of TiO_2 nanoparticles

The synthesis of TiO_2 nanoparticles was performed in the low-pressure reactor by doping the premixed $H_2/O_2/Ar$ flame with dilute concentrations of titanium tetra isopropoxide (*TTIP*). This precursor has very low vapour pressure at room temperature (< 0.1 mbar at 25°C), hence, it cannot be diluted in the mixing vessel (section 3.1.1) like other precursors previously described (see precursor properties in Table 7.4 of Appendix A). Dilute concentrations of *TTIP* was achieved using either the controlled evaporation and mixing device (*CEM*) or the pressure controlled mixing device both described in section 3.1.2 and 3.1.3, respectively. The experimental parameters for TiO_2 synthesis in the low-pressure flame reactor are as follows:

Precursor mass flow (*TTIP*)	0.5 – 1.5 g/h
Reactor pressure P_D	30 mbar
H_2 / O_2 ratio	0.67 – 2.0
Inlet gas velocity v_u	1.32 m/s
Height above burner *HAB*	80 – 180 mm

The synthesis of TiO_2 particles from *TTIP* is described by a simple overall reaction given as follows:

$$Ti(OC_3H_7)_4 + 7O_2 \rightarrow TiO_2 + CO_{2(g)} + 14H_2O_{(g)} \qquad 4.4$$

From the experiment, white crystalline TiO_2 nanoparticles were generated for $H_2/O_2 \leq 0.85$. For this synthesis, the oxygen concentration was slightly reduced than is typically required, due to the presence of oxygen in the precursor. However, further reduction of the oxygen concentration ($H_2/O_2 \geq 1.5$) results in the formation of non-stoichiometric TiO_x powders that exhibit different colours (blue, grey etc.) other than white. The physical properties of bulk TiO_2 are reported in Table 7.5 of Appendix A.

4.2.2 **Characterization of flame synthesized TiO_2 nanoparticles**

The *PMS* was used to analyze the particle size distribution of the TiO_2 nanoparticles while varying the precursor flow rate and the height above burner *HAB*. These two parameters have been identified from previous investigations as the most important factors, which influence the mean particle diameter of materials synthesized in the low-pressure flame reactor. The *PMS* signal and the velocity measurement required for determining the particle size distribution are presented in Figure 4.23.

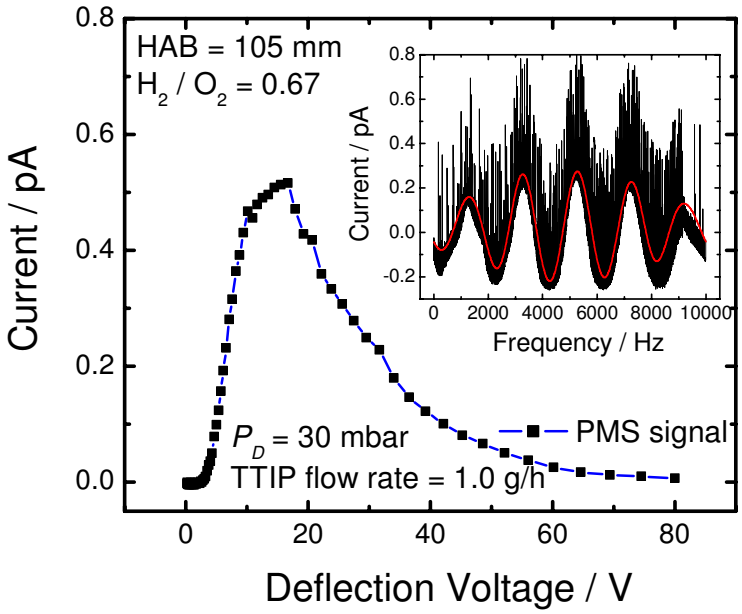

Figure 4.23: *PMS* signal of TiO_2 nanoparticles synthesized in the low-pressure reactor; the insert shows the velocity measurement of the material.

The particle velocity calculated from Figure 4.23 insert was equal to 500 m/s. From this result, a count mean diameter at *CMD* = 6.07 nm and geometric standard deviation σ_g = 1.19 were obtained [88]. Consequently, the change of the mean particle diameter of TiO_2 particles with respect to *HAB* was investigated and the result presented in Figure 4.24.

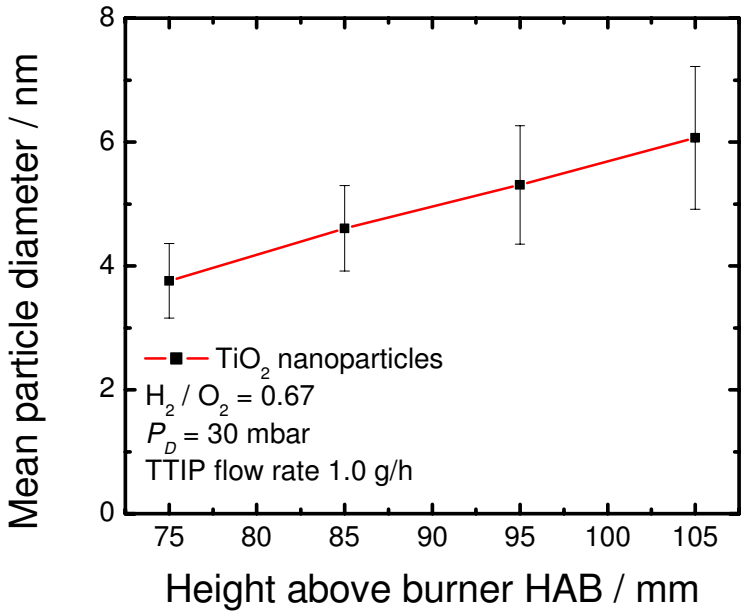

Figure 4.24: Influence of *HAB* on the count mean diameter of TiO_2 particles (Error bars represent the deviation from the mean particle diameter at each *HAB*)

The mean particle diameter was observed to increase correspondingly with the *HAB* for TiO_2 nanoparticles due to increased coagulation and coalescence. However, the rate of change of the mean particle diameter was observed to occur relatively fast, whereby, particle detection began at relatively low *HAB* values. This indicates that the nucleation and particle growth process occur relatively fast for this material. Consequently low geometric standard deviations were observed at low *HAB* values, which progressively increased, as the *HAB* increased. Overall a 2 nm change in the mean particle diameter and 4 % change in the standard geometric deviation were observed over a distance of 30 mm.

The influence of *TTIP* flow rate on the mean particle diameter of TiO_2 nanoparticles was investigated by varying the flow rate at 0.25 g/h intervals starting from 0.5 g/h to 1.5 g/h. The *TTIP* flow rate is directly proportional to the concentration

of *TTIP* in the reactor, and has a direct influence on the mean particle diameter of the material (Figure 4.25). The increase in the mean particle diameter was attributed to the increased coagulation due to higher number of species available as *TTIP* flow rate increases. A change of about 2 nm was observed for a change in the *TTIP* flow rate from 0.5 to 1.5 g/h. The 2 nm change might appear insignificant, however for particles with mean particle diameter below 10 nm, this change is significant and represents over 20% change in this property. It was also observed that the particle size approaches a maximum for high *TTIP* flow rates. This saturation was attributed to the constant *HAB* selected for this investigation. The *HAB* is proportional to the residence time for particle growth, hence, for increasing precursor flow rate, more frequent coagulation, coalescence and particle growth occurs. Therefore, if the maximum residence time available is reached, while precursor flow rate is increasing, there will be insufficient time for particle growth, hence the *PMS* result indicates the onset of saturation in the profile.

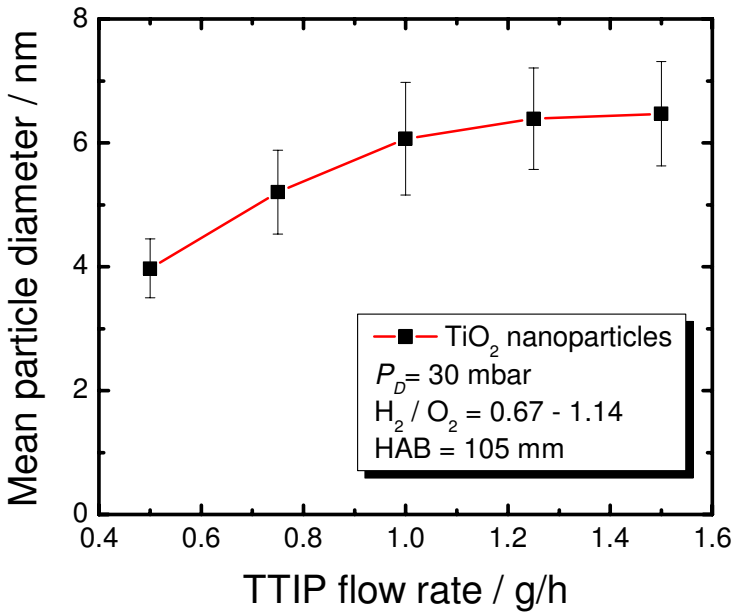

Figure 4.25: The influence of TTIP flow rate on the mean particle diameter of TiO_2 nanoparticles

The mechanism for the synthesis of TiO_2 from *TTIP* follows the thermal dissociation mode. This model is typical for many metalorganic precursors and has been described in detail by *Pratsinis et al.* [89] for TiO_2 synthesis from $TiCl_4$.

The TiO2 nanoparticles synthesized under different H_2/O_2 ratio were analyzed with *XRD*. The result of the investigation is presented in the diffractogram shown in Figure 4.26. From the diffractogram, a sharp Bragg reflection at $2\theta = 33.10$ was observed, and can be attributed to the silicon substrate on which the TiO_2 nanoparticles were deposited. Two different H_2/O_2 ratios (0.67 and 1.0) were selected so as to investigate the influence of temperature on the material, whereby, the oxygen concentration was set so that synthesis of completely oxidized TiO_2 nanoparticles will be achieved.

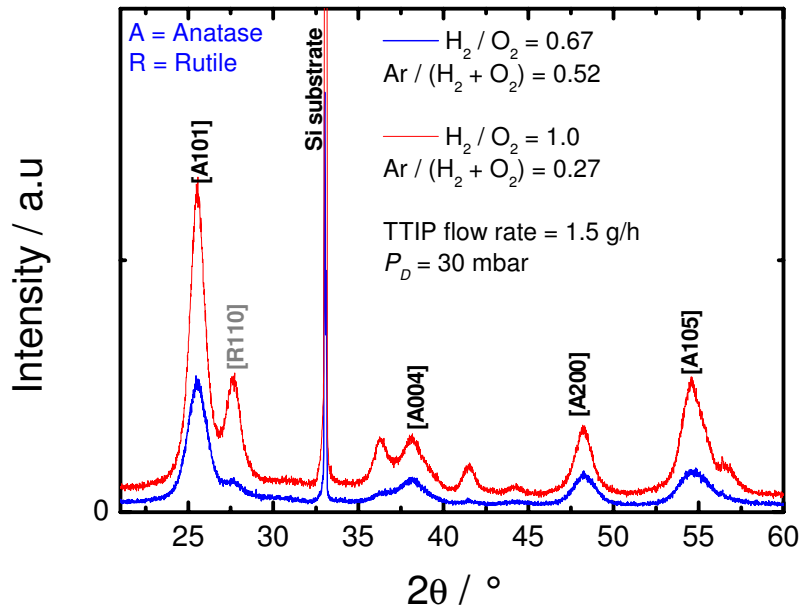

Figure 4.26: *XRD* of TiO_2 nanoparticles synthesized under different H_2/O_2 ratios in the low-pressure flame reactor

From the diffractogram, both powders show dominant anatase structure with traces of the rutile crystal structure. However, the particles synthesized at $H_2/O_2 = 1$ show significant rutile Bragg reflections in comparison to the particles synthesized at H_2/O_2 ratio of 0.67. The rutile crystal structure is the most stable structure of titania, which usually evolves at higher temperatures. Hence, it was initially suggested that due to higher H_2 and lower Ar concentrations for $H_2/O_2 = 1.0$ in the premixed flame, the flame temperature was higher than that for the lower H_2 concentration. However, flame temperature measurement from *NO-LIF* analysis for various H_2/O_2 ratios, revealed only a slight difference in the maximum temperature for both H_2/O_2 ratios, but similar

cooling profile downstream of the flame. Hence the rise of the rutile Bragg reflections cannot be attributed directly to the increased flame temperature.

It has been reported that increasing the oxygen concentration during flame synthesis of titania with *TTIP*, improves the formation of the anatase phase [52]. Hence the formations of the anatase and rutile crystal structures are influenced by the relative concentration of the oxidant in the synthesis environment. The common crystal structures and lattice parameters of TiO_2 are presented in Table 7.6 of the Appendix A.

The flame synthesized TiO_2 nanoparticles (mixed anatase and rutile) have a tetragonal structure, similar to the rutile structure of SnO_2, whereby the space groups for rutile and anatase TiO_2 particles are $D_{4H}^{14} - P4_2/mnm$ and $D_{4H}^{19} - 14_1/amd$ respectively. The lattice parameters calculated from the diffractogram were compared to the literature values for anatase and rutile structured TiO_2 particles, and is presented in Table 4.1.

Table 4.1: Lattice parameter values for rutile, anatase and TiO_2 nanoparticles synthesized in the low-pressure reactor

TiO_2	*a* (nm)	*c* (nm)	*c/a*
Rutile [90]	0.4584	0.2953	0.644
Anatase [90]	0.3733	0.937	2.51
Flame synthesized	0.376	0.928	2.46

The calculated lattice parameters for the flame synthesized TiO_2 nanoparticles appear to be similar to literature reported values for the anatase structure. This result further confirms that the flame synthesized titania is not homogenously composed of a single crystal structure, rather it is a hybrid of the dominant anatase and the recessive rutile structures.

TiO_2 nanoparticles synthesized for a very low *TTIP* flow rate of 0.5 g/h were sampled using the previously described *MBAPD* at *HAB* = 60 mm. The micrograph with the sampled TiO_2 nanoparticles is presented in Figure 4.27. It shows that the particles are not highly agglomerated, which is in contrast to previous observations of flame synthesized powders. The insert shows the particle deposition over a wider area (lower magnification), where it is observed that the deposition is homogenous. The relatively

low *TTIP* flow rate, coupled with the molecular beam expansion of the aerosol, as well as short sampling time, resulted in the low agglomeration observed on the micrograph. In practice, particles thermophoretically deposited in the combustion chamber and filter systems of the reactor, always have a high degree of agglomeration.

TEM image analysis of the micrograph was performed, and the result compared to the particle size distribution from the *PMS* analysis. Both analyses were observed to be in good agreement, and consistent with the findings from SnO_2 synthesis.

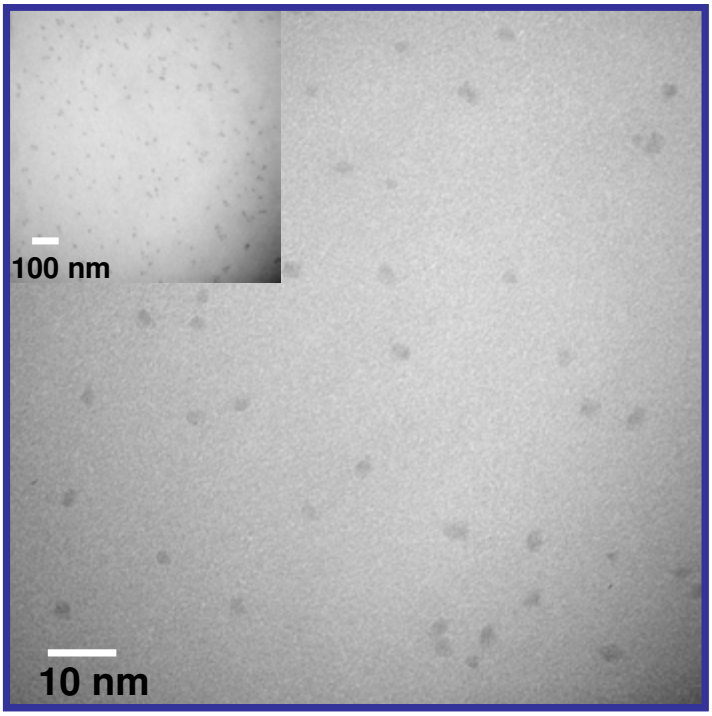

Figure 4.27: *TEM* micrograph of TiO_2 nanoparticles sampled with the molecular beam assisted particle deposition system; the insert shows the particle deposition on a lower magnification

UV spectroscopy of the flame synthesized TiO_2 nanoparticles was performed, and the result presented on Figure 4.28 (insert) as normalized reflectance of the material as a function of the wavelength of the incident light. The spectrum indicates that TiO_2 reflectance decreases in the *UV* range that begins at about 390 nm. This value corresponds well to the literature reported optical behaviour of anatase TiO_2 [90]. Analysis of the reflectance spectra with the *Kubelka-Munk* function (Figure 4.28) yielded an optical band gap of 3.33 eV that is significantly different from the 3.0 eV for rutile, and 3.2 eV for anatase, reported in literature [90]. The explanation for this

discrepancy could not be established within the context of this research. However, this observation presents a platform for future works on the crystal structures of titania.

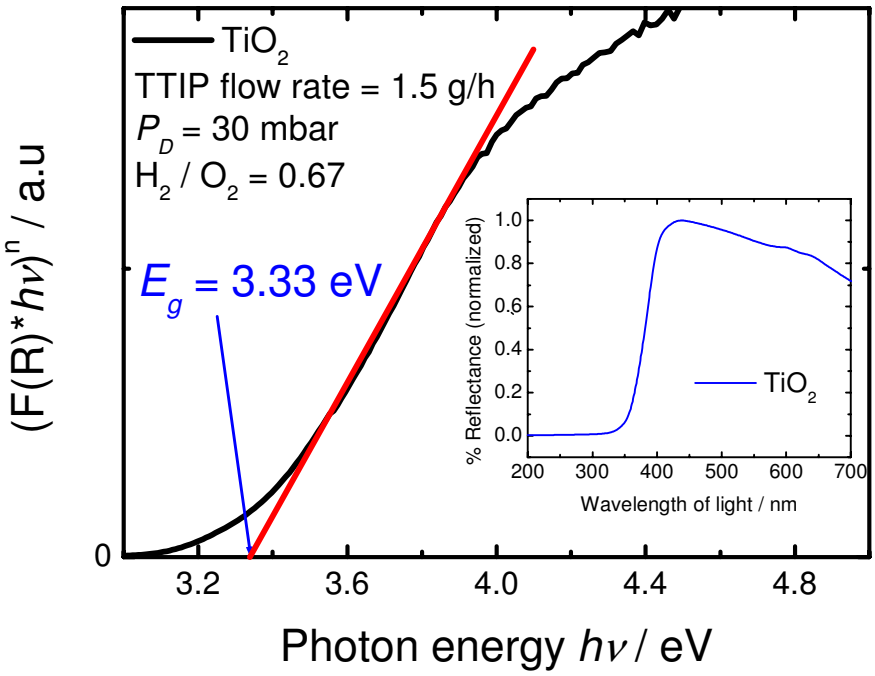

Figure 4.28: Analysis of the optical band gap of nanosized TiO_2 particles; the insert shows the normalized reflectance spectra of the as-synthesized TiO_2 nanoparticles

4.2.3 **Photocatalytic activity of flame synthesized TiO_2 nanoparticles**

The photocatalytic activity of the flame generated titania was investigated and compared to commercial titania powder, by using the materials for the photo-mineralization of 4-chlorophenol (*4CP*). The experimental set-up consist of a conical flask reactor made of quartz glass, *UV* lamps, membrane pumps, a gas chromatograph, CO_2 gas for calibration of the chromatograph and O_2 for the mineralization reaction. Three different titania powders were selected, whereby two of these powders were synthesized in the low-pressure flame reactor while the third powder was from Degussa (P25). The mineralization of *4CP* was performed separately with each of the powder sample. *4CP* was used as the model volatile organic compound (*VOC*), due to previous success with this material for mineralization investigations [91]. Before the experiment began, the set-up was initially calibrated with CO_2 to ensure that the correct

concentration of CO_2 was measured. The *VOC* was then placed in the reactor containing 100 mg of titania powder, and the pH value was adjusted with perchloric acid. 500-700 ppm of O_2 gas was then pumped into the reactor while a magnetic stirrer was used to stir the mixture. The mineralization of *4CP* should yield CO_2 gas, as an indicator that mineralization has occurred. A maximum of 5% CO_2 is expected from this reaction as reported in literature [91].

The result obtained for flame synthesized titania powders with *BET* surfaces of 156 and 234 m^2/g, as well as from P25 (*BET* surface = 50 m^2/g) are presented in Figure 4.29. The 234 m^2/g flame synthesized TiO_2 and P25 showed better photocatalysis than the 156 m^2/g powder. Further analysis of the flame synthesized powders, indicates that the 156 m^2/g powder shows significantly more rutile structure than the 234 m^2/g powder.

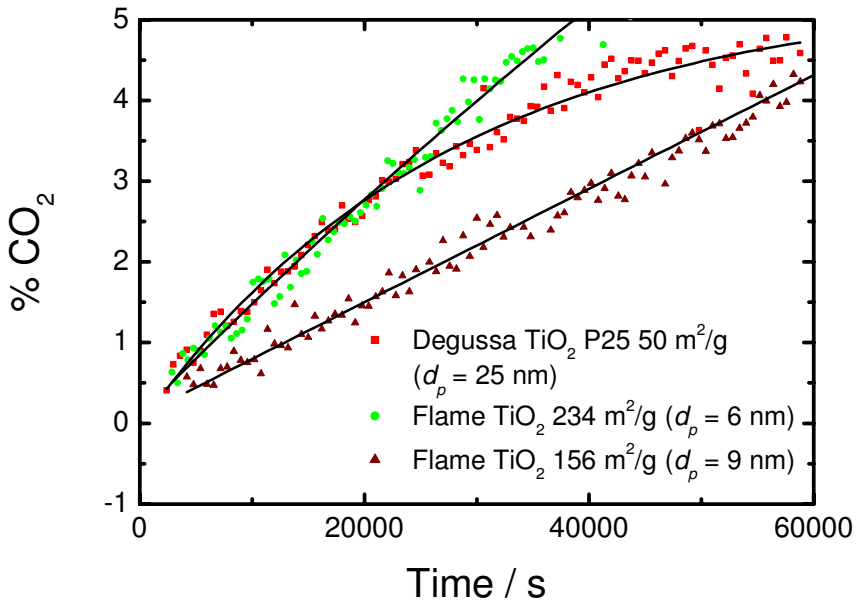

Figure 4.29: Comparative analysis of photocatalytic activity of flame synthesized TiO_2 powders and commercial TiO_2 (Degussa P25)

Hence the improved photocatalytic activity observed for the 234 m^2/g powder can be attributed to its anatase structure and smaller mean particle diameter, which influences the quantum efficiency of TiO_2.

The quantum efficiency of titania is determined by the competition for charge carriers between the *RedOx* reactions, and the electron-hole recombination process, and

has been reported to be a function of the particle diameter [92]. From this investigation, the synthesis of TiO_2 was successfully performed and characterized. Furthermore, the photocatalytic efficiency of the powder has been established whereby, the mean particle size was observed to influence this efficiency.

4.3 TiO_2-SnO_2 mixed oxide nanoparticles

In order to improve the quantum efficiency of TiO_2 particles several suggestion were proffered. These include the synthesis of a TiO_2-SnO_2 nanocomposite, which should prevent the recombination of electrons and holes, hence improving the quantum efficiency of the photocatalytic material [41]. However, the objective of this investigation was rather to synthesize and "tune" the band gap of titania. The aim is to generate a TiO_2-SnO_2 nanocomposite, whereby the presence of two different elements in an oxide matrix is expected to result in a band gap change. The objective was achieved by doping the premixed H_2/O_2/Ar flame with dilute concentrations of titanium tetra isopropoxide (*TTIP*) and tetramethyl tin (*TMT*) simultaneously. From the phase diagram of TiO_2 and SnO_2 (see Figure 4.30), the conditions necessary to generate several composite arrangements (mixed or segregated oxides) are displayed. Therefore, in other to synthesize mixed oxide particles in the flame, which has a maximum temperature of 1400 K, *TTIP:TMT* concentration ratios of 10:1, 4:1 and 1:1 were selected.

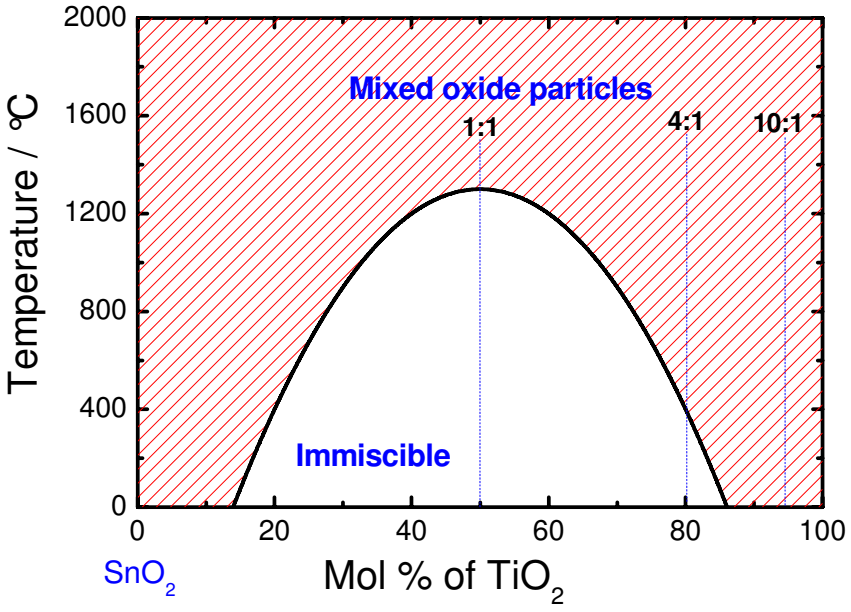

Figure 4.30: Phase diagram of TiO_2 and SnO_2 showing immiscible and mixed oxide sections

4.3.1 Synthesis of TiO_2-SnO_2 mixed oxide nanoparticles

For the synthesis of the TiO_2-SnO_2 nanoparticles, dilute concentrations of *TTIP* and *TMT* were sent co-currently via separate pipes into the reactor. The precursors were initially mixed in a small chamber behind the burner matrix, whereby, glass pearls in this chamber improves the mixing process by turbulence. It is assumed that no reaction of the precursors occur during the initial mixing, due to high argon dilution rates, low temperature of the chamber and low residence time. The parameters for the flame synthesis of TiO_2-SnO_2 nanoparticles are given as:

Precursors concentrations ratio (*TTIP:TMT*)	(10:1; 4.1; 1:1)
Reactor pressure P_D	30 mbar
H_2 / O_2 ratio	0.58 – 0.75
Inlet gas velocity v_u	1.32 m/s
Height above burner *HAB*	80 – 200 mm

Based on previous synthesis of TiO_2 and SnO_2, the H_2/O_2 ratio was selected to ensure sufficient oxygen (factor 20 in excess) for complete oxidation of the metalorganic precursor. A white coloured powder was obtained from each of the three experiments with varying precursor concentration ratios. The materials were consequently characterized with both in-situ and ex-situ characterization techniques.

4.3.2 Characterization of the TiO_2-SnO_2 mixed oxide particles

The mean particle diameters of the composite materials were investigated with the *PMS* for changes with respect to variation of the *HAB* as shown in Figure 4.31. For the evaluation of the count mean diameters (*CMD*) from the *PMS* signal, the density of the composite material was calculated based on the concentration of the precursors in the inlet gas mixture. This method has been described and reported in detail elsewhere [27].

From the *PMS* result, the particles were observed to show "delayed growth" whereby, the first particle diameter was detected at relatively high *HAB* (170 mm). The mean particle diameter was observed to increase with rising *HAB,* which is an established trend for particles synthesized with dilute precursor concentrations in this reactor. The mean particle diameters were observed to change from 5.3 to 8.3 nm for a *HAB* difference of 30 mm and a geometric standard deviation change between σ_g = 1.19 and 1.25. The error bars on Figure 4.31 represent the geometric standard deviation

measured at different *HABs* and was observed to increase with rising *HAB*. In general the TiO_2-SnO_2 nanoparticles exhibit similar particle growth tendency like other metal oxide particles synthesized in the low-pressure premixed flame reactor.

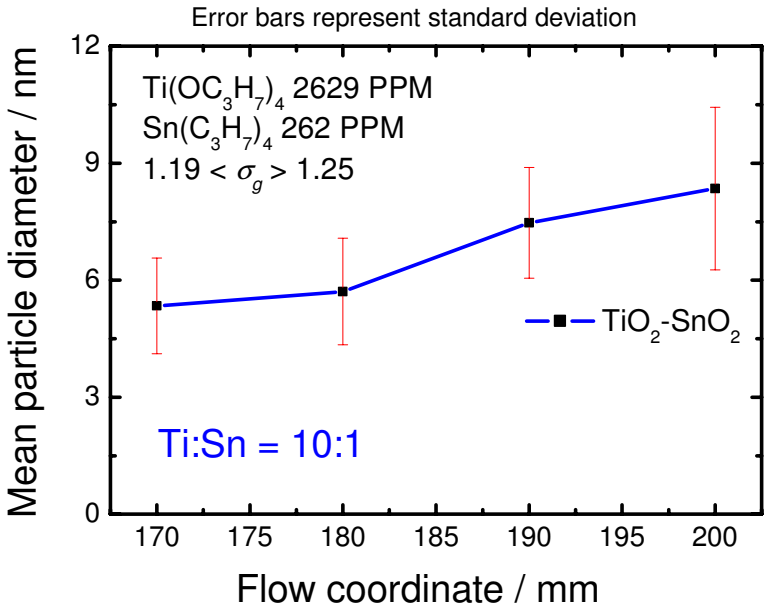

Figure 4.31: The influence of the mean particle diameter of TiO_2-SnO_2 nanoparticles from the flow coordinate Ti:Sn = 10:1

White TiO_2-SnO_2 particles thermophoretically deposited on the reactor walls as well as in the particle filter system were collected and analyzed with *XR*D. This was to determine the crystallinity of the material, as well as provide information on the type of metal oxide arrangement (either nanocomposite or mixed oxide) obtained. The *XRD* of TiO_2-SnO_2 powder was compared to the *XRD* spectra of pure SnO_2 as shown in a diffractogram on Figure 4.32. The high crystallinity of the synthesized materials was confirmed from the Bragg reflexes on the diffractogram. Segregated TiO_2 and SnO_2 Bragg reflections were not identified on the diffractogram, which implies that a nanocomposite arrangement was not achieved during his synthesis. Rather, a mixed oxide arrangement was obtained. For a mixed oxide arrangement, it is assumed that Sn^{4+} was either substitutively or interstitial placed in the crystal lattice of TiO_2. Hence the mixed oxide arrangement can best be depicted as $Ti_{1-x}Sn_xO_2$ arrangement, whereby, *x* represents the concentration of Sn^{4+} in the TiO_2 lattice. Furthermore, despite the high *TTIP* concentration for all experiments, the spectra of the synthesized materials tended

towards the spectrum of pure SnO_2 (Figure 4.32). Further observation indicates that a direct correlation can be established between the *TMT* concentration in the inlet gas mixture, and the optical properties of the mixed oxide.

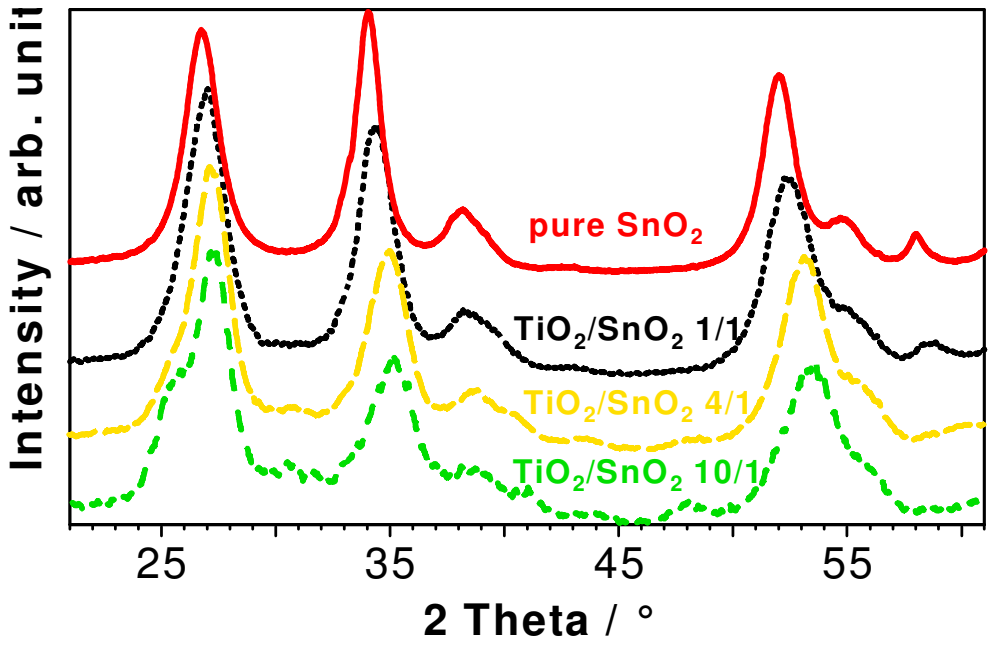

Figure 4.32: Normalized *XRD* of TiO_2-SnO_2 mixed oxide nanoparticles and pure SnO_2 nanoparticles synthesized in the low-pressure premixed flame reactor

The lattice parameters of the mixed oxides were calculated from the diffractogram and compared to the values for pure TiO_2 and SnO_2. The result presented in This observed phenomenon can be attributed to the SnO_2 that readily crystallizes into the tetragonal rutile arrangement when synthesized in the low-pressure reactor. Hence, the addition of SnO_2 into the crystal lattice of anatase TiO_2, results in its transformation into a rutile crystal structure. SnO_2 is thus referred to as a "rutilizer" because of this observed phenomenon.

Table 4.2 shows that the lattice parameters for the mixed oxides lie between that of the rutile TiO_2 and the rutile SnO_2. The parameters correspondingly change with the SnO_2 concentration in the mixed oxide arrangement. This result clearly confirms the optical observation from the *XRD* analysis, whereby a shift in the spectrum of each mixed oxide can be correlated to the concentration of tin precursor in the inlet gas mixture. Furthermore, as-synthesized TiO_2 from the low-pressure premixed flame reactor shows predominantly the anatase crystal structure with some traces of the rutile arrangement.

However, when low concentrations of *TMT* were included along with the inlet gas mixture, a mixed-oxide with rutile structure was generated. This observed phenomenon can be attributed to the SnO_2 that readily crystallizes into the tetragonal rutile arrangement when synthesized in the low-pressure reactor. Hence, the addition of SnO_2 into the crystal lattice of anatase TiO_2, results in its transformation into a rutile crystal structure. SnO_2 is thus referred to as a "rutilizer" because of this observed phenomenon.

Table 4.2: Comparative analysis of the lattice parameters for TiO_2-SnO_2 mixed oxides, TiO_2 and SnO_2 nanoparticles synthesized in the low-pressure flame

Concentration ratios		*a (nm)*	*c (nm)*	*c/a*
SnO_2		0.472	0.318	0.674
TiO_2 / SnO_2	1 : 1	0.468	0.315	0.673
TiO_2 / SnO_2	4 : 1	0.463	0.309	0.667
TiO_2 / SnO_2	10 : 1	0.464	0.305	0.657
TiO_2 (Rutile)		0.459	0.296	0.644

Vergard's law describes the linear relationship between the lattice parameters and composition of the composite materials (expressed in percentages). Based on this law, the lattice parameters of the mixed oxides should vary proportionally to the percentage composition of tin in the material. Figure 4.33 shows analysis of the lattice parameters for pure SnO_2, the mixed oxides, and TiO_2 based on *Vergard's* law.

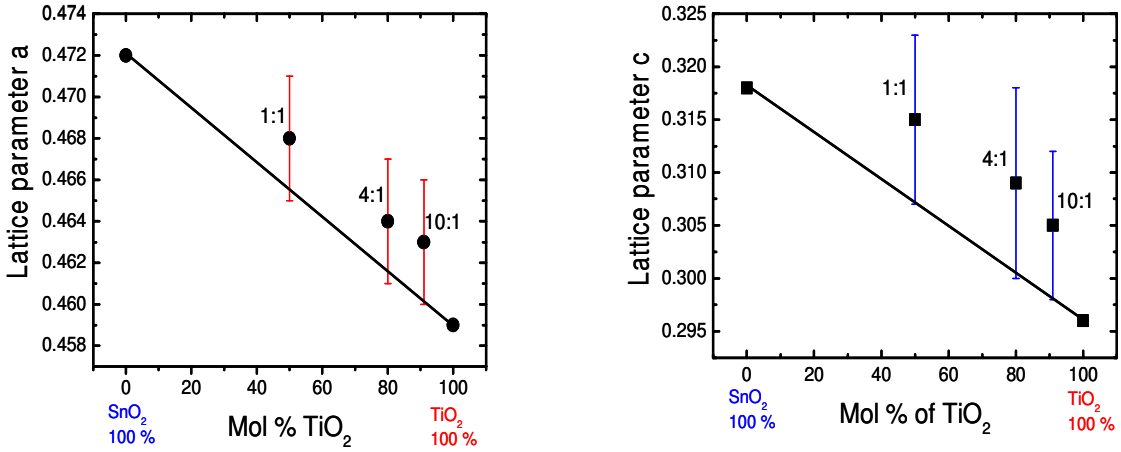

Figure 4.33: Lattice parameters a and c of the mixed oxides compared to the values for pure SnO_2 and TiO_2 according to *Vergard's* law

The error bars on the lattice parameters for the mixed oxides represent the deviation of these parameters based on *Vergard's* law. The trend for both lattice parameters (*a* and *c*) with varying (TiO_2 and SnO_2) composition was observed to be similar. However, the values of these parameters do not ideally comply with *Vergard's* law, although the deviations are considered to be tolerable.

UV reflectance spectra of the mixed oxides were performed and compared to the results obtained for pure TiO_2 and SnO_2 nanoparticles. From the initial reflectance spectrum, significant differences were not observed for the materials under investigation. However, differentiation of the reflectance with respect to the wavelength of the incident light was performed, which revealed significant differences between the materials. The result of this mathematical operation is presented in Figure 4.34, whereby, the maximum of the mixed oxides spectra were observed to lie sequentially between those of SnO_2 and TiO_2.

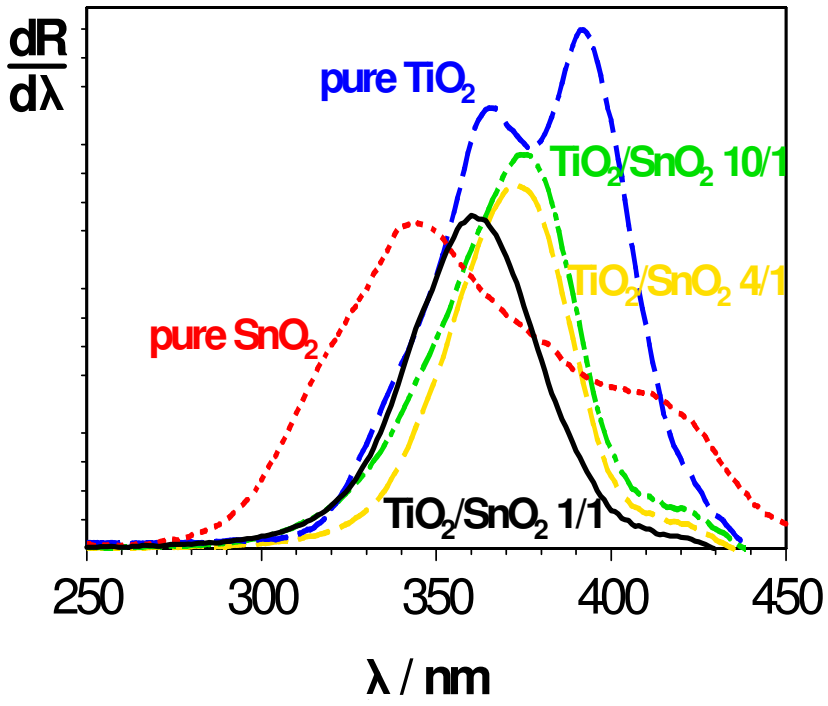

Figure 4.34: Comparative analysis of the differential of the optical reflectance of the mixed oxide, TiO_2 and SnO_2 nanoparticles with respect to the wavelength of the incident light

The position of the maximum can be correlated to the SnO_2 concentration in the mixed oxide powder, whereby, each mixed oxide has a different optical band gap that varies with the SnO_2 content. This implies that by varying the concentration ratios of *TMT* and *TTIP* in the inlet gas mixture, the band gap of the resulting mixed oxide can be "tuned" [80].

The mixed oxide particles (*TTIP:TMT, 4:1*) were sampled on a micrograph using the pneumatic assisted *TEM* sampling device. Figure 4.35A shows the TiO_2-SnO_2 nanoparticles, with a relatively high degree of soft and hard agglomerates. The particle morphology was observed to be spherical and the particle diameters are below 10 nm. The particles appear homogenous with no traces of islands where segregated TiO_2 and SnO_2 exist. Energy dispersive spectroscopy (*EDX*) was performed on particle ensembles as well as on single isolated particles (nano-beam investigation) to determine qualitatively and quantitatively the composition of the as-synthesized materials. The *EDX* results established the presence of Ti, Sn and O in both the particle ensemble as well as on single isolated particle. However, quantitative analysis of the elements did not yield a result that corresponds to the *TTIP:TMT* ratio in the inlet gas mixture.

Hence, it was concluded that the composition of the mixed oxides do not precisely correspond to the precursor mixing ratio. However, the trends of the precursor mixing ratios were sustained in the end products (mixed oxides).

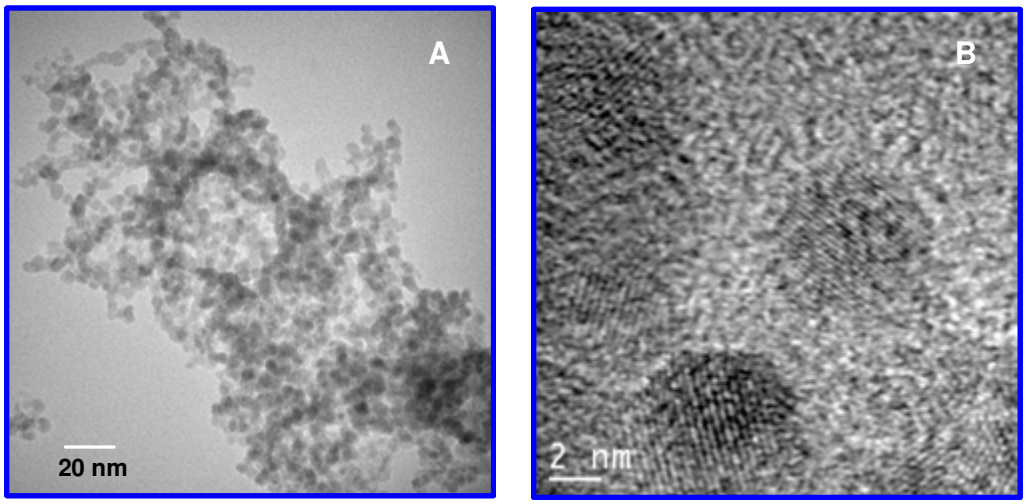

Figure 4.35: A) *TEM* micrograph of TiO_2-SnO_2 (4:1); B) *HR-TEM* of the same particle sampled with the pneumatic assisted *TEM* sampling device

HR-TEM of the TiO_2-SnO_2 mixed oxide was also performed as shown in Figure 4.35*B*, whereby the particle morphology was confirmed as spherical. The lattice fringes, which are an indication of the well ordered crystallite, can be seen as parallel lines on the particles. Hence, the mixed oxide was confirmed as being highly crystalline.

BET analyses of the mixed oxide particles were performed with a 5 point *BET* measuring equipment described previously in section 3.5.2. Depending on the *HAB* selected during synthesis, mixed oxides with *BET* values between 176 and 234 m^2/g were obtained. These surface areas are quite large in comparison to commercial titania (Degussa P25) with a surface area of 50 m^2/g [93]. The *BET* values where converted into equivalent diameters based on the spherical morphology of the particles as observed on the *HR-TEM* micrograph (Figure 4.35). The densities used were calculated empirically based on the precursor concentrations used for the synthesis of the mixed oxides. The results were compared to diameters obtained from *PMS* and *XRD*.

Figure 4.36 indicate that all methods show similar tendencies, whereby the mean particle diameter rises with increase of the *TTIP* composition in the inlet gas mixture. This increase is due to the relatively high precursor concentrations selected for higher

TTIP:TMT ratios (*TTIP:TMT 2629:262*). As a result, more frequent coagulation, coalescence and surface growth of species occur, leading to large particles.

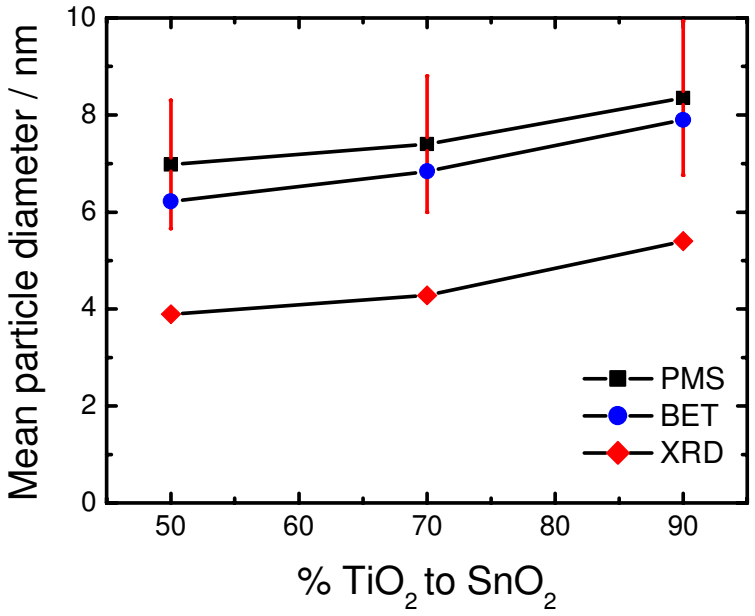

Figure 4.36: Comparative analysis of particle diameters obtained from *PMS*, *BET* and *XRD* analysis of the TiO_2-SnO_2 mixed oxide particles

The result of the *XRD* (crystallite size) differs somewhat from the *BET* and *PMS* measurements. The crystallite size represents the size of the particle crystal with an ordered lattice, whereby, crystalline flame synthesized materials often have an amorphous shell encasing a crystal core. Furthermore, particle size from *XRD* analysis in this size regime, introduces some uncertainties that make the result difficult to compare with other particle sizing technique. Hence, the crystallite size is often lower than the mean particle diameter and is thus not considered as the mean particle diameter of the material. However, the tendency of its change with respect to the TiO_2 content validates the trend observed for *BET* and *PMS* analysis.

The formation of TiO_2-SnO_2 mixed oxide in the low-pressure flame can be attributed to the temperature and precursor ratios selected for the synthesis. Based on the phase diagram of both oxides (see Figure 4.30) the selected synthesis parameters should result in miscible oxides, which was confirmed by *XRD* and *UV-Vis* analysis of the mixed oxides. Furthermore, due to the high temperature gradient and short residence

time in the low-pressure reactor, a specific composition of the material is often "frozen" that result in kinetically controlled synthesis of the materials.

4.3.3 Electrical properties of the TiO_2-SnO_2 mixed oxide nanoparticles

The electrical properties of the mixed oxides were investigated under ambient conditions and compared to that of pure TiO_2 and SnO_2. The result of the investigation is presented in Figure 4.37, whereby $\ln G'$ represents the real part of conductivity (inversely proportional z') of the material.

From the result, TiO_2 exhibits very poor conductivity, in contrast to pure SnO_2. The mixed oxides (1:1 and 10:1) show conductivities that lie between pure TiO_2 and SnO_2. The conductivity of the mixed oxide was observed to vary with the Sn content, whereby the mixed oxide with higher Sn content showed the higher conductivity in comparison to the other. This result is in accordance with the trends observed from *XRD* and *UV-Vis* investigations of the mixed oxide powders.

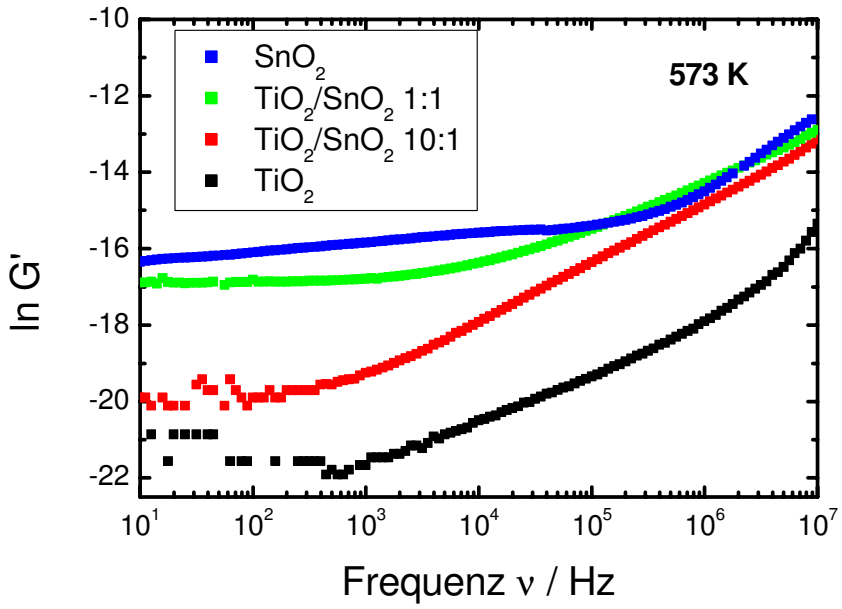

Figure 4.37: Comparative analysis of the conductivity of the TiO_2-SnO_2 mixed oxides as well as, TiO_2 and SnO_2 nanoparticles synthesized in the low-pressure premixed flame

In conclusion, the exact arrangement of the mixed oxide crystal lattice with respect to the position of Ti and Sn was not established in the course of this research (interstitial or

substitutive). However, lattice parameters as observed, can only change when Ti is substitutionally replaced by Sn. It is obvious from the characterization methods employed that a mixed oxide was synthesized in the low-pressure premixed flame reactor.

4.4 Time resolved laser induced incandescence (*TiRe-LII*)

An attempt to measure the particle size of iron oxide (Fe_2O_3) nanoparticles, synthesized in the low-pressure premixed H_2/O_2/Ar flame reactor, with the time resolved laser induced incandescence (*TiRe-LII)* method was performed. The objective of this investigation was to implement a fast, non-intrusive and independent online-particle sizing technique, which will be compared to the results obtained from the particle mass spectrometer (*PMS*) of the metal oxide nanoparticles. The *PMS* has successfully been tested on different nanosized oxides and non-oxides, synthesized under low-pressure conditions [19,58,59], while the *TiRe-LII* has also been implemented in several processes and on different nanosized materials [64,65]. However, both methods have limitations due to assumptions necessary for the simplification of the analysis. *TiRe-LII* is dependent on the ability of the material to absorb and radiate energy that it receives from a laser pulse, whereby, soot is known to be a model material for this analysis. Furthermore, soot particles were previously characterized with the *PMS* in the low-pressure reactor with huge success [62]. Hence, soot was selected as a model particle for the investigation and validation of both measurement techniques.

4.4.1 Synthesis and characterization of Fe_2O_3 nanoparticles

Fe_2O_3 was synthesized by doping the low-pressure H_2/O_2/Ar premixed flame with dilute precursor concentrations of iron pentacarbonyl ($Fe(CO)_5$). The precursor was diluted in the same manner as for SnO_2 synthesis and the concentration in the flame was controlled with a mass flow controller. The flame conditions were similar to that for SnO_2 synthesis; however the reactor pressure was varied between 40 and 50 mbar. The parameters for the synthesis are hereby listed as:

Reactor pressure P_D	40 - 50 mbar
Fe_2O_3 concentration	300 – 1000 ppm
Inlet gas velocity v_u	1.32 m/s
Height above burner *HAB*	60 – 180 mm

A typical *TiRe-LII* raw-signal for a detection wavelength λ_{detect} = 550 nm as a function of the cooling time, measured at conditions p = 50 mbar and *HAB* = 100 mm is shown in Figure 4.38.

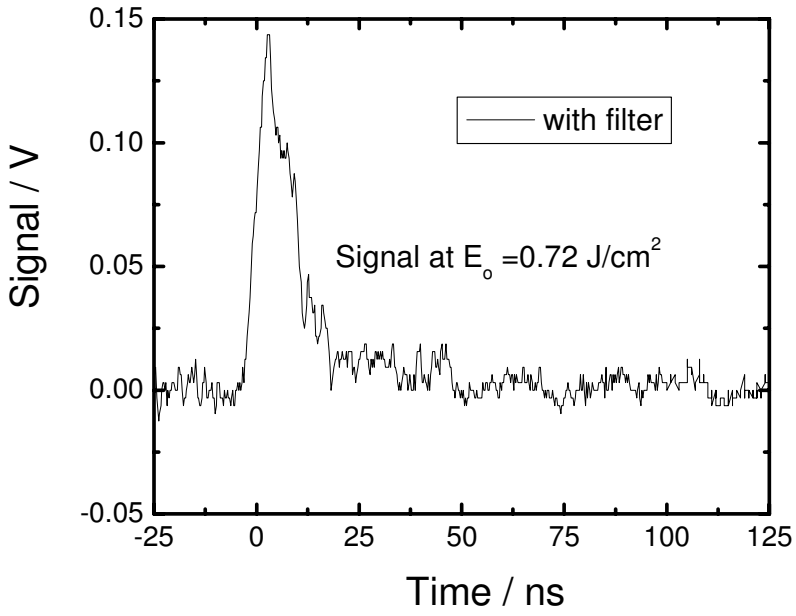

Figure 4.38: *TiRe-LII* signal of Fe_2O_3 nanoparticles measured at detection wavelength of 550 mm, *HAB* = 100 mm, and reactor pressure = 50 mbar, with filter

The sudden rise and consequent cooling profile signal does not exhibit a typical *TiRe-LII* signal for nano-particulate materials, due to the "irregular" nature of the cooling profile. Furthermore, the laser energy density used was very high (0.72 J/cm^{-2}), whereby, the high laser energy can result in the evaporation of the sample materials. In other to ascertain if it is possible to obtain relatively good signals with low signal-to-noise ratio, the optical filter was removed so as to subject the particles to a wider laser wavelength spectrum without high energy density. The signal for this measurement is presented in Figure 4.39. This signal shows a better profile with relatively longer cooling time and lower laser energy density (0.22 J/cm^{-2}). However, by removing the filter, the *TiRe-LII* measurements have been compromised and the result cannot be evaluated for particle size information.

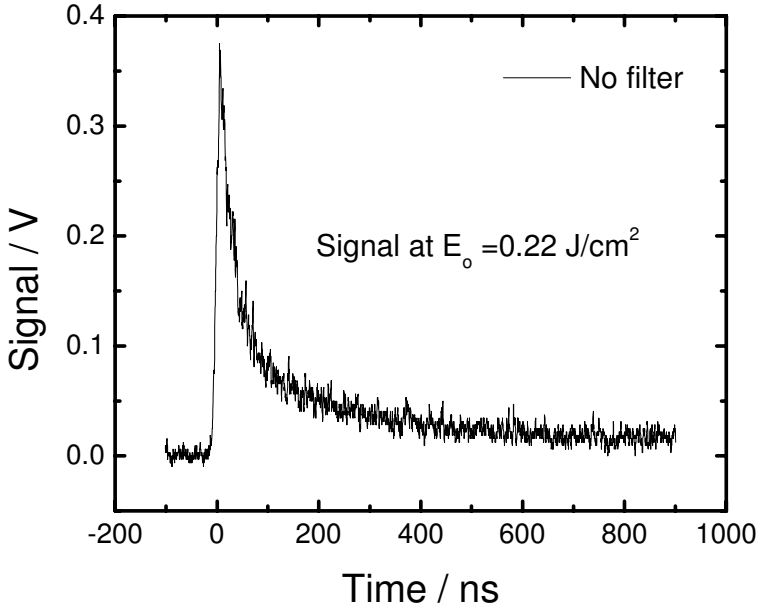

Figure 4.39: *TiRe-LII* signal of Fe_2O_3 nanoparticles measured at detection wavelength of 550 mm, *HAB* = 100 mm, and reactor pressure = 50 mbar, without filter

Therefore, in other to demonstrate the practicability of the *TiRe-LII* measurement to particles generated in low-pressure conditions and subsequent comparison to *PMS*, a model material (soot) was investigated, with both measuring methods in the reactor.

4.4.2 **Synthesis of soot particles in the low-pressure reactor**

For the implementation of the *TiRe-LII* on soot particles in the low-pressure flame reactor, the experimental set-up previously described was used. A major requirement for the implementation of *TiRe-LII* is high particle concentration, which is necessary for the detection of the emitted energy from the particles with a photomultiplier. Hence, for this investigation, a sooty flame was used to ensure high concentrations of soot particles. The parameters for the synthesis and corresponding spectroscopy are given as follows:

Reactor pressure P_D	40 - 50 mbar
C_2H_4 / O_2 ratio	2.125 – 2.5
Inlet gas velocity v_u	1.32 m/s
Height above burner *HAB*	100 – 180 mm

The mean particle diameter of the soot particles generated under the conditions mentioned above, were investigated with *PMS* and *TiRe-LII,* while changing the height above burner *HAB* and the reactor pressure. The result obtained from both methods were analyzed and compared.

4.4.3 **Characterization of soot particles**

PMS measurements performed on soot particles at 40, 45 and 50 mbar as a function of *HAB* is presented in Figure 4.40. For all reactor pressures, the growth of the particle sizes with increasing *HAB* was observed. This observed behaviour was due to increased residence time at high pressures, which results in a high growth rates of the soot particles [12]. Furthermore, at high *HABs* (from 140 mm), saturation sets in, leading to insignificant change of the mean particle diameter with increasing *HAB*. This observation was attributed to the limitation of the *PMS* system in deflecting and consequently measuring large particles. Hence particles above a certain mass will not be deflected, which results in the saturation profile observed in Figure 4.40.

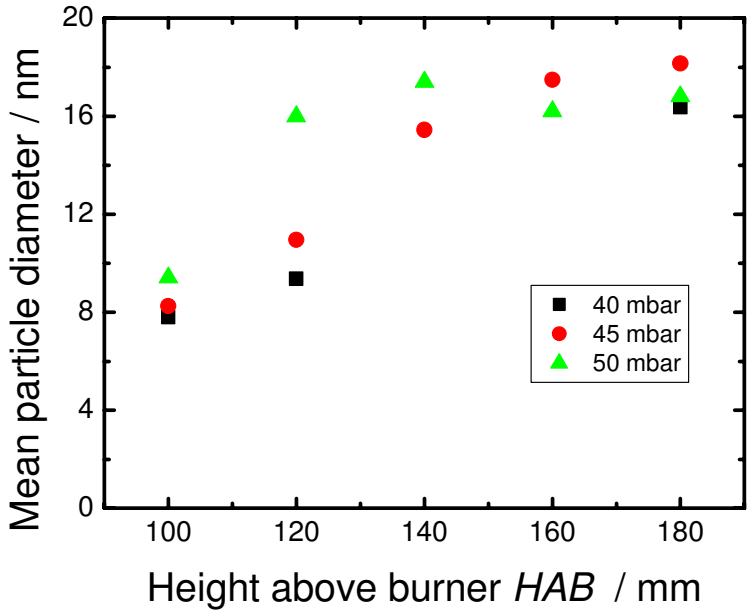

Figure 4.40: *CMD* values obtained from *PMS* measurement analysis at different reactor pressures and *HAB* positions

A typical *TiRe-LII* raw-signal for a detection wavelength λ_{detect} = 550 nm as a function of the cooling time, measured at conditions p = 50 mbar and *HAB* = 120 mm is shown

in Figure 4.41*A*. At time $t = 0$, which signifies the start of the laser pulse, a sudden signal increase due to particle heating is observed. The laser pulse duration is 6 ns, after which the particles radiate energy until the signal reaches its initial level after about 1700 ns. The section of the signal after the laser pulse duration was fitted with an exponential function that describes the cooling profile of the particles under investigation (see Figure 4.41*B*. The cooling time is relatively long because of the suppressed cooling by heat conduction due to the low-pressure conditions. The calculated *CMD* and σ_g from the analysis are 16 nm and 1.1, which are in good agreement with the *PMS* results for the same conditions. The shape of the fitted curve also agrees well with the measured signal. This result confirms that the used model provides a reasonable representation of particle cooling under low-pressure conditions.

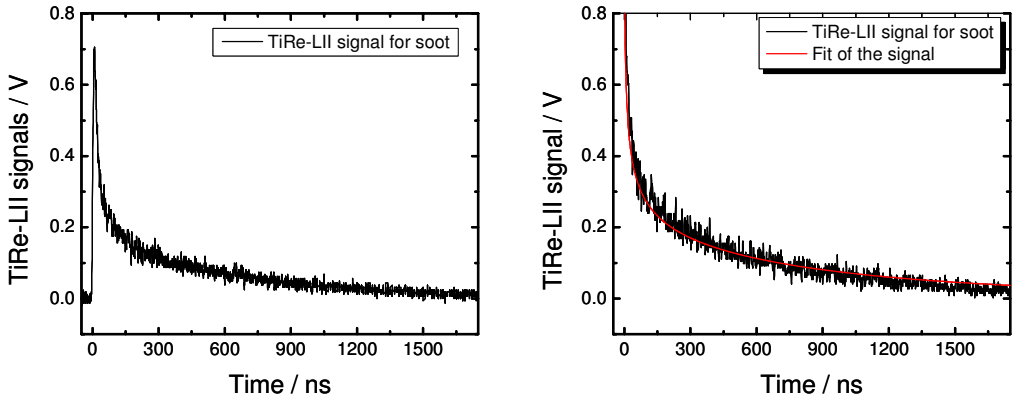

Figure 4.41:A) Typical *TiRe-LII* cooling signal; B) *TiRe-LII* cooling signal showing line of best fit for the curve, *HAB* = 120 mm

A set of normalized particle emission signals during cooling were obtained at three different reactor pressures as shown in Figure 4.42*A*. All signals were measured at $\lambda_{detect} = 550$ nm and *HAB* = 120 mm. The three decay curves have nearly the same characteristics, whereby no clear pressure dependence could be optically established. For the purpose of clarity, the signals were fitted with an exponential function as shown in Figure 4.42*B*. From this analysis, a slight increase of cooling time with the reactor pressure was observed.

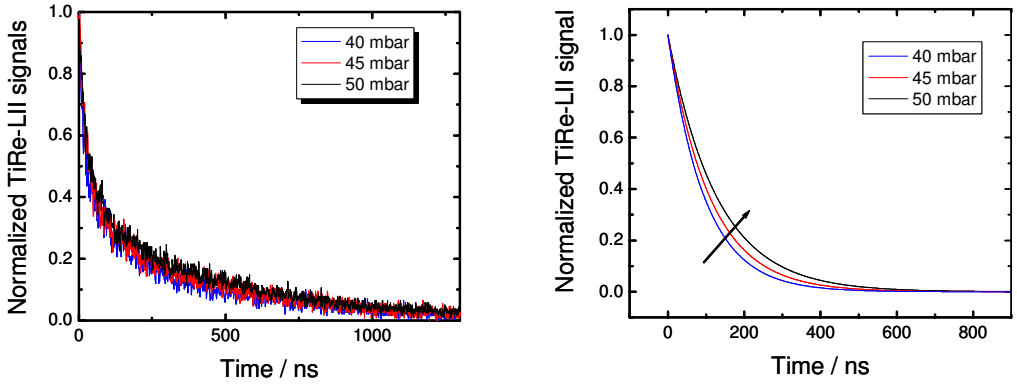

Figure 4.42: A) Normalized *TiRe-LII* signals measured at different reactor pressures; B) Normalized *TiRe-LII* signals measured at different reactor pressures fitted by exponential functions, *HAB* = 170 mm

The increase of the cooling time implies larger particles were measured for higher reactor pressure. Increased reactor pressure leads to lower aerosol velocity, longer residence time and consequently larger particles [88]. Evaluation of the particle size diameter as a function of the reactor pressure was consequently calculated from the original signal (Figure 4.42*A*). The results of the evaluation as well as the comparison to *PMS* generated results are presented in Figure 4.43.

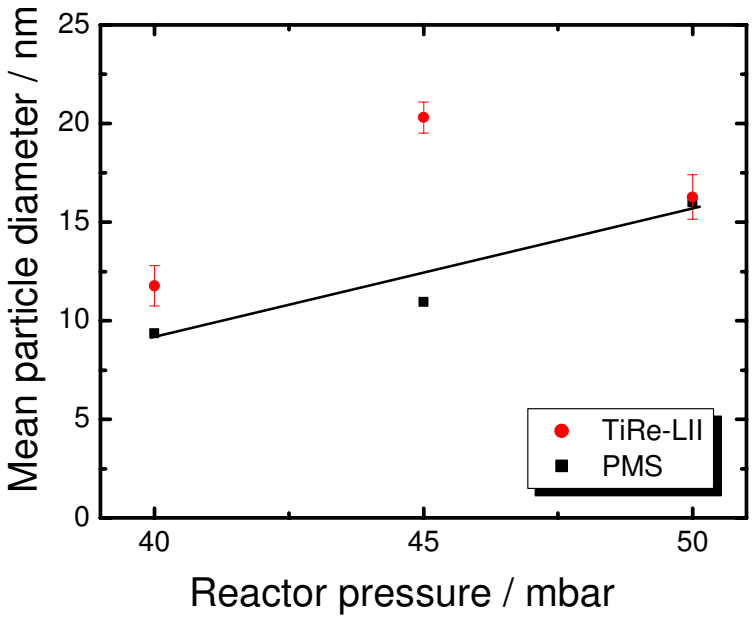

Figure 4.43: Comparison of *PMS* and *TiRe-LII* results for varying reactor pressure and constant residence time, *HAB* = 120 mm

Each *TiRe-LII* point shown in Figure 4.43 was averaged from three individual measurements and the deviation presented as error bars. The results of the two different measuring techniques are in good agreement. However the disparity observed especially at 45 mbar was due to instabilities from working at elevated pressures in the low-pressure reactor (above 40 mbar).

Figure 4.44*A* shows four *TiRe-LII* signals measured at 550 nm for different *HABs* in the reactor at a constant reactor pressure of 40 mbar. The recorded emission signals were normalized and fitted by exponential functions to establish the relationship between *HAB* and the cooling time of the particles. Higher *HAB*s that result in increased residence time for particle growth, was observed to be proportional to the particle cooling time. Hence longer cooling times were observed for higher *HAB* due to the larger diameters of the particles as a result longer growth times. In Figure 4.44*B* the results of *TiRe-LII* and *PMS* measurements with varying residence time at constant reactor pressures were compared. The evaluated *CMD*-values are presented as a function of *HAB*, whereby the trends of the CMDs measured by TiRe-LII are in good agreement. However, some disparity was observed in the actual values of the *CMD* obtained.

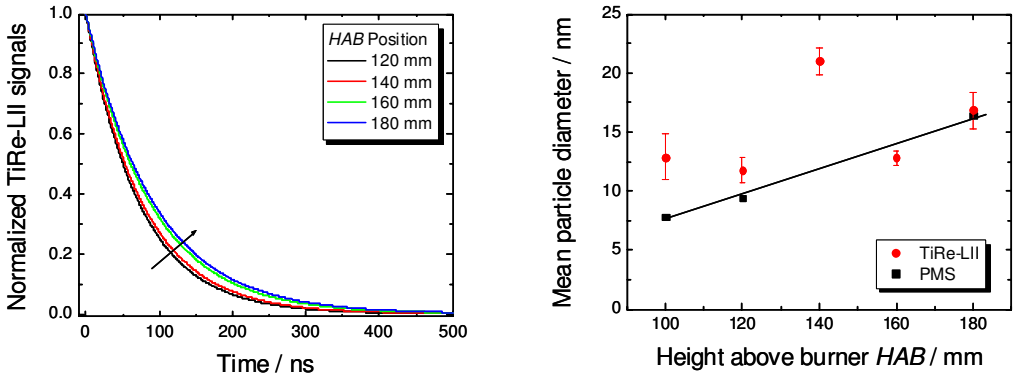

Figure 4.44: A) Normalized *TiRe-LII* signals measured at different *HAB* fitted by exponential functions; B) Comparative analysis of *PMS* and *TiRe-LII* results for varying *HAB* positions and constant reactor pressure

The present work demonstrates the applicability of time-resolved laser-induced incandescence (*TiRe-LII*) for soot particle-size measurements under low-pressure conditions. Quantitative data evaluation requires the solution of a differential equation system that consists of the energy and mass balance of a single particle during cooling. Due to the low-pressure conditions in the reactor the heat transfer from the particle to the surrounding gas takes place under free-molecular *Knudsen* number conditions. The heat flux due to heat conduction under these conditions is suppressed so that the dominating heat transfer at the relevant particle temperatures is caused by evaporation. Under the assumption of a lognormal distribution function of the particles in the reactor, the count median diameter (*CMD*) and geometric standard deviation (σ_g) were used to fit calculated signal curves to the measured signals by least square method. Analysis in terms of particle size distribution was done simultaneously by particle mass spectrometry (*PMS*) to provide an independent *in-situ* measurement for comparison. Both measurements were performed for variation of the reactor pressure and the height above the burner (*HAB*). It was observed that the particle diameters increase with increasing reactor pressure and *HAB*. The tendency of the *TiRe-LII* measured particle sizes are in good agreement with the results evaluated by *PMS*, however some discrepancies exist with the *CMD* values obtained from both processes.

Both methods have limitations that influence the obtained results. The *TiRe-LII* functions effectively at elevated pressures (above 40 mbar), whereby this pressure is already in the upper operational limit of the low-pressure flame reactor. Furthermore,

due to high soot concentration during synthesis, both measurements could not be performed simultaneously hence the results presented are based on the assumption that the particle diameters obtained are reproducible. Taking all these factors into consideration, the results presented are encouraging, but needs more improvement for eventual application in measuring metal oxide particles synthesized in the low-pressure remixed flame reactor.

5 Conclusion

The objective of this work was the investigation into the synthesis and characterization of nanosized semi-conducting metal oxide particles generated in a low-pressure premixed H_2/O_2/Ar flat flame. The materials were synthesized by doping the premixed flame with dilute concentrations of the precursors containing the metal source. Due to the high temperature of the flame, the precursor undergoes thermal dissociation (true for metalorganics), followed by a gas-phase reaction and homogenous nucleation, which results in a supersaturated vapour of the metal oxide. At lower temperatures downstream of the flame, this vapour condenses into solid particles. The size of the particle continues to grow depending on the temperature and residence time distribution, by a combination of processes that includes surface growth, Brownian coagulation and coalescence. The final product is often a mix of single particles, soft and hard agglomerates as well as aggregates, which are thermophoretically collected as metal oxide powders on a cool substrate in the reactor and in a particle filter system for *ex-situ* analysis. An in-built particle mass spectrometer was used to investigate the influence of experimental parameters (height above burner *HAB*, precursor concentration, pressure) on the mean particle diameter of the powder material during synthesis, with relatively good success. In this work, research into the synthesis and characterization of tin oxides, titanium dioxide and titanium-tin mixed oxide were performed. By varying the temperature-time history of the process (oxygen/fuel ratio and height above burner (*HAB*)), the mean particle diameter, particle size distribution, oxidation state and crystallinity of metal oxide nanoparticles were influenced.

Tin oxide nanoparticles were synthesized in the low-pressure reactor with dilute concentrations of tetra methyl tin in argon. The SnO_2 particles were observed to be crystalline with the rutile tetragonal structure and spherical morphology. By increasing the H_2/O_2 ratio in the flame oxygen vacancies are created in the crystal lattice of tin oxide that results in non-stoichiometric SnO_x nanoparticles were $1 < x < 2$. Hence, tuning of the stoichiometry was achieved for this reactor geometry and gas composition. The electrical properties of SnO_2 and SnO_x were investigated, whereby due to oxygen vacancies in SnO_x, increased conductivity was observed in comparison to SnO_2 nanoparticles. Hence, SnO_x particles with tuned stoichiometry are suitable candidates for metal oxide based gas sensors.

Titania (TiO_2) nanoparticles were synthesized by doping the low-pressure flame with dilute concentrations of titanium tetra iso-propoxide (*TTIP*) with either the controlled evaporation and mixing device (*CEM*) or the pressure controlled precursor delivery system. The titania particles were crystalline with a mixed anatase (dominant) and traces of rutile (recessive) structure, whereby the mean diameter was observed to be between 3 and 9 nm depending on the *HAB*. The rutile arrangement in the titania powder increased significantly for higher hydrogen H_2 content in the inlet combustion gas. The photocatalytic property of two flame synthesized titania samples were compared to commercial titania P25 (d_p = 25 nm, *BET* = 50 g/m^2) from Degussa. The flame synthesized titania with high anatase arrangement and 6 nm mean particle diameter (*BET* = 234 g/m^2) exhibited comparable performance to P25, which was better than the high rutile content, 9 nm (*BET* = 156 g/m^2) flame synthesized titania. Hence the photocatalytic property of titania is influenced by its surface area, crystallinity, crystal structure, and consequently its quantum efficiency.

Synthesis of a TiO_2-SnO_2 nanocomposite was proposed for the purpose of band gap "tuning" of TiO_2. This mixed oxide was synthesized by simultaneously doping the low-pressure flame with dilute concentrations of *TTIP* and *TMT*. The mixing ratios were varied (*TTIP:TMT* 10:1, 4:1 and 1:1) and the resulting oxides were characterized with both *in-situ* and *ex-situ* techniques. The as-synthesized oxide was confirmed from *XRD* analysis to be crystalline. Separate Bragg reflections from TiO_2 and SnO_2 were not identified from the diffractogram, whereby this result signals a segregated TiO_2, SnO_2 powder system. Rather, the spectrum was observed to be similar to that of pure SnO_2 with a significant shift in lattice constants, depending on the SnO_2 content of the mixed oxide. It was thus concluded that Sn^{4+} (which has a larger radius than Ti^{4+}) displaces Ti^{4+}, and is substitutively incorporated in the crystal lattice of TiO_2. This resulted in a mixed oxide with the composition $Ti_{1-x}Sn_xO_2$. Finally, electrical characterization of the mixed oxides were performed and compared to the highly conductive SnO_2 and the poorly conductive TiO_2. The result show that with increasing *TMT* in the inlet gas, the conductivity of the mixed oxide improves considerably. This confirms that progressive increase in the concentration of Sn^{4+} in the crystal lattice of TiO_2 can be used to "tune" the optical and electrical properties of these mixed oxides.

Time resolved laser induced incandescence (*TiRe-LII*) was performed in the low-pressure reactor to validate the result obtained from the in-built *PMS* system. Both systems have been previously tested for different materials under different conditions,

hence performing simultaneous measurements with both methods was proposed. For this analysis, soot was used since both methods have shown good results for characterizing soot particles generated from combustion processes. A sooty flame was generated and both measuring techniques were implemented for different reactor pressures (40, 45 and 50 mbar) and different *HAB* (120-180 mm). For both investigations, the trends of the result were identical and validate each other to some extent. However, discrepancies exist between both methods on the actual value of the *CMD* recorded. The observed difference in the *CMD* obtained from both methods was attributed to the operational limits of these technique as well as errors with these measurements. The soot particles synthesized were rather large for the *PMS* to measure in many cases due to the high concentration of carbon species from the acetylene. Secondly the reactor pressures were set at the upper limits of the flame reactor that sometimes resulted in flame instabilities. The geometric standard deviations for both techniques were found to be in good agreement. Overall this method has some promising potential, however the real challenge exist in implementing this technique for measuring metal oxide nanoparticles synthesized in the low-pressure reactor. The TiRe-LII was successfully applied in the low-pressure flame reactor for the first time.

6 References

1. G. D Ulrich, "Theory of Particle Formation and Growth in Oxide Synthesis," Combust. Sci. Tech **4**, 47-57 (1971).
2. K. Wegner and S. E. Pratsinis, "Scale-up of nanoparticle synthesis in diffusion flame reactors," Chem. Eng. Sci **58**, 4581-4589 (2003).
3. M. A. Ratner and D. Ratner, *Nanotechnology. Gentle Introduction to the Next Big Idea* (Prentice Hall International, 2002, 208).
4. R. kudrawiec, M. Nyk, M. Syperek, A. Podhorodecki, and J. Misiewicz, "Photoluminescence from GaN nanopowder: The size effect associated with the surface-to-volume ratio," Appl. Phys. Lett. **88**, 181916-181918 (2006).
5. S. Hahn, *SnO_2 thick folm sensors at ultimate limits: Performance at low O_2 and H_2O concentrations; size reduction by CMOS technology*, in *Fakultät für Chemie und Pharmazie*. 2002, Erberhard-Karl Universität: Tübbingen. p. 161.
6. Z. Zhang, C. Wang, R. Zakaria, and J. Y. Ying, "Role of particle size in Nanocrystalline TiO_2-based photocatalysts," J. Phys.Chem B **102**, 10871-10878 (1998).
7. N. Ohashi, T. Ishigaki, N. Okada, H. Taguchi, I. Sakaguchi, S. Hishita, T. Sekiguchi, and H. Haneda, "Passivation of active recombination centers in ZnO by hydrogen doping," J. Appl. Phys **93**, 6386-6392 (2003).
8. Y. Suzuko and H. Tomoko, "Photocatalytic activity of TiO_2 synthesised by the sol-gel method," J. Chem. Res **7**, 423-425 (2003).
9. C. Y. Wang, T. W. Chen, C. C. Lin, W. J. Hsieh, K. L. Chang, and H. C. Shih, "Synthesis, characterization and cathodoluminescence of nanostructured SnO2 using microwave plasma enhanced CVD," J. Phys D **40**, 2787-2791 (2007).
10. Y. Chen, X. Xue, and T. Wang, "Large-scale controlled synthesis of silica nanotubes using zinc oxide nanowires as templates," Nanotechnology **16**, 1978-1982 (205).
11. H. K. Kammler, L. Maedler, and S. E. Pratsinis, "Flame synthesis of nanoparticles," Chem. Eng. Technol **24**, 583-596 (2001).
12. C. Janzen, *Untersuchung zur Synthese von Eisenoxid-Nanopartikeln in der Gasphase*, in *Dissertation*. 2002, University of Duisburg-Essen: Duisburg. p. 99.
13. G. P. Fotou, S. J. Scott, and S. E. Pratsinis, "Effect of Ferrocene additive on the flame synthesis of Silica particles," J. Aerosol. Sci **25**, S65-S66 (1994).
14. G. P. Fotou, S. Vemury, and S. E. Pratsinis, "Synthesis and evaluation of titania powders for photodestruction of phenol," Chem. Eng. Sci **49**, 4939-948 (1994).
15. J. L. Katz and C. H. Hung, "Initial studies of electric field effects on ceramic powder formation in flames," in *International symposiumon Combustion* (1990), 1733-1738.
16. M. K. Wu, R. S. Steiner, C. k. R. Börs, and S. K. Friedlander, "Controlled Synthesis of Nanosized Particles by Aerosol Processes," Aerosol. Sci. Tech **19**, 527-548 (1993).

17. M. R. Zachariah, D. Chin, J. L. Katz, and H. G. Semerijan, "Silica particle synthesis in a counterflow diffusion flame reactor," Combust. Flame **78**, 287-294 (1989).

18. D. Lindackers, M. G. D. Strecker, and P. Roth, "Formation and growth of SiO_2 particles in low pressure $H_2/O_2/Ar$ flames doped with SiH_4," Combust. Sci. Tech **123**, 287-315 (1997).

19. C. Janzen and P. Roth, "Formation and characteristics of Fe_2O_3 nano-particles in doped low pressure $H_2/O_2/Ar$ flames," Combustion and Flame **125**, 1150-1161 (2001).

20. B. Lewis and G. v. Elbe, *Combustion, Flames and Explosions of Gases*, 3rd ed. Vol. 1 (Academic Press Inc, 1987).

21. S. R. Turns, *An introduction to combustion*. McGraw Hill series in mechannical engineering. Vol. 1 (McGraw Hill, 1996, 565).

22. J. P. Botha and D. B. Spalding, "The laminar Flame Speed of Propane-Air Mixtures with Heat Extraction from the Flame," Proceedings of the Royal Society of London Sereies **225**, 71-96 (1954).

23. P. Ifeacho, T. P. Huelser, H. Wiggers, C. Schulz, and P. Roth, "Synthesis of SnO_{2-x} nanoparticles tuned between $0<x<1$ in a low pressure $H_2/O_2/Ar$ flame," Proc. Combust. Inst. **31**, 1805-1812 (2007).

24. D. L. Hall, A. A. Wang, K. T. Joy, T. A. Miller, and M. S. Wooldridge, "Combustion synthesis and characterization of nanocrystalline tin and tin oxide (SnOx, X = 2)," J. Am. Ceram. Soc **87**, 2033-2041 (2004).

25. J. Warnatz, U. Maas, and R. W. Dibble, *Combustion: Physical and chemical fundamentals, Modelling nd Simulation, Experiments, Pollutant formation*, 3rd ed (Springer, 1996).

26. P. Roth, *Combustion Science script*. 2002: Universität Duisburg-Essen, Duisburg. p. 1-299.

27. J. Knipping, *Synthese und Charakterisierung von Nanopartikeln aus Eisen und Eisenoxid*, in *Fakultät Ingenieurwissenschaften*. 2006, Universität Duisburg-Essen: Duisburg. p. 117.

28. A. Turbiez, A. El Bakali, J. F. Pauwels, A. Rida, and P. Meunier, "Experimental sturdy of a low pressure stoichiometric premixed methane, methane/ethane, methane/ethane/propane and synthetic natural gas flames," Fuel **83**, 933-941 (2004).

29. C. Doute, J. Delfau, R. Akrich, and C. Vovelle, "Experimental study of the chemical structure of low-pressure premixed n-heptane-O_2-Ar and isooctane-O_2-Ar flames," Combust. Sci. Tech **124**, 249-276 (1997).

30. T. T. Kodas and M. Hampden-Smith, *Aerosol processing of materials*. Vol. 1 (Wiley-VCH, New York, 1999, 680).

31. U. Backman, *Studies on nanoparticle synthesis via gas-to-particle conversion*, Helsinki, 2005, 1-49).

32. S. K. Friedlander, *Smoke, Dust and Haze* (John Wiley, New York, 2000).

33. W. C. Hinds, *Aerosol technology* (Wiley, New York, 1999).

34. P. Roth, "Particle synthesis in flames," Proc. Combust. Inst **31**, 1773-1788 (2006).

35. S. H. Ehrman, S. K. Friedlander, and M. R. Zachariah, "Characteristics of SiO_2/TiO_2 nanocomposite particles formed in a premixed flat flame," J. Aerosol. Sci **29**, 687-706 (1998).

36. J. L. Katz, "Homogenous nucleation; theory and experiment," Pure & Appl. Chem **64**, 1661-1666 (1992).

37. J. H. Seinfeld, *Atmospheric chemistry and physics of air pollution* (Wiley, New York, 1986).

38. S. K. Friedlander and M. K. Wu, "Linear rate for the decay of the excess surface area of a coalescing solid," Physical review B **49**, 3622-3624 (1994).

39. S. Tsantilis and S. E. Pratsinis, "Soft-and Hard-agglomerates Aerosols made at high temperatures," Langmiur **20**, 5933-5939 (2004).

40. P. Ifeacho, H. Wiggers, and P. Roth, "SnO_2/TiO_2 mixed oxide particles synthesized in doped premixed H_2/O_2/Ar flames," Proc. Combust. Inst. **30**, 2577-2584 (2005).

41. K. K. Akurati, A. Vital, R. Hany, B. Bommer, T. Graule, and M. Winterer, " One-step flame synthesis of SnO_2/TiO_2 composite nanoparticles for photocatalytic applications," International Journal of Photoenergy **7**, 153-161 (2005).

42. C. Janzen, J. Knipping, B. Rellinghaus, and P. Roth, " Formation of silica-embedded iron-oxide nanoparticles in low-pressure flames," J. Nanopart. Res **5**, 589-596 (2003).

43. S. H. Ehrman, S. K. Friedlander, and M. R. Zachariah, "Phase segregation in binary SiO_2/TiO_2 and SiO_2/Fe_2O_3 nanoparticle aerosols formed in a premixed flame," J. Mater. Res **14**, 4551-561 (1999).

44. S. Jain, T. T. Kodas, M. K. Wu, and P. Preston, "Role of surface reaction in Aerosol synthesis of titanium dioxide," J. Aerosol. Sci **28**, 133-146 (1997).

45. S. Jain, P. Atanasova, T. T. Kodas, and M. Hampden-Smith, "In Situ Formation of Coated and Composite Palladium Particles via Spray Pyrolysis," J. Electochem. Soc **143**, 3762-3770 (1996).

46. Z. Sun, L. Liu, L. Zhang, and D. Jia, "Rapid synthesis of ZnO nano-tods by one step, room-temperature, solid-state reaction and ther gas-sensing properties," Nanotechnology **17**, 2266-2270 (2006).

47. F. Xu, S. D. Tse, J. F. Al-sharab, and B. H. Kear, "Flame synthesis of aligned tungsten oxide nanowires," Appl. Phys. Lett. **88**, 243115/1-3 (2006).

48. B. Cheng and E. T. Samulski, "Fabrication and characterization of nanotubular semiconductor oxides In_2O_3 and Ga_2O_3," J. Mater. Chem **11**, 2901-2902 (2001).

49. S. D. Bakrania, C. Perez, and M. S. Wooldridge, "Methane-assisted combustion synthesis of nanocomposite tin dioxide materials," Proc. Combust. Inst **31** (2007).

50. Y. J. Jang, C. Simer, and T. Ohm, "Comparison of zinc oxide nanoparticles and its nano-crystalline particles on the photocatalytic degradation of methylene blue," Material Research Bulletin **41**, 67-77 (2006).

51. I. J. Gallardo, *Tungsten oxide nanocrystalline powders for gas sensing applications*, in *Deoartment of Electronics*. 2003, Universitat De Barcelona: Barcelona. p. 226.

52. C. L. Yeh, S. H. Yeh, and K. K. Ma, "Flame synthesis of titania particles from titanium tetraisopropoxide in premixed flames," Powder technology **145**, 1-9 (2004).

53. P. Entel, M. Kreth, R. Meyer, and K. Kadau, "Vibrational behavior of nanocrystalline materials Phonons in Condensed Materials," S. P. Sanyal and R.K. Singh, Editors (Allied Publishers, New Delhi, 2004).

54. A. S. Edelstein and R. C. Cammarata, eds. *Nanomaterials: Synthesis properties and Applications*. Institute of Physics series in Micro and Nanoscience and Technology, ed. P. J. Dobson and V. K. Varadan (Institute of Physics Publishing, London, 1996).

55. M. Fox, *Optical properties of Solids*. Oxford master series in Condensed Matter Physics (Oxford University Press, New York, 2001, 305).

56. J. R. Hook and H. E. Hall, *Solid state Physics*, 2nd ed (John Wiley & Sons Ltd, Chichester, 2000, 474).

57. L. M. Liz-Marzán and P. V. Kamat, eds. *Nanocale materials*. Vol. 1 (Kluwer Academic Publishers, Dordrecht, 2003, 499).

58. V. Simanzhenkov, P. Ifeacho, H. Wiggers, J. Knipping, and P. Roth, "Synthesis of germanium oxide nanoparticles in low-pressure premixed flames," Journal of Nanoscience and Nanotechnology **4**, 157-161 (2004).

59. H. Kleinwechter, C. Janzen, J. Knipping, H. Wiggers, and P. Roth, "Formation and properties of ZnO nanoparticles from gas phase synthesis processes," J. Mater. Sci **37**, 4349-4360 (2002).

60. L. Suber, R. Zysler, A. Garcia Santiago, D. Fiorani, M. Angiolini, A. Montone, and J. L. Dormann, "Size and shape effect on the magnetic properties of α-Fe_2O_3 nanoparticles," Mat. Sci. Forum, 269-272 (1998).

61. P. Roth and A. Hospital, "Design and test of a particle mass spectrometer (PMS)," Journal of Aerosol Science **25**, 61-73 (1994).

62. A. Hospital and P. Roth, "In-situ mass growth measurements of charged soot particles from low pressure flames," Proc. Combust. Inst. **23**, 1573-1579 (1991).

63. N. A. Fuchs, "On the stationary charge distribution on Aerosol particles in bi-polar atmosphere," Pura. Appl **56**, 185-193 (1963).

64. B. F. Kock, C. Kayan, J. Knipping, H. R. Orthner, and P. Roth, "Comparison of LII and TEM sizing during synthesis of Iron Particle Chains," Proc. Combust. Inst **30**, 1689-1697 (2005).

65. B. F. Kock, Th. Eckhardt, and P. Roth, "In-cylinder Sizing of Diesel Particles by Time-Resolved Laser-Induced Incandescence (TR-LII)," Proc. Combust. Inst **29**, 2775-2782 (2002).

66. A. V. Filipov, M. W. Markus, and P. Roth, "In-situ Characterization of ultrafine Particles by Laser Induced Incandescence Sizing and Particle Structure Determination," J. Aerosol. Sci **30**, 71-87 (1999).

67. B. F. Kock, *Zeitaufgelöste laserinduzierte Inkandeszenz (TR-LII)*, in *Fakultät für Ingenieurwissenschaften*. 2005, Universität Duisburg-Essen: Duisburg. p. 145.

68. H. A. Michelsen, "Understanding and predicting the temporal response of laser-induced incandescence from carbonaceous particles," J. Chem. Phys **118**, 7012-7045 (2003).

69. M. Kerker, *The scattering of light nd other electromagnetic radiation* (Academic Press, New York, 1996).

70. S. Will, S. Schraml, and A. Leipertz, "Two-dimensional soot-particle sizing by time-resolved laser-induced incandescence," Opt. Lett **20**, 2342-2344 (1995).

71. M. Winterer, *Röntgen-Pulverdiffraktometrie an nanokristallinem Titandioxid*, in *Nanopartikel-Prozeßtechnik Praktikum*. 2006: Duisburg. p. 1-10.

72. S. Braunauer, P. H. Emmett, and E. Teller, "Adsosorption of gases on multimolecular layers," J. Am. Chem. Soc **60**, 309-319 (1938).

73. O. Bartels, *Darstellung, Charakterisierung und Eigenschaften von Phthalocyanin-Molekularsiebkompositen in der photokatalysierten Oxidation von Natriumsulfid*, in *Biologie/Chemie*. 2003, Universität Bremen: Bremen. p. 215.

74. L. E. Murr, *Electron and Ion Microscopy and Microanalysis*. Vol. 1 (Dekker, New York, 1982, 793).

75. E. Barsoukov and J. R. Macdonald, *Impedance Spectroscopy: Theory, Experiment, and Applications* (John Wiley and Sons, New York, 2005).

76. W. G. Bessler and C. Schulz, "Quantitative multi-line NO-LIF temperature imaging," Appl. Phys B **78**, 519-533 (2004).

77. A. O. Vyrodov, J. Heinze, M. Dillmann, U. E. Meier, and W. Stricker, "Laser-induced fluorescence thermometry and concentration measurements on NOA–X (0-0) transitions in the exhaust gas of high pressure CH4/air flames," Appl. Phys B **61**, 409-414 (1995).

78. Z. Wenhua and S. E. Pratsinis, "Synthesis of SiO_2 and SnO_2 particles in diffusion flame reactors," AiChE Journal **43**, 2657-2664 (1997).

79. D. Lindackers, *Erzeugung und charakterrisierung von oxidischen Nano-Partikeln*, in *Fakultät von Ingenieurwessenschaften*. 1999, Universität Duisburg-Essen: Duisburg. p. 1-137.

80. P. Ifeacho, T. Huelser, V. Kravets, H. Wiggers, and C. Schulz, *Synthesis and characterization of SnO_x nanoparticles in a low-pressure premixed $H_2/O_2/Ar$ flame reactor*, in *European combustion meeting*. 2005: Louvain La Neueve.

81. J. Tauc, R. Grigorovici, and A. Vancu, "Optical properties and electronic structure of amorphous germanium," Phys. Stat. Sol **15**, 627-637 (1966).

82. S. Luo, J. Fan, W. Liu, M. Zhang, Z. Song, C. Lin, X. Wu, and P. K. Chu, "Synthesis and low-temperature photoluminescence properties of SnO_2 nanowires and nanobelts," Nanotechnology **17**, 169-1699 (2006).

83. M. Kennedy, *Investigation of tin oxide (SnO_x) gas sensor*, in *Fakultät für Ingenieurwessenschaften*. 2004, Universität Duisburg-Essen: Duisburg. p. 1-145.

84. SANDIA National Labs, *CHEMKIN PREMIX Ver 3.7*. 2001.

85. J. Herzler and P. Roth, "High temperature gas phase reaction of SnO_g with O_2," Phys. Chem. Chem. Phys **5**, 1552-1556 (2003).

86. K. Takahashi, A. Giesen, and P. Roth, "High temperature reaction of $Sn(^3P_0)$ atoms with O_2 based on Sn and O-concentration measurements," Phys. Chem. Chem. Phys **3**, 4296-4300 (2001).

87. R. K. Joshi and F.E. Kruis, "Influence of Ag particle size on ethanol sensing of SnO1.8:Ag nanoparticle films: a method to develope parts per billion level gas sensors," Applied Physics Letters **89**, 153116-1-3 (2006).

88. P. Ifeacho, A. Kowalik, H. Wiggers, P. Roth, and C. Schulz, "Synthesis and Characterization of High Surface Area TiO_2 Nanoparticles from Gas-phase Processes," in *PARTEC* (Nuremberg, 2007).

89. P. T. Spicer, S. T. O. Chaoul, and S. E. Pratsinis, " Titania formation by TiCl4 gas phase oxidation, surface growth and coagulation," J. Aerosol. Sci **33**, 17-34 (2001).

90. U. Diebold, "The surface science of titanium dioxide," Surface Sceince Reports **48**, 53-229 (2003).

91. A. Mills and S. Morris, "Photomineralization of 4-chlorophenol sensitized by titanium dioxide: a study of the initial kinetics of carbon dioxide photogeneration," J. Photochem. Photobiol. A: Chem, 75-83 (1993).

92. K. K. Akurati, A. Vital, G. Fortunato, R. Hany, F. Nueesch, and T. Graule, "Flame synthesis of TiO2 nanoparticles with high photocatalytic activity," Solid State Sciences **9**, 247-257 (2007).

93. D. Q. Fei, T. Hudaya, and A. A. Adesina, " Visible-light activated titania perovskite photocatalysts: Characterization and initial activity studies," Catalysis Communications **6**, 253-258 (2005).

7 Appendix A

Table 7.1: SnO_2 precursor data

Precursor	Formula	CAS No	Molar mass	Vapour pressure
Tetramethyl Tin	$Sn(CH_3)_4$	594-27-4	178.83	133 mbar @ 25°C

Table 7.2: Material properties SnO_2

Material	Molar mass	Density (g/cm^3)	Melting point (°C)	Boiling point (°C)
SnO_2	150.69	6.90-7.00	1630	1800-1900 (sublimes)

Table 7.3: Crystal structure

Crystal structure	System	Space group	Lattice constants (nm)		
			a	*B*	*C*
rutile	tetragonal		0.472		0.318

Table 7.4: TiO_2 precursor data

Precursor	Formula	Cas No	Molar mass	Vapour pressure
Titanium tetra iso-propoxide	$Ti(OC_3H_7)_4$	546-68-9	284.25	< 0.1 mbar @ 25°C

Table 7.5: Material properties TiO_2

Material	Molar mass	Density (g/m^3)	Melting point (°C)	Boiling point (°C)
TiO_2 (anatase)	79.9	3.830		2500-3000
TiO_2 (rutile)	79.9	4.240	1870	2500-3000

Table 7.6: Crystal structure

Crystal structure	System	Space group	Lattice constants (nm)		
			a	b	c
anatase	tetragonal		0.3733	-	0.937
rutile	tetrogonal		0.4584	-	0.2953

Curriculum vitae

Personal data

Name	Pascal Onyibo Ifeacho
Date of birth	27th September 1974
Place of birth	Enugu, Nigeria
Nationality	German
E-mail	pifeacho@gmail.com

School record

09/1980-08/1985	Nigeria Airforce primary school, Ikeja, Lagos, Nigeria
09/1985-08/1986	Command Secondary school, Abakaliki, Nigeria
09/1986-10/1991	Nigeria Airforce secondary school, Ikeja, Lagos, Nigeria

University record

02/1992-12/1997	B.Sc in chemical engineering from the university of lagos, Akoka, Nigeria
11/1999-02/2002	M.Sc in chemical engineering from the Friedrich Alexander Universität, Erlangen, Germany
04/2002-07/2002	Research assistant at the institute for mechanical process engineering at the Friedrich Alexander Universität, Erlangen, Germany

Professional record

01/1998-10/1999	Project/operations engineer at Pamax Associates Nigeria limited, Lagos, Nigeria
09/2002-08/2007	Research assistant at the institute for combustion and gas dynamics, Universität Duisburg-Essen, Campus Duisburg
Since 09/2007	Technologist at Shell Deutschland Oil GmbH